UC Berkeley
UC Berkeley Electronic Theses and Dissertations

Title
Structural Insights into Gas Binding and Signal Transduction in the H-NOX Family of Heme Proteins

Permalink
https://escholarship.org/uc/item/88c3k2xg

Author
Herzik, Mark Anthony

Publication Date
2014

Peer reviewed|Thesis/dissertation

eScholarship.org Powered by the California Digital Library
University of California

Structural Insights into Gas Binding and Signal Transduction in the H-NOX Family of Heme Proteins

By

Mark Anthony Herzik, Jr.

A dissertation submitted in partial satisfaction of the

requirements for the degree of

Doctor of Philosophy

in

Molecular and Cell Biology

in the

Graduate Division

of the

University of California, Berkeley

Committee in charge:

Professor Michael A. Marletta, Chair
Professor John Kuriyan
Professor Andreas Martin
Professor Michiko E. Taga

Spring 2014

Structural Insights into Gas Binding and Signal Transduction in the H-NOX Family of Heme Proteins

© 2014

by Mark Anthony Herzik, Jr.

Abstract

Structural Insights into Gas Binding and Signal Transduction in the H-NOX Family of Heme Proteins

By

Mark Anthony Herzik, Jr.

Doctor of Philosophy in Molecular and Cell Biology

University of California, Berkeley

Professor Michael A. Marletta, Chair

Nitric oxide (NO) signaling in mammals occurs through the activation of soluble guanylate cyclase (sGC), which results in the stimulation of cGMP mediated signaling pathways important for blood vessel homeostasis and neurotransmission. sGC is a heterodimeric hemoprotein comprised, typically, of α1 and β1 subunits, with the heme cofactor responsible for selective NO binding located at the N-terminus of the β1 subunit. The heme domain of sGC belongs to a larger class of proteins termed Heme Nitric oxide/OXygen binding (H-NOX) domains, named as such to encompass their ability to serve as either NO or O_2 sensors. Functional characterization of H-NOX proteins from prokaryotes has provided important insight into the roles these proteins serve in biological contexts. However, fundamental questions remain about the mechanisms of NO activation and signal transduction within H-NOX signaling pathways.

Extensive studies on several members of the H-NOX family have established the functional importance of topological features within the protein scaffold that tune the electronic properties of the heme. However, there is little knowledge regarding the functional role of H-NOX protein structure in modulating gas diffusion as a means for tuning the ligand-binding properties. Using X-ray crystallography with xenon as a probe for gas diffusion pathways, a bifurcated tunnel network between the solvent and interior heme site was mapped in a prokaryotic H-NOX protein. Site-directed mutagenesis and kinetic measurements demonstrate that blocking the tunnels to hinder gas diffusion has important consequences on gas-binding affinity. These data suggest that this tunnel network in H-NOX proteins may serve functional roles in controlling the flux of ligands important for tuning gas-mediated signaling.

A key molecular event during NO-induced activation of H-NOX proteins is loss of the heme-histidine bond and formation of a five-coordinate nitrosyl complex. Although this has been known for quite some time, molecular details into this process have remained elusive. Using X-ray crystallography, structures of a prokaryotic H-NOX protein in the ferrous-unliganded as well as both six-coordinate and five-coordinate nitrosyl complexes were reported. These structures

show that several features in the unliganded state maintain the heme in a distorted conformation that relaxes towards planarity following NO binding and loss of the heme-histidine bond. Because the heme and protein conformations are intimately coupled, relaxation of the heme towards planarity results in a pronounced conformational change in the H-NOX protein involving a rotational displacement of the distal subdomain about the proximal subdomain. It is hypothesized that this conformational change is the method by which H-NOX proteins communicate NO binding to downstream signaling partners.

The observation that H-NOX proteins can bind NO as five-coordinate complexes with NO located in either the distal or proximal heme pockets presented the possibility that these two nitrosyl complexes would yield different NO signaling lifetimes as a result of their intrinsically different dissociation rates. To test this hypothesis, two different chemical based NO traps were employed to measure the dissociation rate constants from distal and proximal-bound, five-coordinate NO complexes in a prokaryotic H-NOX protein. Unexpectedly, under all conditions tested, similar rate constants for NO dissociation are observed between these two nitrosyl species. As such, it is hypothesized that the rate-determining step for dissociation of NO from both five-coordinate NO species is loss of the NO-iron bond.

Prokaryotic H-NOX proteins are often found in predicted operons with putative signaling proteins, predominantly histidine kinases. Importantly, histidine kinases are commonly part of two-component signaling systems, which serve as a basic stimulus-response pathway critical for prokaryotes to sense and respond to extracellular stimuli. Furthermore, it has been established that the H-NOX: histidine kinase signaling couple from *Shewanella oneidensis* regulates the motility of the organism in response to NO. To obtain insight into the mechanism by which H-NOX proteins regulate histidine kinase autophosphorylation upon binding NO, various biophysical techniques were employed to determine the architecture of the H-NOX: histidine kinase complex from *S. oneidensis*. From these data, it is hypothesized that the NO-induced conformational change in the H-NOX protein allosterically inhibits histidine kinase activity by eliciting a series of conformational changes in the histidine kinase that places the phospho-accepting histidine in an inaccessible conformation.

TABLE OF CONTENTS

LIST OF FIGURES

LIST OF TABLES

LIST OF ABBREVIATIONS

5cNO	five-coordinate nitrosyl heme complex
6cNO	six-coordinate nitrosyl heme complex
AMPPNP	Adenylylimidodiphosphate
ATP	adenosine triphosphate
BLAST	basic local alignment search tool
CaM	calmodulin
cGMP	guanosine 3', 5'-cyclic monophosphate, cyclic guanosine monophosphate
CO	carbon monoxide
CV	column volume
DEA	diethanolamine
DGC	diguanylate cyclase
DMSO	dimethyl sulfoxide
DNA	deoxyribonucleic acid
DTCS	*N*-(dithiocarboxy)-sarcosine
DTT	dithiothreitol
eNOS	endothelial isoform of NOS
EPR	electron paramagnetic resonance
GST	glutathione S-transferase
GTP	guanosine triphosphate
H-NOX	Heme Nitric oxide/OXygen binding
HDX-MS	hydrogen-deuterium exchange mass spectrometry
HEPES	4-(2-hydroxyethyl)piperazine-1-ethanesulfonic acid
His_6	hexahistidine affinity tag
HK	histidine kinase
ICP-AES	inductively coupled plasma absorption emission spectroscopy
iNOS	inducible isoform of NOS
IPTG	isopropyl β-D-1-thiogalactopyranoside
LC-MS	liquid chromatography mass spectrometry
Mb	myoglobin
MBP	maltose-binding protein
MCP	methyl-accepting chemotaxis protein
MD	molecular dynamics
MnPPIX	manganese protoporphyrin IX
MWCO	molecular weight cutoff
NADPH	nicotinamide adenine dinucleotide phosphate
NO	nitric oxide
NOS	nitric oxide synthase
Ns H-NOX	H-NOX protein from *Nostoc sp* PCC 7120
O_2	oxygen
PAS	Per/Arnt/Sim domain

PCR	polymerase chain reaction
PEG	polyethylene glycol
RMSD	root mean squared deviation
RR	response regulator
RT	room temperature
SDS-PAGE	sodium dodecyl sulfate polyacrylamide gel electrophoresis
SERp	surface entropy reduction server
sGC	soluble guanylate cyclase
So H-NOX	H-NOX protein from *Shewanella oneidensis*
TB	terrific broth
TCEP	tris(2-carboxyethyl)phosphine
TCS	two-component signaling
TEA	triethanolamine
TEV	tobacco etch virus
TFA	trifluoroacetic acid
TLS	Translation/Libration/Screw
Tris	tris(hydroxymethyl)aminomethane
Tt H-NOX	H-NOX protein from *Thermoanaerobacter tengcongensis*
UV	ultraviolet
Vc H-NOX	H-NOX protein from *Vibrio cholerae* O1 El Tor
vis	visible
WT	wild-type

ACKNOWLEDGEMENTS

There are many people who deserve my thanks for their guidance and support.

First and foremost, I would like to thank my advisor Michael Marletta. From my first interaction with Michael during my interview weekend at UC Berkeley I knew that he was someone I would want to work for. Michael conveys a sense of approachability and genuine interest in the well being of his students that, in a field dominated by the introverted and self-advancing, is often missing in PIs. Michael values the opinion of each member of his lab equally and maintains an environment that fosters scientific discussion and camaraderie. Over the years I have enjoyed and appreciated the freedom that Michael gives each student to develop their own ideas and pursue their own interests. This mentoring style, together with Michael's constant, but healthy dose of skepticism, has developed me into the critical and independent thinker that I am today. Michael has incredible scientific instincts and an innate ability to always maintain the greater goal in mind. I am very grateful for all the lessons I have learned from Michael and I can only hope that I have absorbed some of the instincts that have made him the great scientist he is today.

I would like to thank John Kuriyan for his generosity and support after the Marletta lab moved to The Scripps Research Institute. I am very thankful for the fact that John fully integrated me into the daily operations of his lab and treated me as an equal member of his lab. John has amazing instincts as a structural biologist and has the remarkable ability to ascertain biologically relevant features of a structure that others may not observe. Every session spent with John talking about X-ray crystallography or at the computer looking at electron density was always incredibly informative.

I have had many great mentors throughout my years in graduate school. First, I would like to thank Michael B. Winter. I honestly believe that one of my most valued learning experiences in graduate school occurred during our collaboration. Michael's knowledge, maturity, discipline, attention to detail, scientific rigor, and mentoring ability amazed me from our first trip up the hill to the synchrotron and continue to amaze me to this day. Our frequent scientific discussions were always thought provoking and directed at progressing our project towards completion. I would also like to thank Jon Winger who always encouraged me to explore all my options when attempting to interpret data and forced me to think about science in new and deeper ways. Jon was always capable of serving as devil's advocate, albeit in the friendliest of manners, in order to ensure that all avenues had been explored prior to reaching a conclusion. Jon's wealth of knowledge was an invaluable resource that will always be desired. I would also like to thank Tiago Barros for the continued discussions about crystallography as well as his constant willingness to share his talents in figure making and in writing. Tiago has a keen scientific eye and remarkable talent for communicating scientific data not only in the most visually appealing manner but also in a manner that is the most impactful for the audience. Finally, I would like to thank Jeff Iwig for ongoing discussions about crystallography and metalloproteins as well as his indiscriminate ability to keep people grounded. Jeff was always able to serve as a knowledgeable and unbiased referee when discussing science and I regarded

his opinions highly.

I have been blessed with two amazing undergraduate researchers during my time at Berkeley. I would like to thank my first undergraduate Brandyn West for his eagerness to always tackle the problem at hand and willingness to endure my growth as a mentor during my early years in graduate school. He has an attention to detail and a vast skillset that makes him an excellent scientist. I would also like to thank Rohan Jonnalaggadda for his unbridled enthusiasm for all aspects of our research together. Even during times when things were not going that well he never lost his desire to be in lab and push the project forward. Rohan was also fearless when it came to tackling new projects or new techniques.

I would also like to thank my senior lab mates Nathaniel Fernhoff, Charles Olea and Lars Plate, for being there for me from the first day I walked through the doors of the Marletta lab. Nathaniel and I shared many great conversations about life and science while walking across campus to grab food. Charles was my rotation mentor and taught me that you are capable of doing great science while maintaining a jovial attitude and a sense of humor. Charles also fostered my interest in structural biology in the Marletta lab and was a great resource during my early years. I would like to thank Lars for taking the time to help me to become a successful graduate student and helping me develop my project. Lastly, I would like to thank Christine Phillips-Piro for not only serving as an amazing bay mate and mentor but also acting as my "big" sister in lab. Our consistent scientific discussions in our bay were always insightful and her cheerful attitude was always refreshing.

I would also like to thank members of the Marletta lab – Loes Bevers, Sarah Bissonnette, Hans Carlson, Charles Hespen, Alexander Nierth, Chris Phillips, Minxi Rao, Brian Smith, Sarah Wynia Smith, Basak Surmeli, Rosalie Tran, Eric Underbakke, Van Vu, Emily Weinert, Joshua Woodward, and Jungjoo Yoon –members of the Kuriyan lab – Pradeep Bandaru, Aaron Cantor, Xiaoxian Cao, Yongjian Huang, Steven Jacques, Brian Kelch, Erika Kovacs, Meindert Lamers, Sonja Lorenz, Ethan McSpadden, Andrew Ring, Markus Seeliger, Neel Shah, Margaret Stratton, Patrick Visperas, Qi Wang, and Julie Agard Zorn – and residents of the fifth floor of Stanley Hall – Phil Anselmo, Charlene Bashore, Robyn Beckwith, Randy Blythe, Katie Hart, James Hetfield, Jack Kirsch, Susan Marqusee, Andreas Martin, Chino Moreno, Sabriya Rosemond, Laura Rosen, Avi Samelson, Alex Siegel, Dave Wemmer, and Evan Worden – in addition to those whom I have already mentioned, for the discussions, encouragements, and laughs we have shared.

Lastly, I would like to thank my parents, sisters, lovely wife, extended family, and friends for their continued love and support.

CHAPTER 1

Introduction

Summary

Soluble guanylate cyclase (sGC) is the primary nitric oxide (NO) receptor in mammals and is responsible for stimulating cGMP mediated signaling pathways upon selectively binding NO. Initial efforts to elucidate the determinants of NO-mediated signaling through sGC led to the discovery of the Heme Nitric oxide/Oxygen binding (H-NOX) family of heme proteins. Although it is known that NO binding to the H-NOX domain of sGC activates cyclase activity the molecular mechanism by which NO stimulates activity in sGC, and H-NOX proteins in general, has remained elusive. **Chapter 1** provides historical background into the discovery of the H-NOX family of gas-sensing proteins and describes our current understanding of how H-NOX proteins sense and communicate NO binding to downstream partners.

Nitric Oxide in Mammalian Biology

Nitric oxide (NO) is a highly reactive toxic gas that has evolved over the last three decades from being primarily regarded as an atmospheric pollutant to a well-established signaling molecule critical to numerous physiological processes in mammals [1-5]. In eukaryotes, NO is produced enzymatically by one of three isoforms of the P450-type heme protein nitric oxide synthase (NOS) [6]. Mammalian NO synthases are complex, multi-cofactor enzymes that utilize O_2 and NADPH as co-substrates during the 5 electron oxidation of arginine to citrulline to produce NO [7-9]. During an immunological response, macrophages upregulate the transcription and expression of the inducible isoform of NOS (iNOS) as a means to synthesize high levels of NO (μM) for use as a cytotoxic agent against invading microorganisms [10]. NO signaling in the vasculature is initiated by Ca^{2+} influx into the cytosol of endothelial cells. Calmodulin (CaM) binding to Ca^{2+} and subsequent binding of the CaM:Ca^{2+} complex to eNOS results in the transient activation of eNOS for production of low levels of NO (nM) [8, 9, 11]. NO then diffuses into adjacent smooth muscle cells for activation of soluble guanylate cyclase to result in smooth muscle relaxation and subsequent lowering of blood pressure [11, 12].

Soluble Guanylate Cyclase and H-NOX Proteins

Architecture of H-NOX proteins. Soluble guanylate cyclase (sGC) is the primary nitric oxide (NO) sensor in animals and is responsible for catalyzing the cyclization of GTP to the second messenger cGMP upon binding of NO to its heme cofactor [2, 11-13]. The NO-cGMP signaling pathway is involved in homeostasis of cardiovascular and neuronal processes and dysregulation of this pathway has been implicated in hypertension, erectile dysfunction, and congestive heart failure [14]. sGC is a heterodimeric protein most commonly comprised of α1 and β1 subunits with a dimer interface that involves Per/Arnt/Sim (PAS), coiled coil, and guanylyl cyclase domains homologous to both subunits (**Figure 1.1**) [12, 15]. Interests to elucidate the molecular basis for ligand discrimination led to efforts that defined the minimal heme-binding region as the N-terminal 194 residues of the β1 subunit of sGC. This minimal

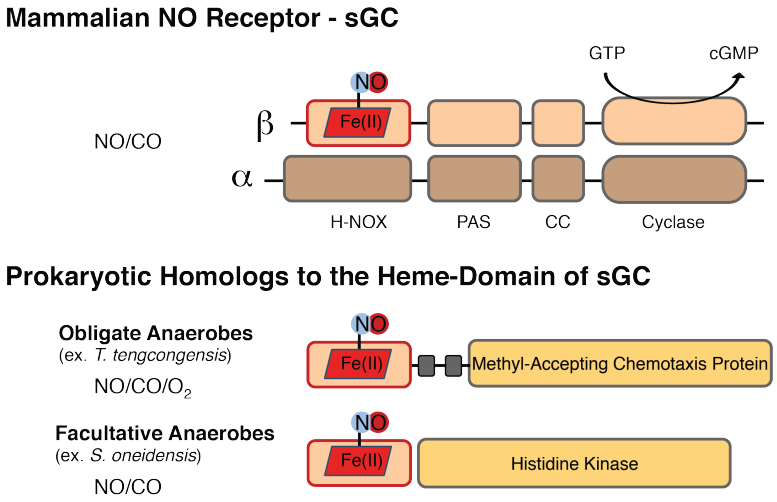

Figure 1.1 Domain architecture of soluble guanylate cyclase (sGC) and prokaryotic H-NOX signaling pairs. The sGC heterodimer contains a single H-NOX domain at the N-terminus of the β1 subunit. The Per/Arnt/Sim (PAS), coiled-coil (CC), and catalytic domains are homologous between the α1 and β1 subunits. H-NOX proteins from obligate anaerobes are found as N-terminal fusions to integral membrane chemoreceptors while H-NOX proteins from facultative anaerobes are in operons adjacent to histidine kinases or diguanylate cyclases.

domain – which was found to contain a histidine-ligated heme and possess identical ligand-binding properties as the full-length enzyme [16-18] – was later used as a BLAST search query that identified heme domain homologues in many different organisms [19]. In prokaryotes the homologues were found in both obligate anaerobes, as fusions to methyl-accepting chemotaxis proteins, as well as facultative anaerobes, as isolable proteins in operons adjacent to histidine kinases or diguanylate cyclases (**Figure 1.1**) [18, 19]. *In vivo* and *in vitro* functional studies have confirmed that several prokaryotic homologues are involved in gas-mediated signaling pathways [20-23].

Biochemical characterization of the prokaryotic heme domain homologues has demonstrated that they have divergent ligand-binding properties depending on the oxygen tolerance of the host organism. Specifically, those heme domains from obligate anaerobes, similar to the globins, were found to bind NO and O_2 whereas those domains from facultative anaerobes, similar to sGC, show selective NO binding even under aerobic conditions [18, 24-27]. Thus to encompass the diverse ligand-binding properties, the family was termed H-NOX (Heme Nitric oxide/OXygen binding) domains [18].

The first crystal structure of an H-NOX family member was determined from the obligate anaerobic bacterium *Thermoanaerobacter tengcongensis* (*Tt* H-NOX) (PDB ID 1U55) and revealed an overall fold that was distinct from other known heme-based gas sensors [28]. From this structure it was determined that H-NOX domains consist of N-terminal and C-terminal subdomains that flank the distal and proximal faces of the heme, respectively. The heme cofactor is bound within the core of the protein via histidine ligation to the heme iron and salt bridge interactions between the heme propionate groups and the absolutely conserved YxSxR motif (**Figure 1.2**) [19, 28]. Further analysis of the heme pocket of *Tt* H-NOX revealed that the heme cofactor was severely distorted from planarity as a result of van der Waals interactions with a conserved proline residue (P115) and a branched hydrophobic residue (I5) that buttress the heme

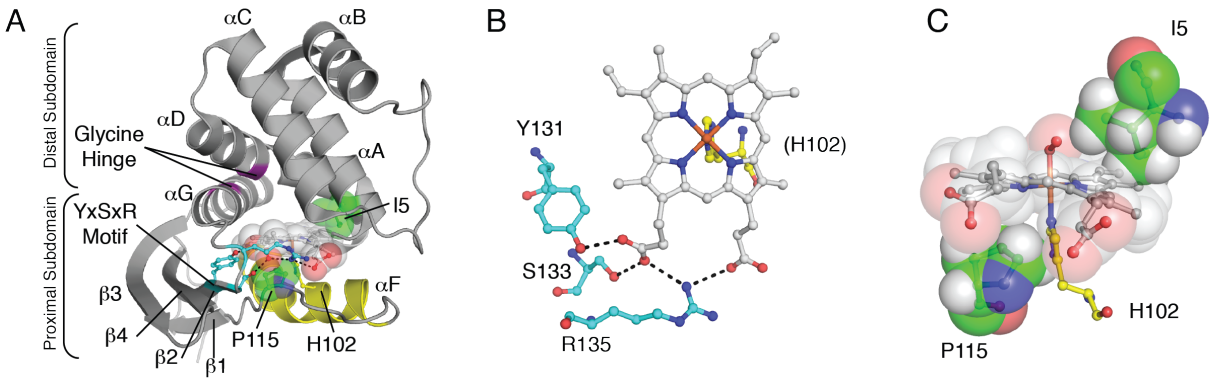

Figure 1.2 X-ray crystal structure of the H-NOX from *Thermoanaerobacter tengcongensis* (*Tt* H-NOX) (PDB ID 1U55). (**A**) Cartoon representation of *Tt* H-NOX with conserved structural features highlighted. The signaling helix is shown in yellow and the glycine hinge is colored purple. (B) The heme-ligating histidine (H102, yellow) and propionate-coordinating YxSxR motif (Y131xS133xR135, blue) are shown as sticks. (C) The heme (light gray) and heme-distorting residues (green) are shown as spheres.

from the proximal and distal heme faces, respectively (**Figure 1.2**). Additionally, two conserved glycine residues were observed to lie at the interface of helices αD-αG. These helices are located at the back of the heme pocket – opposite to the heme propionate groups – and constitute a substantial interface between the distal and proximal subdomains. Moreover, these glycines, termed the "glycine hinge", have been implicated as a means to accommodate changes in orientation of the distal and proximal subdomains by serving as a flexion point [29-31].

Ligand-Binding Determinants in H-NOX Domains. sGC exhibits selective binding of NO under aerobic conditions even though O_2 is at ~1000-fold higher concentration than signaling concentrations of NO *in vivo* [12, 32]. This selectivity is in stark contrast to the globins, which also use a histidyl-ligated heme, as well as a variety of other gas-binding hemoproteins that cannot discriminate between NO, CO and O_2 [33]. Structural and biochemical characterization of several H-NOX proteins from facultative anaerobes – with similar ligand selectivity to sGC – and obligate anaerobes have elucidated several determinants that contribute to the divergent and selective ligand-binding properties of H-NOX proteins.

One of the most striking features of H-NOX protein structures solved to date is the highly distorted porphyrin. Although the modes of distortion – saddling, ruffling, and/or doming – vary across organisms, the amino acids that impart distortion on the porphyrin – a proline (P115 in *Tt* H-NOX) in the proximal pocket and a branched hydrophobic at position 5 in helix αA (I5 in *Tt* H-NOX) in the distal pocket – are conserved across divergent H-NOX proteins (**Figure 1.2C and 1.3**) [19, 26, 28, 30]. Mutagenesis of heme-distorting residues to yield a flattened porphyrin demonstrated that porphyrin distortion plays a role in modulating the electronics of the heme and ligand affinities. Specifically, the P115A mutant of *Tt* H-NOX exhibited a dramatically decreased reduction potential (-4 vs 167 mV) and increased O_2 affinity (21 vs 90 nM) as compared to the Wt protein [29]. Additionally, the I5L mutant of *Tt* H-NOX also displayed a marked decrease in heme reduction potential (101 vs 167 mV) further demonstrating the role of porphyrin distortion in tuning heme electronics in H-NOX proteins [34, 35].

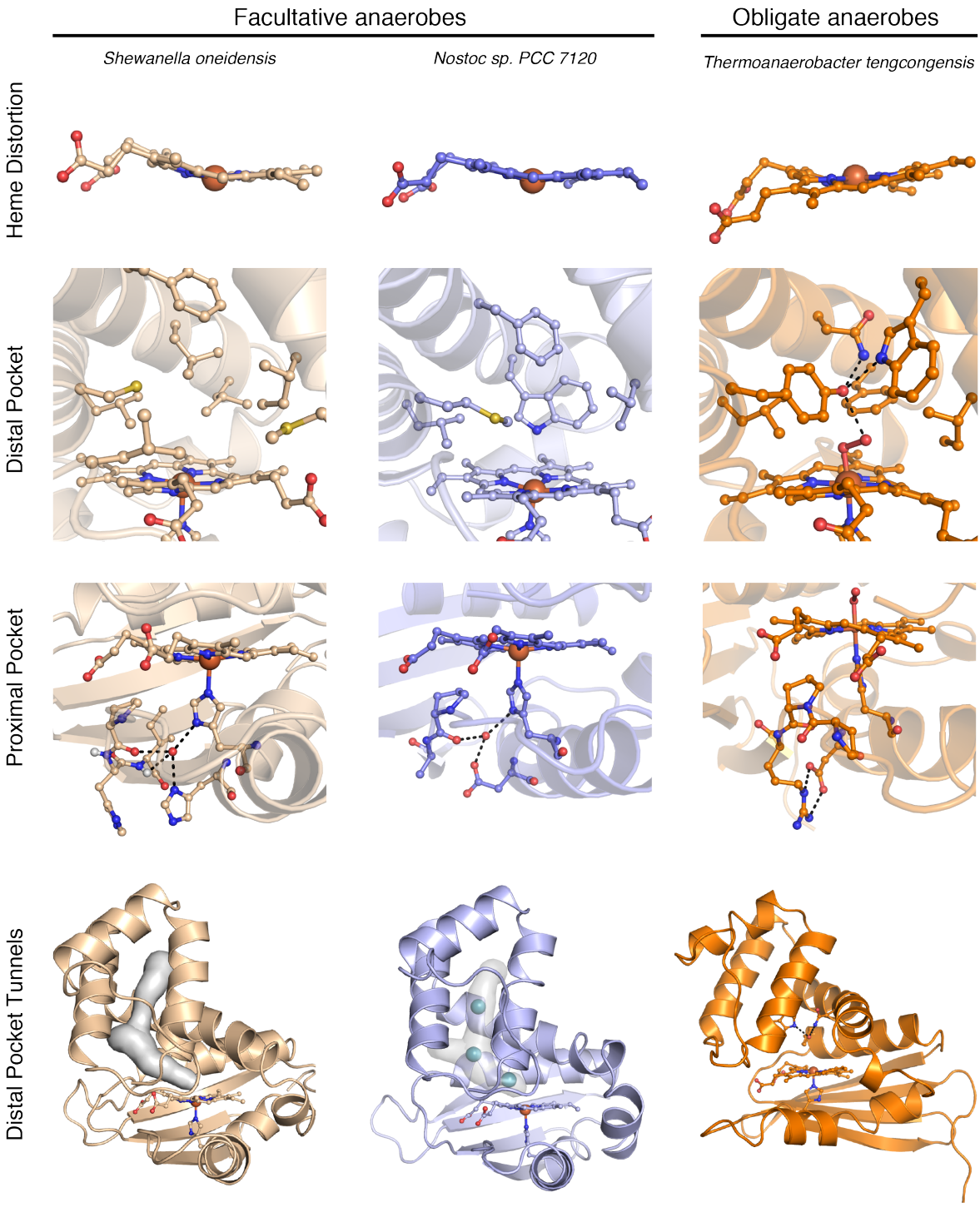

Figure 1.3 Structural features among H-NOX proteins that contribute to their divergent ligand-binding properties. Crystal structures H-NOX proteins from *Shewanella oneidensis* (wheat), *Nostoc sp* (blue, PDB ID 2O09), and *Thermoanarobacter tengcongensis* (orange, PDB ID 1U55) are displayed. Heme cofactors and important residues are shown as sticks, waters are shown as red spheres, and the heme iron is shown as an orange sphere. The bound O_2 molecule in *Tt* H-NOX (shown as sticks) with hydrogen bonds to Y140 from the hydrogen-bonding network shown as a black dashed line. Tunnels within the distal subdomain are shown as a gray surface (calculated using the program CAVER) with experimentally determined xenon atoms shown as light blue spheres. Molecule A for each H-NOX was used.

The structure of *Tt* H-NOX also provided valuable insight into O_2 selectivity in H-NOX proteins. Specifically, it was observed that the distal heme pocket in *Tt* H-NOX possesses a hydrogen-bonding network comprised of residues W9, N74, and Y140 that is responsible for stabilizing bound O_2 via direct hydrogen bond donation by Y140 (**Figure 1.3**). Analysis of multiple sequence alignments indicated that non-O_2-binding H-NOX proteins possess non-polar amino acids at the Y140 position suggesting that the presence of a distal pocket tyrosine could be a key molecular determinant for O_2 binding [28]. Support for this hypothesis was obtained via structure-guided mutagenesis where replacement of the hydrogen-bonding network in *Tt* H-NOX significantly impaired O_2 binding while introduction of a tyrosine in a non-O_2 binding H-NOX conferred O_2 binding [24]. Additional support of this hypothesis was obtained following structure determination of non-O_2-binding H-NOX proteins from *Nostoc sp* (*Ns* H-NOX) and *Shewanella oneidensis* (*So* H-NOX) [26, 30]. Both of these proteins lack hydrogen bond-donating residues in the distal heme pocket. Furthermore, contrary to the polar distal pocket of O_2-binding H-NOX proteins, the distal pockets of non-O_2-binding H-NOX proteins are predominantly non-polar and may further contribute to the divergent ligand-binding properties of H-NOX proteins (**Figure 1.3**).

Although the presence of a distal pocket tyrosine has proven to be a reliable predictor for O_2 binding in bacterial H-NOX proteins, efforts to confer O_2 binding to sGC through introduction of a tyrosine have proven difficult indicating that the mechanisms of ligand discrimination in sGC is more complex. Incorporation of a tyrosine (I145Y) into a H-NOX–containing sGC truncation was found to result in a weak O_2 complex [24] whereas the same mutation in the full-length enzyme did not facilitate O_2 binding [36]. Additional efforts have utilized incorporation of a minimal hydrogen-bonding network (I145Y/I149Q) into sGC [37]. Although an apparent O_2 complex was obtained, the transient nature of the complex and the rapid oxidation of the heme cofactor [36] suggest that additional structural and electronic features in the H-NOX domain of sGC are responsible for modulating ligand affinity.

Recent efforts to elucidate additional mechanisms by which H-NOX tune their ligand binding properties investigated the pathways by which gaseous ligands access the heme. In contrast to the globins, H-NOX proteins possess a heme that is buried within the core of the protein [38]. To elucidate the pathways ligands utilize to access the heme in H-NOX proteins, X-ray crystallography in conjunction with xenon as a probe for gas diffusion was performed. From this study it was determined that the non-O_2-binding *Ns* H-NOX protein possesses a bifurcated tunnel network in the distal subdomain that can serve as a molecular conduit for gas diffusion to the heme. Support for this conclusion was obtained by direct observation of xenon atoms binding solely within the tunnel network (**Figure 1.3**). In addition, structure-guided mutagenesis in combination with time-resolved absorption techniques established a functional role for these tunnels in tuning ligand affinity within *Ns* H-NOX [39]. Analysis of the crystal structure of the non-O_2-binding H-NOX from *Shewanella oneidensis* also demonstrates a bifurcated tunnel network in the distal subdomain (calculated using CAVER [40]). However, the O_2-binding H-NOX from *T. tengcongensis* does not possess these tunnels as a result of W9 from the conserved hydrogen-bonding network locating directly where the putative tunnel network would occur (**Figure 1.3**) [39]. As such, it is hypothesized that all non-O_2-binding H-NOX proteins, including sGC, utilize this tunnel network as a means to control ligand flux to the heme.

Additional support for the role of this tunnel network serving as a gas conduit resulted from molecular dynamics (MD) simulations in which CO ligands were allowed to diffuse from the heme iron to solvent [41]. Insights obtained from this study are in agreement with experimental results and demonstrate that in *Ns* H-NOX escaping CO ligands preferentially utilize this tunnel network as a molecular pathway. The same simulation carried out on *Tt* H-NOX, which lacks the tunnel network, led to the conclusion that protein fluctuations near the heme edge permit ligand flux [41]. This observation agrees with experimental data that indicates xenon atoms are not capable of entering the heme pocket of *Tt* H-NOX *in crystallo* [39]. The potential role of transiently formed pathways for facilitating ligand flux is also evident in *Ns* H-NOX when both tunnels were blocked, as ligand binding was still observed [39]. However, it is clear from the experimental and computational data that the tunnel network, when present, represents the most favorable route of ligand diffusion.

These studies, along with others not mentioned explicitly herein [42-46], together have provided substantial insights into the interior topological features of H-NOX proteins that participate in tuning the electronics of the heme cofactor. Furthermore, significant progress has elucidated which structural features of H-NOX proteins are ubiquitous across all domains of life as well as those that contribute to the divergent ligand-binding proteins within the H-NOX family. This knowledgebase will only be expanded and refined, as more structures of H-NOX proteins are determined.

NO-Induced Activation of H-NOX Proteins

NO Binding to H-NOX Proteins. Initial biochemical studies carried out with an excess of NO suggested that sGC activated in a binary manner – i.e. "off" or "on" – where NO binding increased basal cGMP production several hundred-fold. NO was observed to bind to the open coordination site of the ferrous heme to yield an active, five-coordinate nitrosyl complex following dissociation of the histidine. Importantly, breakage of the iron-histidine bond has been implicated as the key molecular switch for sGC activation [47-50]. However, recent works have determined that NO binding to sGC, and H-NOX proteins in general, is much more complex (**Figure 1.4**).

Extensive kinetic and spectroscopic studies have determined that H-NOX proteins initially bind NO as a six-coordinate complex with NO located distal to the heme-ligating histidine [27, 49, 51, 52]. NO association severely weakens the iron-histidine bond, resulting in histidine dissociation and formation of a five-coordinate NO complex. Most intriguingly, it has been determined that not only does the rate of NO association exhibit NO concentration dependence but the rate of histidine dissociation does as well [27, 49, 51, 52]. As a result of this latter observation, it has been hypothesized that a second NO is responsible for catalyzing histidine dissociation and subsequently binding to the open proximal heme face following histidine loss [27, 49, 52]. Additional support for the involvement of a second NO molecule was obtained using double isotope sequential stopped-flow and freeze quench EPR experiments where a second NO binding event to the proximal heme face could be discerned [52]. These studies have provided substantial evidence that H-NOX proteins potentially bind NO to the proximal heme face under excess NO conditions. However, crystallographic evidence for this species does not exist. It must be noted, however, that under conditions of limiting NO, it is

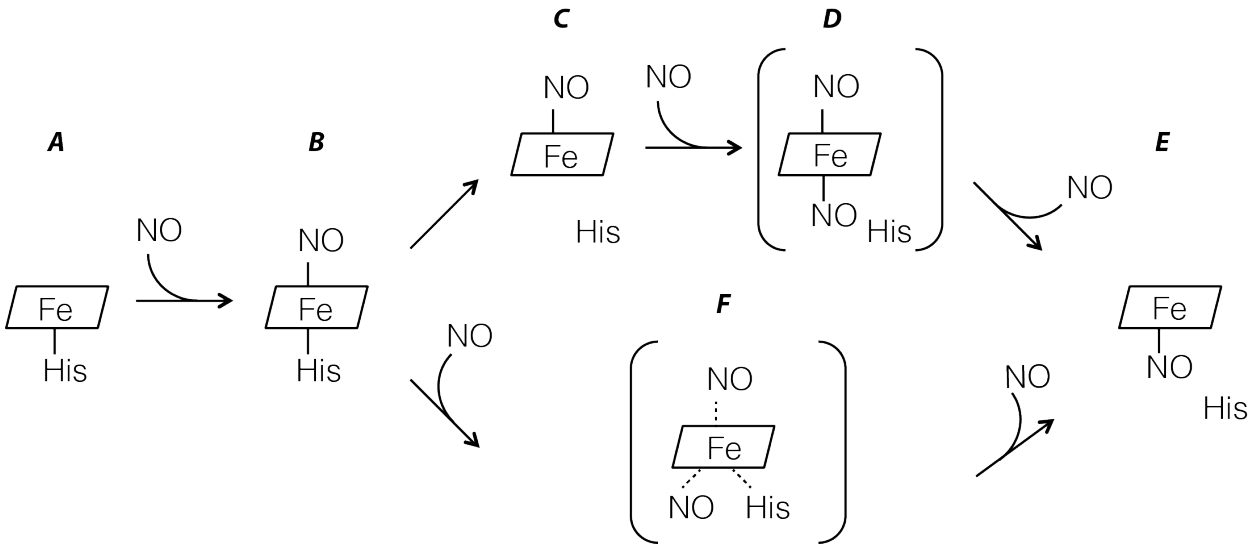

Figure 1.4 Proposed reaction schemes for NO binding to H-NOX proteins. NO binds to the ferrous unliganded H-NOX (***A***) axial to the heme-ligating histidine to form a six-coordinate NO complex (***B***). Following dissociation of the histidine to form a five-coordinate, distal-bound nitrosyl (***C***) a second NO molecule could then bind to the proximal heme face to form a putative dinitrosyl intermediate (***D***) whereby the distal NO would dissociate to leave a five-coordinate, proximal-bound nitrosyl (***E***). Alternatively, the proximal NO complex could occur through a quaternary bis-NO-heme-his complex (***F***) that requires NO attack to the proximal heme face to compete the histidine ligand away. Intermediates ***D*** and ***F*** (shown in brackets) are not observed experimentally and presumably only exist transiently.

postulated that a distal-bound, five-coordinate NO complex will be the dominant species [49, 52].

Two potential mechanisms have been proposed to describe formation of the proximal five-coordinate NO complex under conditions of excess nitric oxide (**Figure 1.4**). Initial NO binding would yield a six-coordinate nitrosyl complex (***A*** to ***B***) whereby subsequent scission of the iron-histidine bond (***B*** to ***C***) would result in a distal-bound, five-coordinate NO complex (***C***). This would expose the proximal face of the heme to allow for binding of a second NO molecule and formation of a putative dinitrosyl-heme complex (***D***). The repulsive *trans* effect imposed by the proximal NO would destabilize the distal-bound NO resulting in its dissociation and a five-coordinate, proximal-bound NO complex [53-55]. Alternatively, following formation of the six-coordinate NO complex, a second NO molecule could bind to the proximal heme face to form a quaternary bis-NO-heme-histidine transition complex (***F***). The five-coordinate, proximal-bound NO complex would then result from dissociation of both the histidine and distal-bound NO [27, 52].

Although it has been observed that most non-O_2-binding H-NOX proteins react with NO in a manner similar to sGC – to form a five-coordinate NO complex – there are examples of non-O_2-binding H-NOXs forming exclusive six-coordinate NO complexes or mixtures of five- and six-coordinate NO complexes [18, 25-27, 32]. Additionally, O_2-binding H-NOX proteins form six-coordinate nitrosyl complexes [18]. Presumably, all H-NOXs interact with NO in a similar

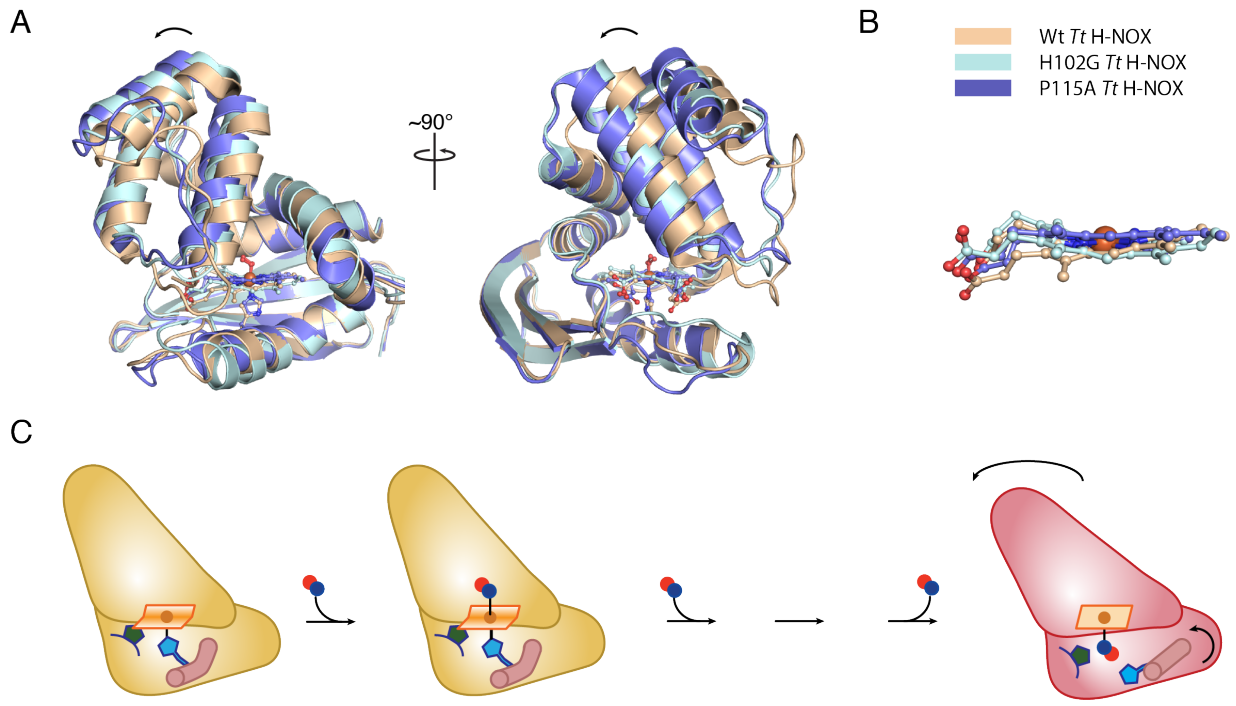

Figure 1.5 NO-induced activation of H-NOX proteins. (**A**) Superimposition of Wt (wheat), H102G (light blue) and P115A (blue) structures of *Tt* H-NOX reveal distal subdomain displacement upon breaking the iron-histidine bond and relaxation of the porphyrin towards planarity. (**B**) Alignment of the heme cofactors for each construct demonstrating relaxation of the porphyrin. (**C**) Heme-strain model of H-NOX activation. In this model, the inactive, unliganded H-NOX (show in gold) maintains the heme in a distorted conformation. NO binds in the distal pocket to form a six-coordinate that following scission of the iron-histidine bond results in a five-coordinate NO complex and the active H-NOX signaling state.

manner – initially binding NO distal to the heme-ligating histidine – except those H-NOXs that maintain an intact iron-histidine bond following NO binding possess unknown structural features in the heme pocket that counteract the *trans* effect exhibited by NO. Furthermore, given the role iron-histidine bond breakage serves in sGC activation, it is unclear at the moment how H-NOX proteins that do not bind NO as a five-coordinate complex transduce ligand binding to their signaling partners.

NO Activation Mechanism. A critical event during NO-induced activation of H-NOX proteins is cleavage of the iron-histidine bond [12, 47]. Substantial efforts have been dedicated to determining the molecular mechanism by which this molecular event activates H-NOX proteins. Unfortunately, structural determination of an unliganded and five-coordinate NO-bound H-NOX protein has proven difficult. However, results compiled across several studies have provided an overarching model of NO activation.

Initial insights into the conformational changes that may occur during NO-induced activation were obtained from crystal structures of *Tt* H-NOX [28]. The first structure of *Tt* H-NOX contained 2 molecules in the asymmetric unit that displayed different orientations of the distal subdomain with respect to the proximal subdomain (PDB ID: 1U55). Further inspection indicated that the overall architecture of each molecule correlated well with the extent by which the heme was distorted from planarity. In addition, mutagenesis to remove the steric bulk

imparted by P115 (P115A) resulted in a significantly more planar heme as well as a different orientation of the distal subdomain as compared to the Wt protein (PDB ID: 3EEE) [29]. Importantly, residue I5 in the distal pocket moves with the trajectory of the heme and thus serves to communicate the conformation of the heme to the distal subdomain. Together, these results indicated that the heme and protein conformation of H-NOX proteins were intimately linked and suggested a potential coupling between ligand binding to the heme and substantial structural changes in the H-NOX domain (**Figure 1.5**).

The first structure of a NO-bound H-NOX protein was determined by soaking crystals of ferrous unliganded *Ns* H-NOX with NO. However, NO was observed to bind as a six-coordinate complex without significant change in protein conformation [26]. This observation is in agreement with previous biochemical data indicating that the key molecular switch is loss of the iron-histidine bond [47]. Superimposition of both NO- and CO-bound *Ns* H-NOX with O_2-bound *Tt* H-NOX structures indicated that ligand binding results in a pivot-shift of the heme within the heme pocket. It was thus speculated that this heme motion could result in displacement of the distal subdomain and potentially serve as a mechanism for NO activation. Though, steric restraints within the heme pocket of *Ns* H-NOX, particularly a tryptophan (W9) located immediately adjacent to the heme iron, could be partially responsible for the noticeable shift of the heme following ligand binding as a result of van der Waals interaction with bound ligands. However, movement of the heme within the heme pocket is a plausible consequence of eliminating histidine ligation.

Further studies to probe the activation mechanism have utilized structural mimics wherein the heme-ligating histidine has been substituted with a glycine and heme binding retained using imidazole as a surrogate for the histidine side-chain [30, 31]. Comparison of these mutants to their Wt counterpart demonstrated that artificially "cleaving" the iron-histidine bond elicits a substantial conformational change involving a 3-6 Å rotational displacement of the distal subdomain about the proximal subdomain (**Figure 1.5**). This conformational change is similar in nature to those structural changes observed upon flattening the heme through removal of the steric bulk imparted by the proximal pocket proline (i.e. P115A vs Wt *Tt* H-NOX). Further inspection of the his-to-gly mutant structures indicates that, alongside the conformational change, removal of the iron-histidine bond results in a more planar heme (**Figure 1.5**). Since a correlation between heme and protein conformation had already been established in H-NOX proteins [29], it was concluded that NO binding and scission of the iron-histidine act to elicit conformational activation of H-NOX proteins via relieving heme distortion.

From these studies, a heme-strain model of NO-induced activation was proposed (**Figure 1.5**) [30]. In this model, structural features in the unliganded state maintain the heme in a conformation highly distorted from planarity. Upon NO binding and cleavage of the iron-histidine bond, these steric restraints are relieved to allow the heme to relax back towards planarity. Intimate interactions between the protein scaffold and the heme serve to communicate flattening of the porphyrin to the distal subdomain, eliciting a pronounced displacement of the distal subdomain with respect to the proximal subdomain. The change in relative orientation between the two subdomains provides a potential mechanism by which H-NOX proteins communicate NO binding to their signaling partners.

Focus of This Research

The focus of this dissertation encompasses multiple aspects of NO signaling by the H-NOX family of heme proteins, including: ligand binding (**Chapter 2**), activation (**Chapter 3**), NO dissociation (**Chapter 4**) and communication of NO binding to signaling partners (**Chapter 5**). Previous studies to examine the structural features that modulate ligand binding in H-NOX proteins have primarily focused on heme pocket residues. However, the observation that H-NOX proteins possess a buried heme cofactor within the core of the protein raised the question: how do ligands access the heme? Initially, X-ray crystallography in conjunction with xenon gas was used to map discrete pathways for ligand diffusion in within the H-NOX scaffold (**Chapter 2**). Structure guided mutagenesis was then employed to block these pathways and examine their influence on the diffusion of gas ligands to the heme by monitoring ligand-binding kinetics. Together, these results indicate that non-O_2-binding H-NOX proteins utilize discrete ligand migration pathways to modulate ligand-binding properties (**Chapter 2**). Although this study, along with previous work, provided insight into how H-NOX proteins tune their ligand affinities, mechanistic information into how NO binding activates H-NOX proteins has remained elusive. Toward this end, crystal structures of a non-O_2-binding H-NOX with high similarity to sGC was crystallized in the unliganded state, as well as both the six-coordinate intermediate and active five-coordinate nitrosyl complexes. From these structures, it is clear that structural features within the unliganded state maintain the heme in a distorted conformation. NO binding eliminates these restraints to allow the heme to relax to planarity and elicit a pronounced conformational change. Furthermore, this study details the first five-coordinate NO structure of a H-NOX protein and provides the first mechanistic linkage between the state of the iron-histidine bond and the conformation of the H-NOX (**Chapter 3**). Intriguingly, NO is observed to bind within the proximal heme pocket in contrast to other ligands that are observed to bind in the distal heme pocket. Because molecular reversibility is not a feasible mechanism for dissociation from the proximal NO complex, the rates of NO dissociation from distal and proximal-bound NO were determined. Most unexpectedly, these complexes are observed to dissociate at the same rate, over a wide range of temperatures, and using two different NO traps (**Chapter 4**). **Chapter 5** reports recent progress into elucidating the molecular mechanism by which H-NOX domains communicate NO binding to their signaling partners.

References

1. Buchan WE, & Charlson RJ (1968) Urban Haze: The Extent of Automotive Contribution. *Science* 159:192–194.
2. Ignarro LJ, Cirino G, Casini A, & Napoli C (1999) Nitric oxide as a signaling molecule in the vascular system: an overview. *J Cardiovasc Pharmacol* 34:879–886.
3. Bredt DS, & Snyder SH (1992) Nitric oxide, a novel neuronal messenger. Neuron. 8:3-11
4. Yoon PS, Iyengar R, Leaf CD, & Wishnok JS (1988) Macrophage oxidation of L-arginine to nitrite and nitrate: nitric oxide is an intermediate. *Biochemistry* 27:8706-8711
5. Palmer RMJ, Ashton DS, & Moncada S (1988) Vascular endothelial cells synthesize nitric oxide from L-arginine. Nature 333:664–666.
6. White KA, & Marletta MA (1992) Nitric oxide synthase is a cytochrome P-450 type hemoprotein. *Biochemistry* 31:6627-6631
7. Marletta MA, Hurshman AR, & Rusche KM (1998) Catalysis by nitric oxide synthase.

Current Opinion in Chemical Biology 2:656–663.
8. Gribovskaja I, Brownlow KC, Dennis SJ, Rosko AJ, Marletta MA, & Steven-Truss R (2005) Calcium-binding sites of calmodulin and electron transfer by inducible nitric oxide synthase. *Biochemistry* 44:7593–7601.
9. Stevens-Truss R, Beckingham K, & Marletta MA (1997) Calcium Binding Sites of Calmodulin and Electron Transfer by Neuronal Nitric Oxide Synthase. *Biochemistry* 36:12337–12345.
10. MacMicking J, Xie Q-W, & Nathan C (1997) Nitric Oxide and Macrophage Function. *Annu Rev Immunol* 15:323–350.
11. Moncada S, Palmer RM, & Higgs EA (1991) Nitric oxide: physiology, pathophysiology, and pharmacology. *Pharmacological reviews*
12. Derbyshire ER, & Marletta MA (2009) Biochemistry of Soluble Guanylate Cyclase - Springer. *cGMP: Generators*
13. Denninger JW, & Marletta MA (1999) Guanylate cyclase and the ·NO/cGMP signaling pathway. Biochimica et Biophysica Acta 1411:334-350
14. Stasch J-P, Pacher P, & Evgenov OV (2011) Soluble Guanylate Cyclase as an Emerging Therapeutic Target in Cardiopulmonary Disease. Circulation
15. Campbell MG, Underbakke ES, Potter CS, Carragher B, & Marletta MA (2014) Single-particle EM reveals the higher-order domain architecture of soluble guanylate cyclase. *Proc Natl Acad Sci* USA.
16. Foerster J, Harteneck C, Malkewitz J, Schultz G, & Koesling D (1996) A Functional Heme-Binding Site of Soluble Guanylyl Cyclase Requires Intact N-Termini of α1 and β1 Subunits. *European Journal of Biochemistry* 240:380–386.
17. Zhao Y, & Marletta MA (1997) Localization of the heme binding region in soluble guanylate cyclase. *Biochemistry* 36:15959–15964.
18. Karow DS, Pan D, Tran R, Pellicena P, Presley A, Mathies RA, & Marletta MA (2004) Spectroscopic Characterization of the Soluble Guanylate Cyclase-like Heme Domains from *Vibrio cholerae* and *Thermoanaerobacter tengcongensis*. *Biochemistry* 43:10203–10211.
19. Iyer LM, Anantharaman V, & Aravind L (2003) Ancient conserved domains shared by animal soluble guanylyl cyclases and bacterial signaling proteins. *BMC Genomics* 4:5.
20. Carlson HK, Vance RE, & Marletta MA (2010) H-NOX regulation of c-di-GMP metabolism and biofilm formation in *Legionella pneumophila*. *Mol Microbiol* 77(4):930-942
21. Wang Y, Dufour YS, Carlson HK, Donohue TJ, Marletta MA, & Ruby EG (2010) H-NOX–mediated nitric oxide sensing modulates symbiotic colonization by *Vibrio fischeri*. *Proc Natl Acad Sci* USA 107:8375.
22. Plate L, & Marletta MA (2012) Nitric Oxide Modulates Bacterial Biofilm Formation through a Multicomponent Cyclic-di-GMP Signaling Network. *Molecular Cell* 46:449–460.
23. Henares B, Xu Y, & Boon E (2013) A Nitric Oxide-Responsive Quorum Sensing Circuit in *Vibrio harveyi* Regulates Flagella Production and Biofilm Formation. *IJMS* 14:16473–16484.
24. Boon EM, Huang SH, & Marletta MA (2005) A molecular basis for NO selectivity in soluble guanylate cyclase. *Nat Chem Biol* 1:53–59.
25. Price MS, Chao LY, & Marletta MA (2007) *Shewanella oneidensis* MR-1 H-NOX Regulation of a Histidine Kinase by Nitric Oxide. *Biochemistry* 46:13677–13683.
26. Ma X, Sayed N, Beuve A, & van den Akker F (2007) NO and CO differentially activate soluble guanylyl cyclase via a heme pivot-bend mechanism. *The EMBO Journal* 26:578–

588.
27. Wu G, Liu W, Berka V, & Tsai A-L (2013) The selectivity of *Vibrio cholerae* H-NOX for gaseous ligands follows the "sliding scale rule" hypothesis. Ligand interactions with both ferrous and ferric *Vc* H-NOX. *Biochemistry* 52:9432–9446.
28. Pellicena P, Karow DS, Boon EM, Marletta MA, & Kuriyan J (2004) Crystal structure of an oxygen-binding heme domain related to soluble guanylate cyclases. *Proc Natl Acad Sci* USA 101:12854–12859.
29. Olea C, Boon EM, Pellicena P, Kuriyan J, & Marletta MA (2008) Probing the Function of Heme Distortion in the H-NOX Family. *ACS Chem Biol* 3:703–710.
30. Erbil WK, Price MS, Wemmer DE, & Marletta MA (2009) A structural basis for H-NOX signaling in *Shewanella oneidensis* by trapping a histidine kinase inhibitory conformation. *Proc Natl Acad Sci* USA 106:19753–19760.
31. Olea C Jr., Herzik MA Jr., Kuriyan J, & Marletta MA (2010) Structural insights into the molecular mechanism of H-NOX activation. *Protein Science* 19:881–887.
32. Boon EM, Davis JH, Tran R, Karow DS, Huang SH, Pan D, Miazgowicz MM, Mathies RA, & Marletta MA (2006) Nitric oxide binding to prokaryotic homologs of the soluble guanylate cyclase β1 H-NOX domain. *J Biol Chem* 281:21892–21902.
33. Hao B, Isaza C, Arndt J, Soltis M, & Chan MK (2002) Structure-Based Mechanism of O_2-Sensing and Ligand Discrimination by the FixL Heme Domain of *Bradyrhizobium japonicum*. *Biochemistry* 41:12952–12958.
34. Tran R, Boon EM, Marletta MA, & Mathies RA (2009) Resonance Raman Spectra of an O_2-Binding H-NOX Domain Reveal Heme Relaxation upon Mutation. *Biochemistry* 48:8568–8577.
35. Olea C Jr., Kuriyan J, & Marletta MA (2010) Modulating Heme Redox Potential through Protein-Induced Porphyrin Distortion. *J Am Chem Soc* 132:12794–12795.
36. Martin E, Berka V, Bogatenkova E, Murad F, & Tsai A-L (2006) Ligand selectivity of soluble guanylyl cyclase: effect of the hydrogen-bonding tyrosine in the distal heme pocket on binding of oxygen, nitric oxide, and carbon monoxide. *J Biol Chem* 281:27836–27845.
37. Derbyshire ER, Deng S, & Marletta MA (2010) Incorporation of Tyrosine and Glutamine Residues into the Soluble Guanylate Cyclase Heme Distal Pocket Alters NO and O_2 Binding. *JBC* 285:17471-17478
38. Tilton RF Jr, Kuntz ID Jr, & Petsko GA (1984) Cavities in proteins: structure of a metmyoglobin xenon complex solved to 1.9 Å. *Biochemistry* 23:2849–2857.
39. Winter MB, Herzik MA Jr, Kuriyan J, & Marletta MA (2011) Tunnels modulate ligand flux in a heme nitric oxide/oxygen binding (H-NOX) domain. *Proc Natl Acad Sci* USA 108:E881–E889.
40. Chovancova E, Pavelka A, Benes P, Strnad O, Brezovsky J, Kozlikova B, Gora A, Sustr V, Klvana M, Medek P, Biedermannova L, Sochor J, & Damborsky J (2012) CAVER 3.0: A Tool for the Analysis of Transport Pathways in Dynamic Protein Structures. *PLoS Comput Biol* 8:e1002708.
41. Zhang Y, Lu M, Cheng Y, & Li Z (2010) H-NOX domains display different tunnel systems for ligand migration. *Journal of Molecular Graphics and Modelling* 28:814–819.
42. Weinert EE, Plate L, Whited CA, Olea C, Marletta MA (2009) Determinants of Ligand Affinity and Heme Reactivity in H-NOX Domains. *Angewandte Chemie* International Edition 49:720–723.
43. Winter MB, McLaurin EJ, Reece SY, Olea C, Nocera DG, & Marletta MA (2010) Ru-

Porphyrin Protein Scaffolds for Sensing O_2. *J Am Chem Soc* 132:5582–5583.
44. Weinert EE, Phillips-Piro CM, & Marletta MA (2013) Porphyrin π-stacking in a heme protein scaffold tunes gas ligand affinity. *Journal of Inorganic Biochemistry* 127:7–12.
45. Tran R, Weinert EE, Boon EM, Mathies RA, & Marletta MA (2011) Determinants of the Heme–CO Vibrational Modes in the H-NOX Family. *Biochemistry* 50:6519–6530.
46. Weinert EE, Plate L, Whited CA, Olea C, & Marletta MA (2010) Determinants of Ligand Affinity and Heme Reactivity in H-NOX Domains. (2009). *Angewandte Chemie International Edition* 49:720–723.
47. Dierks EA, Hu S, Vogel KM, Yu AE, Spiro TG, & Burstyn JN (1997) Demonstration of the Role of Scission of the Proximal Histidine–Iron Bond in the Activation of Soluble Guanylyl Cyclase through Metalloporphyrin Substitution Studies. *J Am Chem Soc* 119:7316–7323.
48. Russwurm M, & Koesling D (2004) NO activation of guanylyl cyclase. *The EMBO Journal* 23:4443–4450.
49. Zhao Y, Brandish PE, Ballou DP, & Marletta MA (1999) A molecular basis for nitric oxide sensing by soluble guanylate cyclase. *Proc Natl Acad Sci* USA 96:14753–14758.
50. Cary SPL, Winger JA, & Marletta MA (2005) Tonic and acute nitric oxide signaling through soluble guanylate cyclase is mediated by nonheme nitric oxide, ATP, and GTP. *Proc Natl Acad Sci* USA 102:13064–13069.
51. Stone JR, & Marletta MA (1996) Spectral and kinetic studies on the activation of soluble guanylate cyclase by nitric oxide. *Biochemistry* 35:1093–1099.
52. Martin E, Berka V, Sharina I, & Tsai A-L (2012) Mechanism of Binding of NO to Soluble Guanylyl Cyclase: Implication for the Second NO Binding to the Heme Proximal Site. *Biochemistry* 51:2737–2746.
53. Lawson DM, Stevenson CEM, Andrew CR, & Eady RR (2000) Unprecedented proximal binding of nitric oxide to heme: implications for guanylate cyclase. *The EMBO Journal* 19:5661–5671.
54. Lawson DM, Stevenson CEM, Andrew CR, George SJ, & Eady RR (2003) A two-faced molecule offers NO explanation: the proximal binding of nitric oxide to haem. *Biochem Soc Trans* 31:553–557.
55. Ascenzi P, Santucci R, Coletta M, & Polticelli F (2010) Cytochromes: Reactivity of the "dark side" of the heme. *Biophysical chemistry* 152:21-27

CHAPTER 2

A TUNNEL NETWORK MODULATES LIGAND FLUX IN A PROKARYOTIC H-NOX DOMAIN*

Summary

In this chapter, a tunnel network in a H-NOX protein was found to serve as a molecular pathway for ligand diffusion from the solvent to the heme cofactor buried within the protein interior. X-ray crystallography using xenon as a probe to map ligand diffusion pathways, in conjunction with structure-guided mutants and kinetic measurements, provide a functional understanding of how this tunnel network modulates heme ligand-binding properties. Together, the data suggest that H-NOX proteins possess discrete ligand migration pathways for the purpose of tuning gas-mediated signaling

Introduction

Protein scaffolds are exquisitely tuned to carry out essential processes in biology. The structures of enzyme active sites, for example, have evolved to both catalyze and lend specificity to numerous chemical transformations. In addition to structural features that directly participate in active site chemistry, proteins often have interior cavities that provide spatial and temporal regulation. These structural features guide small molecule entry and exit as well as link intermediates between reactive centers. For example, channels for gas transport have been identified in enzymes utilizing O_2 (e.g. oxidases and oxygenases) (1, 2), N_2 (nitrogenases) (3), and H_2 (hydrogenases) (4) for critical biological redox reactions. In enzymes with multiple active sites, tunnel networks shunt oftentimes volatile or reactive intermediates between reactive centers for processes such as bacterial carbon fixation (5) and the biosynthesis of essential cofactors (6) and amino acids (7, 8).

Interior structural features have evolved in heme proteins to facilitate diverse types of chemistry with an identical heme cofactor. Historically, globins have served as a model system for understanding how ligand flux through heme protein scaffolds controls gas-binding properties. Over the past 50 years, studies on myoglobin have utilized X-ray crystallography (9), time-resolved absorption techniques (10), CO photolysis of protein crystals (11, 12), and computational methods (13, 14) to provide a detailed molecular picture of ligand migration through the globin fold. Experimental approaches have implicated a histidine residue, the "His(E7) gate" (15), as the primary route for ligand entry and exit, in contrast to computational studies which have identified multiple ligand migration pathways (14). Internal cavities around

---

The worked described in this chapter was done in collaboration with Michael B. Winter in Prof. Michael A. Marletta's laboratory (UC Berkeley) and Prof. John Kuriyan (UC Berkeley). M.B.W. aided in obtaining protein for crystallization and performed kinetic measurements. This work led to the following publication: Winter MB, Herzik MA, Jr.*, Kuriyan J, & Marletta MA (2011) Tunnels Modulate Ligand Flux in a Heme Nitric Oxide/Oxygen Binding (H- NOX) Domain. *Proc Natl Acad Sci USA* 108: 17577-17578, E881-E889.
*Authors contributed equally.

the porphyrin in globins transiently hold O_2 as it migrates to and from the heme iron. These structural features work in concert with residues directly involved in ligand coordination to efficiently capture and release O_2 for gas transport, storage, and delivery in desired physiological contexts (16, 17).

Recent structural studies conducted on non-canonical globins have greatly expanded our knowledge of how globins function (18-23). Alternate topological features such as interior gas tunnels in truncated hemoglobins, for example, have been shown to be mechanistically important for modulating ligand migration (18, 19). However, further studies are needed to fully understand how these related protein frameworks within the globin family contribute to variations in ligand-binding properties. In addition, little is known about how ligand diffusion affects reversible gas binding within a broader spectrum of heme proteins.

H-NOX (**H**eme **N**itric oxide / **OX**ygen binding) domains are a newly discovered family of gas-sensing heme proteins with a novel fold found in organisms from bacteria to humans (24). The best characterized H-NOX-containing protein is soluble guanylate cyclase (sGC), which is the principle mammalian receptor for NO and a central regulator of NO/cGMP-dependant signaling pathways (24). Members of the H-NOX family exhibit divergent ligand-binding properties within the identical protein fold. Some H-NOX domains bind NO, O_2, and CO like the globins, whereas others (including sGC) discriminate against O_2 binding, allowing them to serve as specific NO sensors even under aerobic conditions (24). The presence of a distal pocket tyrosine residue has been shown to be important for stabilizing O_2 binding in the H-NOX family (25). However, it is apparent that additional structural and electronic features contribute to ligand binding properties (25-30).

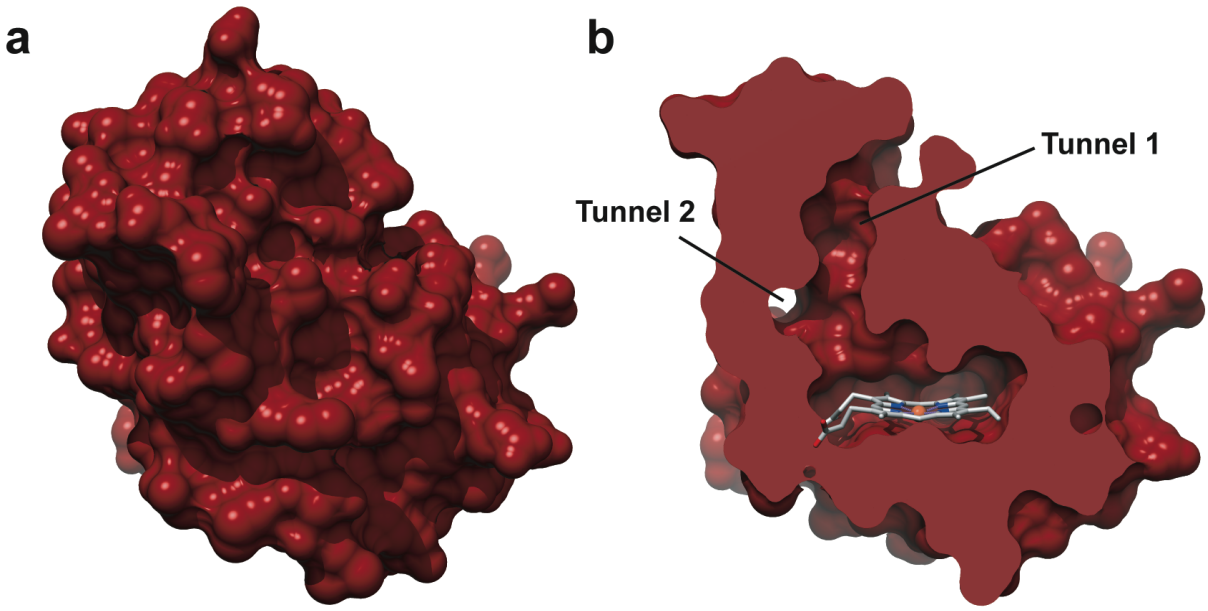

Figure 2.1 Surface representations of WT *Ns* H-NOX depicting **(a)** the protein exterior and **(b)** a cross-sectional view where putative channels between the solvent and heme pocket are evident.

Surface representations of available H-NOX crystal structures (31, 32) indicate that unlike globins, the heme in H-NOX domains is completely buried within the protein matrix (**Figure 2.1A**). Close inspection of a non-O_2-binding H-NOX domain, however, reveals a putative tunnel network (**Figure 2.1B**) that extends between the solvent and interior heme site (33). This tunnel network is comprised of shorter (~15 Å) and longer (~22 Å) branches that are lined by well-conserved, hydrophobic residues and appear to be void of ordered solvent molecules (32). This indicates that the apparent tunnels may serve as potential conduits for gas diffusion. The tunnels are not evident in O_2-binding H-NOX domains, suggesting that differential ligand flux through H-NOX scaffolds could be important for divergent functions (33).

In the present study, direct experimental evidence is provided for the existence of a tunnel network in H-NOX proteins. High-resolution crystal structures were obtained of the non-O_2-binding H-NOX domain from *Nostoc sp*. (*Ns* H-NOX) (32) pressurized with xenon, establishing a molecular route for ligand diffusion between the solvent and heme site. Structure-guided mutagenesis in combination with time-resolved absorption techniques were employed to probe the functional role of the tunnel network in modulating ligand-binding kinetics at the heme. Together, the data has led to an unexpected mechanism for how ligand diffusion regulates ligand-binding properties in the H-NOX family – marking the first time that the effect of tunnels on reversible gas binding has been elucidated in a non-globin fold. This work provides fundamental insights into the functional role of protein scaffolds in controlling the flux of biological molecules.

Materials and Methods

Plasmids for protein expression. The gene for *Ns* H-NOX (residues 1-189) from *Nostoc sp* PCC 7120 (32) was purchased codon-optimized in the pUC vector from GenScript. The gene was PCR amplified and cloned into the pCW plasmid. DNA primers for PCR amplification and site-directed mutagenesis were synthesized by Integrated DNA Technologies. Sequencing of all *Ns* H-NOX variants was carried out by Elim Biopharmaceuticals, Inc. The gene for untagged *Tt* H-NOX (residues 1-188 of *Tt*Tar4H from *Thermoanaerobacter tengcongensis*) (44) and the construct with a C-terminal His_6 tag (26) were used as described previously.

Protein expression. *Ns* H-NOX constructs were transformed into the RP523 strain of *E. coli* (45). Expression cultures were grown at 37 °C in TB media in the presence of 30 μg/mL hemin (~200X stock in DMSO) and 75-100 μg/mL ampicillin. Expression was induced with 1 mM IPTG, and induction was allowed to occur for 18-22 h at room temperature. *Tt* H-NOX constructs were expressed as described previously (26).

Protein purification. All *Ns* H-NOX variants were purified using anion exchange chromatography followed by size-exclusion chromatography. Proteins were isolated in the Fe^{II}–unligated state (Soret maxima of 429-430 nm). *Tt* H-NOX constructs were purified as described previously (26) (45) and isolated in the Fe^{II}–O_2 ligation state (Soret maximum of ~416 nm).

For all *Ns* H-NOX variants, cell pellets (from 1-2 L of *E. coli* expression) were slowly thawed on ice and re-suspended in ~100 mL of buffer A (50 mM DEA, pH 8.5, 25 mM NaCl,

5% glycerol, 5 mM DTT, 1 mM benzamidine hydrochloride), which also contained 1 mM Pefabloc. The resuspended cells were lysed 3 times with an EmulsiFlex-C5 homogenizer (Avestin, Inc.) at 4 °C between 5,000 and 15,000 psi. The lysate underwent centrifugation with an Optima XL-100K ultracentrifuge (Beckman Coulter, Inc.) for 1 h at 42,000 rpm. The supernatant was applied at 1.2-1.5 mL/min to a Toyopearl SuperQ-650M anion exchange column (Tosoh Bioscience GmbH) that had been equilibrated with buffer A. The protein was eluted with a NaCl gradient from 0% to 100% buffer B (50 mM DEA, pH 8.5, 500 mM NaCl, 5% glycerol, 5 mM DTT) over 800 mL at 1.2-1.5 mL/min while 5 mL fractions were collected. Fractions containing *Ns* H-NOX were pooled and concentrated to less than 3 mL using a 5,000 or 10,000 MWCO spin concentrator. Finally, the concentrated protein underwent size-exclusion chromatography with a HiLoad 16/60 Superdex 75 column (GE Healthcare) that had been equilibrated with buffer C (50 mM TEA, pH 7.5, 150 mM NaCl, 5% glycerol, 5 mM DTT). The protein was separated with an isocratic flow of buffer C at 1 mL/min while 2 mL fractions were collected. Fractions containing the highest purity *Ns* H-NOX were pooled and concentrated with a 5,000 or 10,000 MWCO spin concentrator. Purity was estimated to be >90% by Coomassie stain following SDS-PAGE. Subsequent experiments were only carried out with protein isolated in the ferrous-unligated state (Soret absorbance of ~430 nm).

UV–visible spectral characterization. Heme-ligand complexes were generated as described previously using established methods (44). Briefly, UV–visible spectra of various *Ns* H-NOX heme-ligand complexes were acquired in buffer D (50 mM HEPES, 7.4, 50 mM NaCl) at room temperature on a Cary 3E spectrophotometer. Briefly, proteins were fully reduced with ~10 mM dithionite in an anaerobic chamber (Coy) for 5 min at room temperature. Dithionite was subsequently removed using a PD10 column (GE Healthcare). All spectra were acquired under anaerobic conditions in a septum-sealed 1 cm pathlength quartz cuvette. Fe^{II}–CO complexes were generated by sparging the headspace of a cuvette containing ferrous protein with CO (99.99%; Praxair, Inc.) for 5 min. Fe^{II}–NO complexes were generated by adding 4 μM DEA NONOate (Caymen Chemical Company) to ferrous protein via a gastight syringe.

Protein crystallization. WT *Ns* H-NOX and the L66W/L67W mutant were used as purified for crystallization. L66W and L67W were incubated with ~10 mM dithionite for 5-10 minutes in an anaerobic chamber (Coy) to ensure full reduction. All *Ns* H-NOX variants were exchanged into crystallization buffer (5 mM Tris, pH 7.5, 100 mM NaCl, 1 mM DTT) using a PD-10 column. The proteins were crystallized at 20 °C using sitting drop vapor diffusion in which 1 μL of the protein was mixed with 1 μL of reservoir solution and equilibrated against a 700 μL reservoir. For WT *Ns* H-NOX, 15 or 30 mg/mL protein was equilibrated against 1.8 M DL-malic acid (pH 7.0) with and without 100 mM BIS-TRIS propane (pH 7.0). For L66W and L67W, 45 mg/mL protein was equilibrated against 1.9-2.0 M malonic acid (pH 7.0). For L66W/L67W, 10 mg/mL protein was equilibrated against 1.9-2.1 M malonic acid (pH 7.0).

Untagged *Tt* H-NOX was used as purified in the Fe^{II}–O_2 ligation state. Protein was exchanged into crystallization buffer (20 mM TEA, pH 7.5) using a PD-10 column. Crystals were grown using sitting drop vapor diffusion in which 1 μL of the protein (30 or 60 mg/mL) was mixed with 1 μL of reservoir solution and equilibrated against a 700 μL reservoir of 20% to 28% (w/v) PEG 2000 and 200 mM to 250 mM sodium acetate at 20 °C.

All crystals appeared within 12 h. Cryoprotection was achieved by transferring the crystals stepwise into mother liquor solutions containing 5%, 10%, and 15% glycerol for *Ns* H-NOX variants and 5%, 10%, 15%, and 20% for *Tt* H-NOX. The crystals for native data sets were flash frozen in liquid N_2 for storage without further manipulation.

Xenon derivatization. Crystals were derivatized with xenon (research grade; Praxair, Inc.) using a Xenon Chamber (Hampton Research) apparatus following standard protocols (46). Briefly, the wick in the provided Mini-Vial/Wick system was saturated with cryoprotectant, and an additional ~75 μL of cryoprotectant was added to the bottom of the vial to prevent crystal dehydration. The cryoprotectant in the Mini-Vial/Wick system was pre-equilibrated with xenon by pressurizing the chamber 3 times at each xenon pressure to be subsequently used for crystal derivatization. Crystals underwent cryoprotection as described above and were immediately pressurized in the chamber with 1 atm to 8 atm xenon for 0.5, 1, 5, 10, 15, or 30 min. Following derivatization, the chamber was rapidly depressurized (<10 s), and the crystals were immediately frozen (~5 s) in liquid N_2 for storage.

X-ray data collection and structure refinement. For native crystals, X-ray data were collected using synchrotron radiation at beamlines 5.0.2 or 8.3.1 at the Advanced Light Source, Lawrence Berkeley National Laboratory (Berkeley, CA). Diffraction images were collected at 100 K with exposure times of 0.1 s to 1 s and 0.35º to 1º oscillations per frame at a wavelength of λ = 1.1158 Å. Data integration and scaling were performed using the HKL2000 (47) suite, and structure solution was performed using Phaser (48) with *Ns* H-NOX (PDB ID 2O09) or *Tt* H-NOX (PDB ID 1U55) as the search model. Rebuilding of the model was performed using ARP/wARP (49) following molecular replacement, and manual model rebuilding was performed using Coot (38). Iterative model refinement was performed using PHENIX (50) with TLS refinement parameters incorporated. Refinement statistics are listed in **Table A.1 and Table A.2**. Stereochemical properties were assessed by MOLPROBITY (51) and PROCHECK (52).

For xenon-derivatized crystals, diffraction images were collected using inverse beam geometry at a wavelength of λ = 1.3776 Å to maximize xenon anomalous signal (Xe $f'' = 5.8$), and reflection intensities were scaled with anomalous flags selected. Structure solution was performed using rigid body refinement of the native structure against the scaled xenon intensities since the crystals were isomorphous. The location of xenon sites was determined by peak analysis from an anomalous difference map by selecting peaks greater than 4σ that corresponded to peaks in the F_o–F_c map and did not overlap with Fe ($f'' = 2.6$) or S ($f'' = 0.5$) atoms. For initial placement of each xenon atom, the B factor was set to the average of non-hydrogen protein atoms within 5 Å, and the occupancy was set to a value of 0.5. The occupancy and B-factor of each xenon atom were then iteratively refined using restrained refinement until there was no further positive electron density in the F_o–F_c map. Iterative model refinement and assessment of model correctness was carried out as described for the native structures.

Coordinates are deposited in the RCSB Protein Data Bank as entries **3TF8** (WT *Ns* H-NOX), **3TF9** (WT *Ns* H-NOX under 1 atm Xe), **3TFA** (WT *Ns* H-NOX under 6 atm Xe), **3TFD** (L66W), **3TFE** (L66W under 6 atm Xe), **3TFF** (L67W), and **3TFG** (L66W/L67W), **3TF0** (WT *Tt* H-NOX), and **3TF1** (WT *Tt* H-NOX under 6 atm Xe).

Stopped flow spectroscopy. CO association rate constants (k_{on}) were determined for ferrous *Ns* H-NOX (WT, L66W, L67W, L66W/L67W, T48W, and I9W) and ferrous WT *Tt* H-NOX (His_6) at 20 °C using a HiTech KinetAsyst stopped flow instrument equipped with a diode array detector. Ferric-unligated *Tt* H-NOX was prepared by first oxidizing the protein with excess potassium ferricyanide for 5 min at room temperature in an anaerobic chamber. Ferricyanide was then removed with a PD10 column by desalting the protein into buffer D. Both *Ns* and *Tt* H-NOX (~1 μM) were fully reduced with ~10 mM dithionite in an anaerobic chamber. CO binding experiments were conducted in the presence of ~10 mM dithionite to prevent *Tt* H-NOX from partially binding O_2 (K_D = 90 nM) (25) during subsequent sample manipulation on the stopped flow. CO binding rates were found to be dithionite independent. Saturated CO stock solutions (950 μM) were prepared by sparging ~3 mL buffer in a septum-sealed Reacti-Vial (Pierce) with CO (99.99%; Praxair, Inc.) for >30 min at room temperature. Dilutions of CO (24, 48, 95, and 143 μM) were generated directly on the stopped flow in gas-tight syringes by mixing the saturated CO stock solution via a three-way joint with anaerobic buffer. Reactions were initiated by rapid, equal mixing of the ferrous protein and CO solutions. UV–visible spectra were recorded for 450 ms (300 scans, 1.5 ms integration time) from 400-700 nm using the Kinetic Studio program (TgK Scientific). The spectral transition was fit to a two-state model using the SPECFIT Global Analysis System (version 3.0.14). Replicate CO titrations (N = 3-5) were carried out on different days utilizing protein from different preparations whenever possible. Average observed rates (k_{obs}) for each CO concentration are reported for >30 sample shots on the stopped flow.

For CO dissociation rate constants, ferrous-CO protein (2 μM) was mixed with an NO (99.5%; Praxair, Inc.) trap as described previously (40, 42). *Ns* H-NOX variants were fully reduced with ~10 mM dithionite in an anaerobic chamber. Dithionite was subsequently removed by desalting the proteins into buffer D using a PD10 column. *Tt* H-NOX (His_6) samples were oxidized prior to reduction as described above. Ferrous protein (~2 μM) was placed in a septum-sealed tonometer connected via a three-way joint to a syringe containing anaerobic buffer. The headspace of the tonometer was subsequently sparged with 1 atm CO gas (950 μM CO in solution) to prepare the protein Fe^{II}–CO complexes. Saturated NO solutions (2 mM) for NO traps were generated by sparging ~3 mL anaerobic buffer in a septum-sealed Reacti-Vial for >15 min at room temperature with NO (99.5%; Praxair, Inc.) that had been passed through 10 M KOH. The saturated NO solution was removed from the Reacti-Vial with a gas-tight syringe that was then connected via a three-way joint to a syringe containing anaerobic buffer. Prior to sample delivery into the stopped flow, the stopped flow syringes were deoxygenated with an anaerobic dithionite solution. All dithionite was subsequently removed by flushing the stopped flow syringes with anaerobic buffer via the three-way joints described above. Reactions were initiated by rapid, equal mixing of the Fe^{II}–CO protein and NO trap. UV–visible spectra were recorded for 4.5 s from 350-700 nm using the Kinetic Studio program as above. The difference in absorbance (424 and 416 nm) versus time was fit to a single exponential equation using Igor Pro (version 5.01). Measurements were recorded from ≥3 samples on different days and represent ≥18 sample shots on the stopped flow. CO dissociation rates were verified to be independent of NO trap concentration as long as an excess of trap was used. To confirm trap independence, ferrous protein solution containing either 10 or 20 μM CO was mixed with traps containing 200 μM and 2 mM NO.

Flash photolysis. CO association rate constants were also determined using transient absorption spectroscopy at the Beckman Institute Laser Resource Center (California Institute of Technology, Pasadena, CA) with an experimental set-up that has been described previously (53). Proteins were reduced with dithionite and desalted into spectral buffer (50 mM HEPES, pH 7.4, 50 mM NaCl) as described in the stopped flow experiment. The proteins were subsequently sparged with 1 atm CO in a sealed 1 cm pathlength quartz cuvette and incubated under a CO atmosphere overnight at 4 °C with gentle rocking to ensure full sample equilibration prior to data acquisition. The protein Fe^{II}–CO bond was photolyzed using 560 nm irradiation from a Nd:YAG laser (8 ns pulse). Data were collected at 20 °C over 10 ms at 415 and 440 nm from 2 samples on different days. Traces were fit to a single exponential equation using Igor Pro.

Results

Probing gas migration in the predicted tunnels with xenon. X-ray diffraction utilizing xenon is a powerful structural tool to observe gas diffusion through proteins (34). Xenon has a similar polarity and van der Waals radius to diatomic gases (2.16 Å versus 1.50-1.55 Å for O_2, CO, and NO) (35), is freely diffusible in protein crystals, and weakly interacts with protein molecules (34). Importantly, xenon also possesses an appreciable anomalous signal, allowing for unambiguous localization of xenon atoms in protein crystal structures (34). Although xenon has high polarizability, which can bias interactions toward regions in proteins with more polarizable side chains (36), numerous studies have confirmed that the locations of xenon binding sites correlate well with areas that are favorable for diatomic gas migration (12, 13).

Crystals of ferrous-unligated *Ns* H-NOX were obtained for xenon pressurization via sitting drop vapor diffusion. A 2.13 Å structure of the native protein was solved by molecular replacement using the previously published structure of ferrous-unligated *Ns* H-NOX (PDB ID 2O09) (32), which was obtained under different crystallization conditions, as the search model. The *Ns* H-NOX crystal structure solved here was at a similar resolution (2.13 Å vs. 2.10 Å) in the identical space group ($P2_13$) and had comparable unit cell dimensions (a = b = c = 123.7 Å vs. 123.4 Å) as the previous structure (**Table A.1**) (32). The two structures were found to superimpose well with an rmsd of 0.197 Å (C_α–C_α alignment).

To map the putative tunnels in *Ns* H-NOX, native *Ns* H-NOX crystals were subsequently exposed to 1-6 atm of xenon for various times using a xenon pressurization chamber (Hampton Research). A crystal structure of *Ns* H-NOX pressurized with 1 atm of xenon is reported to 2.59 Å resolution (**Table A.1**). As shown in **Figure 2.2A**, 1 xenon atom (blue mesh) was observed per protein molecule at this pressure. The xenon atom is located at the intersection of the apparent tunnels near the distal face of the heme where diatomic ligands bind. The presence of xenon is indicated by spherical electron density in the $2mF_o$–DF_c map generated for *Ns* H-NOX (**Figure 2.2A**) and unambiguously confirmed by the presence of xenon electron density in the anomalous difference map at the same position (**Figure A.1**). The xenon-binding cavity is formed by several hydrophobic contacts. These include the faces of the porphyrin macrocycle and W74 indole ring, the V5 and L148 side chains, the M1 and M144 sulfur atoms, as well as the F70 phenyl ring edge (**Figure 2.2 and A.2**).

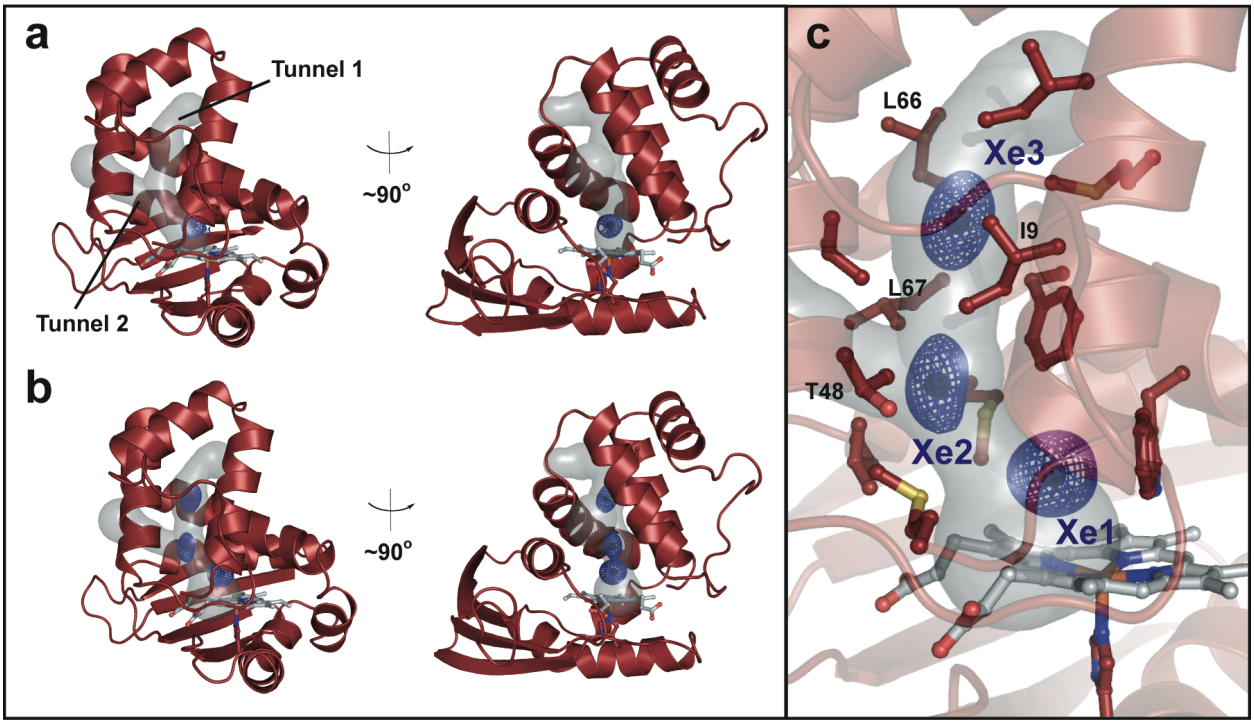

Figure 2.2 Crystal structures of WT *Ns* H-NOX following xenon pressurization. Structures are reported for crystals pressurized with **(a)** 1 atm of xenon for 1 min and **(b)** 6 atm of xenon for 1 min. $2mF_o–DF_c$ maps (mesh surface) for xenon atoms are contoured at 1σ (see **Figure A.1** for anomalous xenon density). **(c)** A detailed view of the 6 atm crystal structure showing numerous residues that line the tunnel network. Key residues that were selected for structure-based rational mutagenesis are indicated. See **Figure A.2** for views of the individual xenon-binding sites (Xe1, Xe2, and Xe3). The tunnel network was modeled using CAVER with the heme iron as the point of origin and a probe radius of 1.5 Å.

To test if *Ns* H-NOX has other accessible xenon-binding sites, a crystal structure of *Ns* H-NOX under 6 atm of xenon was obtained (**Table A.1**). The structure was solved to 2.27 Å resolution and found to align well with the native structure (0.127 Å C_α rmsd). At this higher pressure, three xenon atoms were observed that extend between the heme and the end of tunnel 1 near the solvent interface. The presence of xenon at these locations is evident from electron density in the $2mF_o–DF_c$ map (**Figs. 2.2B and 2.2C**) and the superposition of xenon electron density in the anomalous difference map (**Figure A.1**). Xenon binding in the site identified at lower pressure (herein referred to as "Xe1") is still observed and occurs with higher occupancy in the 6 atm structure (occupancy of 0.6 vs. 0.3 in molecule A). The newly identified sites (referred to as "Xe2" and "Xe3") are also predominately composed of hydrophobic residues (**Figure 2.2C**). For the Xe2 site, the side chains of V5, I9, L67, and L141 as well as the T48 methyl group and face of the F70 aromatic ring contribute to form the xenon-binding pocket. For the Xe3 site at the end of tunnel 1, the binding pocket opens into solvent and is formed at its base by the side chains of I9, M12, I13, V52, and L66, as well as the face of the F70 aromatic ring (**Figure A.2**). Notably, no xenon occupancy was observed in tunnel 2. This smaller channel is predicted to be accessible to diatomic gases in the crystal structure based on molecular modeling (37). However, it may be too narrow to effectively accommodate xenon and/or may lack sufficient contacts to stabilize xenon binding.

The crystallographic data suggest a dynamic picture for xenon movement in the tunnels. Xenon flux is supported by anisotropic electron density at the Xe2 and Xe3 sites (**Figure 2.2C**) and residual density that bridges these sites in the $2mF_o–DF_c$ map for the structure at lower contour levels. Xenon flux in the structure is correlated to xenon occupancy, which decreases from 0.6 to 0.3 to 0.4 for Xe1, Xe2, and Xe3, respectively (using molecule A) (**Table A.1**). Together, the data indicate that xenon moves most dynamically in the tunnel near the protein exterior and more stably interacts with the protein distal to the heme at the Xe1 site. Based on these observations, the tunnels appear to funnel gases between the solvent and protein interior where they are preferentially trapped in the heme distal pocket.

To compare to O_2-binding H-NOX proteins, which do not appear to display a tunnel network (**Figure A.3**) (33), crystals of the H-NOX protein from *Thermoanaerobacter tengcongensis* (*Tt* H-NOX) were pressurized with 6 atm of xenon. The resulting crystal structure of *Tt* H-NOX was solved to 2.03 Å resolution (**Table A.3**) and found to overlay well with the native structure (0.129 Å C_α rmsd). Under these pressurization conditions, two xenon atoms were bound to each protein molecule (**Figure A.3**). However, unlike *Ns* H-NOX, a continuous pathway could not be traced in *Tt* H-NOX, either between the xenon atoms or to the heme pocket. This finding supports the prediction that gas diffusion in O_2-binding H-NOX domains may not occur through discrete, preformed tunnels.

Structure-guided design of mutations to block the tunnel network. To examine the role of the *Ns* H-NOX tunnels in modulating ligand migration, structure-guided mutants were designed in an attempt to block each branch of the tunnel network. Although numerous positions are potentially available for mutagenesis, two candidates (L66W to block tunnel 1 and L67W to block tunnel 2) were selected following modeling of allowed side chain rotamers (38) (**Figure 2.2C**). Leucine-to-tryptophan mutations were chosen principally to provide sufficient steric bulk to interact tightly with surrounding tunnel residues. Additionally, these mutations are predicted to maintain the hydrophobicity of the site (leucine and tryptophan partition coefficients differ by only 0.07) (39). The L66W, L67W, and L66W/L67W variants were generated using standard protocols and purified in a manner analogous to WT *Ns* H-NOX. Ferrous complexes (Fe^{II}–unligated, Fe^{II}–CO, and Fe^{II}–NO) of the isolated proteins were characterized with steady-state UV–visible spectroscopy. UV–visible spectra of the mutants were very similar to those of WT *Ns* H-NOX (**Table A.4**), indicating that incorporation of tryptophan residues in the selected positions did not significantly alter the electronic properties of the heme.

Crystal structures of predicted tunnel-blocking tryptophan mutants. High-resolution crystal structures of the *Ns* H-NOX variants were pursued to establish the effectiveness of the tryptophan residues in blocking the tunnels. Crystals of L66W, L67W, and the L66W/L67W double mutant were obtained in similar conditions to the WT protein (**Materials and Methods**). The structures were solved to 1.96 Å, 1.94 Å, and 1.90 Å resolution, respectively (**Figure 2.3**). Notably, the structures were obtained in the same space group and found to have nearly identical

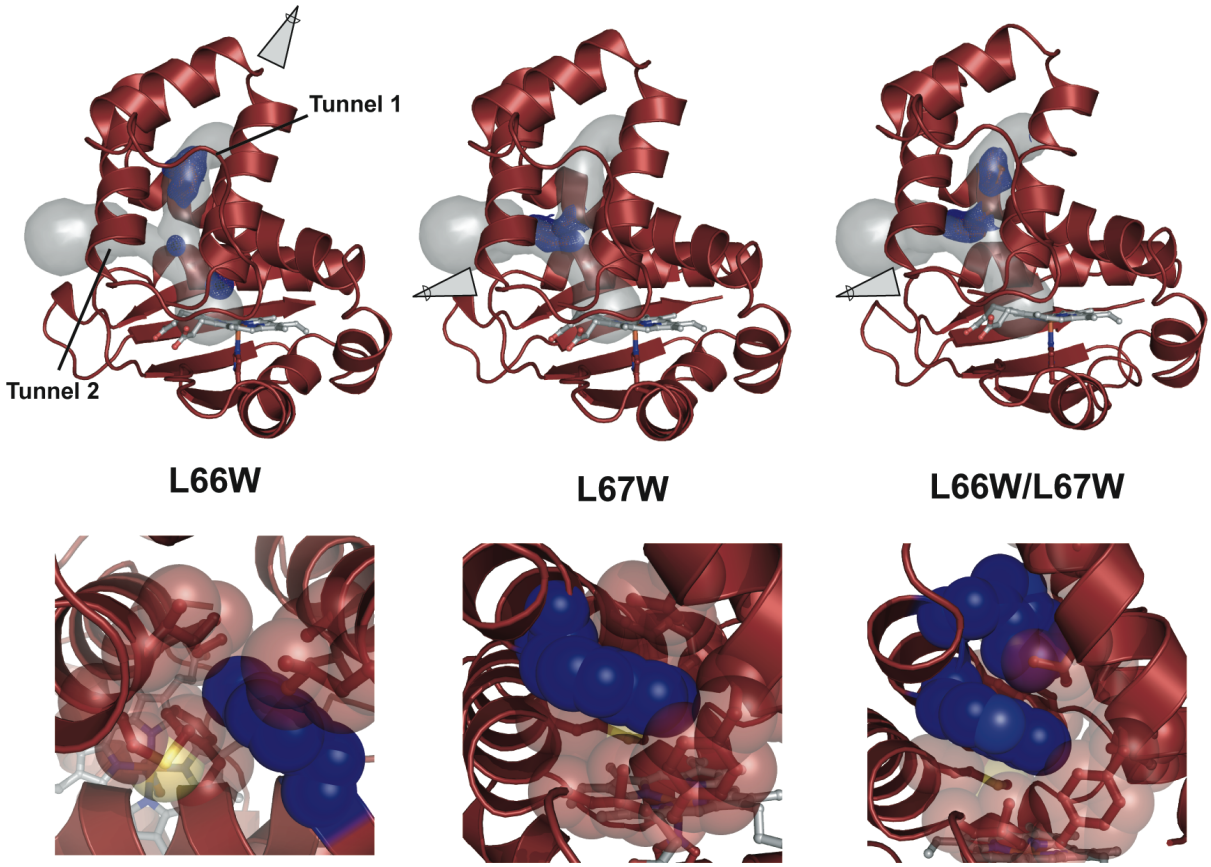

Figure 2.3 Crystal structures of tunnel-blocking variants in *Ns* H-NOX. Structures of L66W (pressurized with 6 atm of xenon for 1 min), L67W, and L66W/L67W are shown. L66W blocks tunnel 1 and L67W blocks tunnel 2. Zoom-in views looking from the solvent to heme pocket depict van der Waals contacts with surrounding tunnel residues: I9, M12, I13, V52, A55, L59, L67, and F70 (for L66W) and T48, V52, F70, L141, M144, Y49 (for L67W). Simulated-annealing composite omit maps (mesh surface) are shown for the tryptophan side chains. $2mF_o–DF_c$ maps (mesh surface) for xenon atoms are contoured at 1σ (see **Figure A.1** for anomalous xenon density). The tunnel network was modeled with CAVER using the WT *Ns* H-NOX structure.

unit cell dimensions as WT *Ns* H-NOX (**Table A.2**), providing initial evidence that introduction of the tryptophan residues did not significantly alter the native fold. The final crystal structures were found to superimpose well with the WT protein (**Figure A.4**). C_α rmsd values of 0.273, 0.286, and 0.158 Å were obtained for L66W, L67W, and L66W/L67W, respectively (using molecule A of each structure).

Closer inspection of the tryptophans in each crystal structure show that the side chains were incorporated within the tunnel network as expected. Simulated-annealing composite omit maps for the L66W and L67W side chains show unambiguous electron density from the tryptophan indole rings (**Figure 2.3**). These side chains make tight van der Waals contact with the surrounding, predominately hydrophobic residues in the tunnels. The tryptophan indole ring in the L66W single mutant is packed tightly by I9, M12, I13, V52, A55, L59, L67, and F70 at the top of tunnel 1. The tryptophan indole ring in the L67W single mutant is tightly contacted by T48, V52, F70, and L141 as well as the sulfur atom of M144 and the face of the Y49 phenol ring. Notably, the large tryptophan side chains appear to fit into the open space in the tunnel

network and sterically seal tunnel 1 and tunnel 2. Decreased B-factors in the crystal structures at these sites support tight van der Waals contacts between the tryptophan side chains and tunnel residues and suggest that introduction of the tryptophan residues locally enhances conformational rigidity.

The tryptophan side chains in molecule A of the double mutant (L66W/L67W) are in the same orientation as the single mutants and contacts with surrounding residues in the tunnels are preserved (**Figure 2.3**). Additionally, the edge of the L66W residue is in van der Waals contact with the face of the L67W indole ring. In molecule B of the double mutant, the L66W side chain is in at least one different rotameric position than in molecule A but still functions to partially seal the tunnel (**Figure A.5**). The different observable rotamers of L66W suggest that this side chain has enhanced flexibility in the double mutant structure.

To examine the effect of blocking the tunnels on gas accessibility in *Ns* H-NOX, crystals of L66W were subsequently pressurized with xenon. L66W was selected as a representative mutant because it is predicted to block the main pathway (tunnel 1) for xenon diffusion between the solvent and protein interior. The structure of L66W under 6 atm of xenon was obtained for direct comparison to WT *Ns* H-NOX (**Table A.2**). As seen in the 1.99 Å resolution structure (0.071 Å C_α rmsd vs. native L66W), introduction of the tryptophan residue in tunnel 1 sterically blocks xenon binding at the former Xe3 position but preserves the Xe1 and Xe2 sites (**Figure 2.3** and **Figure A.1**). Retention of xenon binding in the single mutant reflects the ability of xenon to access the base of the channel through other pathway(s). This suggests that tunnel 2 could serve as a possible conduit for gases even though xenon occupancy remains to be observed in that tunnel directly.

Together the structural data indicate that the *Ns* H-NOX tunnel network was blocked by introducing tryptophan residues and that these residues sterically control gas migration in the protein interior. The ability to modify the protein without significant structural changes suggests that this approach represents a unique opportunity to systematically dissect the contribution of the H-NOX tunnels to ligand binding kinetics at the heme.

Blocking the tunnels affects the CO k_{on}. To examine how blocking the tunnel network affects ligand association rates, time-resolved absorption spectroscopies using CO gas were employed with the tryptophan variants. CO has several important advantages over NO as a spectroscopic tool to probe ligand migration in heme proteins: **(1)** CO reacts more slowly (~100-1000 fold) with ferrous heme (40), **(2)** CO has been previously shown to both bind to and dissociate from the *Ns* H-NOX heme in a simple 1-step process (40), and **(3)** CO does not participate in redox chemistry with proteins (41). Two likely outcomes were predicted for blocking the tunnels with respect to ligand binding. Blocking the tunnels could decrease CO association rate constants (k_{on} values or "on-rates") if diffusion into the heme pocket were dramatically slowed. Alternatively, on-rates could increase if ligand trapping in the heme pocket were enhanced (following ligand diffusion through the protein matrix) due to the blocking of route(s) for ligand escape.

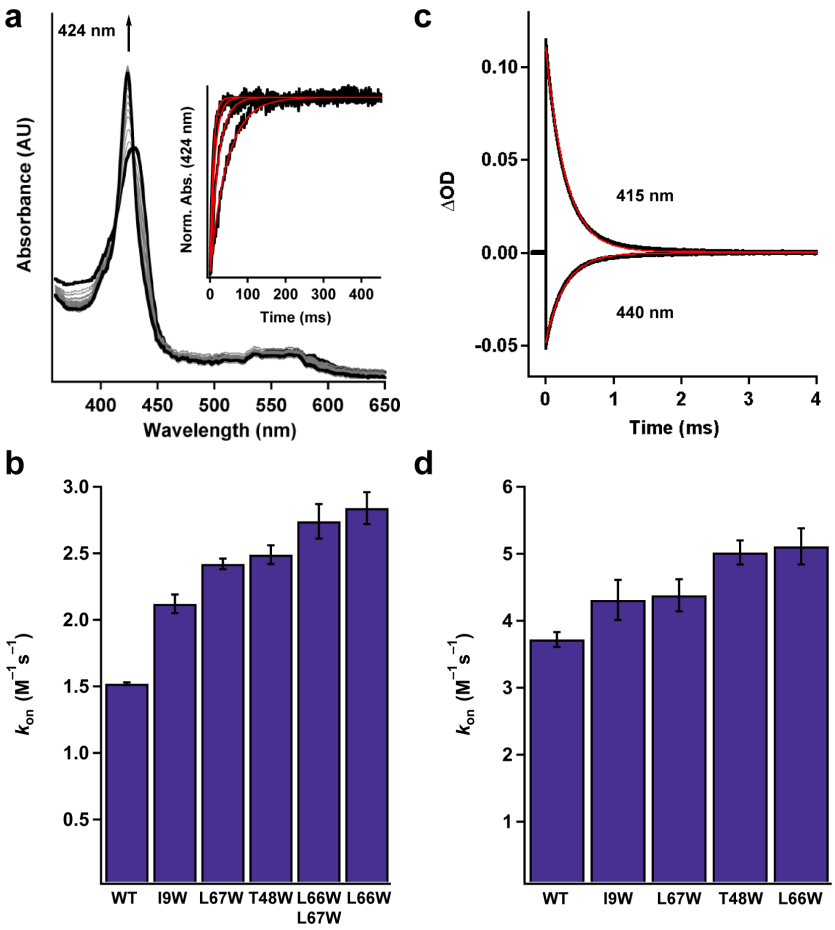

Figure 2.4 Determination of CO k_{on} values (x 10^6 $M^{-1}s^{-1}$) for the *Ns* H-NOX variants. **(a)** Time-resolved UV–visible spectra of CO binding to WT ferrous *Ns* H-NOX in a stopped flow spectrometer (11.9 μM CO data is shown). **(Inset, a)** Single wavelength stopped flow traces of the absorbance at 424 nm versus time for WT *Ns* H-NOX in the presence of varying CO concentrations. **(b)** Summary of CO k_{on} values for the *Ns* H-NOX variants determined with stopped flow spectroscopy (see **Figure A.6** for a plot of k_{obs} versus CO concentration). N = 3-5. Error represents the standard deviation. **(c)** Transient absorption traces of CO binding to WT ferrous *Ns* H-NOX under 1 atm of CO following laser photolysis. The trace at 440 nm represents the loss of the Fe^{II}–unligated species, and the trace at 415 nm represents the formation of the Fe^{II}–CO species. **(d)** Summary of CO k_{on} values for all the *Ns* H-NOX variants determined with laser photolysis. N = 2. Error represents the standard deviation.

CO on-rates for the tryptophan variants were measured with stopped flow spectroscopy in a manner similar to that described previously (40). Ferrous protein was rapidly mixed with increasing CO concentrations, and CO binding was followed using a diode array detector on a stopped flow instrument (**Figure 2.4A**). Plots of observed rate (k_{obs}) versus CO concentration (**Figure A.6**) were used to calculate k_{on} values from the slope of the linear fits. WT *Ns* H-NOX had a CO k_{on} of 1.52 x 10^6 $M^{-1}s^{-1}$, which is comparable to the previously reported value (40). To our initial surprise, all the tunnel-blocking variants exhibited faster CO k_{on} values compared to the WT protein. The on-rate for L67W (blocking tunnel 2) increased by 50%, while the on-rates for L66W (blocking tunnel 1) and L66W/L67W increased by approximately 100% relative to the WT protein (**Figure 2.4B** and **Table 2.1**). These data indicate that even with blocking the tunnels, CO is still able to rapidly diffuse through the protein matrix, which likely occurs within the dead time of the stopped flow measurement (<1.5 ms). Therefore, CO on-rates determined

with stopped flow spectroscopy appear to reflect CO binding following diffusion from both the solvent and protein scaffold. In agreement with the xenon pressurization data, the most significant changes in rate are observed upon blocking tunnel 1, which suggests that it is a more favorable ligand migration pathway.

Table 2.1 CO binding constants for *Ns* H-NOX and selected H-NOX proteins

Protein	CO k_{on} (x 10^6 $M^{-1}s^{-1}$)		CO k_{off} (s^{-1})	CO K_D[a] (μM)	*Ref.*[b]
	Laser Photolysis	Stopped Flow			
***Ns* H-NOX**					
Wild-type	3.7 ± 0.1	1.52 ± 0.01	6.73 ± 0.42	4.42 ± 0.28	
L67W	4.4 ± 0.2	2.42 ± 0.04	6.71 ± 0.15	2.78 ± 0.08	
L66W	5.1 ± 0.3	2.84 ± 0.12	7.36 ± 0.62	2.59 ± 0.24	
L66W/L67W	N/D	2.74 ± 0.13	5.36 ± 0.20	1.96 ± 0.12	
T48W	5.0 ± 0.2	2.49 ± 0.07	4.13 ± 0.54	1.66 ± 0.22	
I9W	4.3 ± 0.3	2.12 ± 0.07	7.00 ± 0.18	3.30 ± 0.14	
***Tt* H-NOX**	4.1 ± 0.2	2.18 ± 0.09	3.56 ± 0.42	1.63 ± 0.20	
sGC	N/D	0.0358 ± 0.0015	3.5 ± 0.5	98 ± 15	*(54)*

[a] Calculated from k_{off}/k_{on} using stopped flow data. [b] This work unless otherwise noted. N/D = not determined. Error (±) represents the standard deviation.

To confirm the increases observed in CO on-rates when the tunnels are blocked, tryptophan residues were also engineered at the I9 and T48 positions in the tunnel network. I9 and T48 are located on different α-helices than L66W and L67W (**Figure 2.2**). Based on modeling of allowed tryptophan rotamers (38), the T48W side chain is predicted to be incorporated near the branch point between tunnel 1 and tunnel 2, and the I9W side chain is predicted to be incorporated further away from the heme in tunnel 1 in between the locations of T48W and L66W (**Figure A.7**). The I9W and T48W single mutants were generated as described above. As with the other variants, UV–visible spectra obtained for T48W and I9W heme-ligand complexes were very similar to the WT protein (**Table A.4**), again suggesting that the tryptophan residues did not greatly alter the electronic properties of the heme. Characterization of CO on-rates with stopped flow spectroscopy illustrated that the CO k_{on} values for I9W and T48W are faster than WT. The T48W variant in particular exhibited a greater increase in rate that is similar to L66W and the L66W/L67W double mutant (**Figure 2.4B** and **Table 2.1**). The increases in ligand on-rates across a broad panel of tunnel-blocking mutants suggest that the kinetic trend is a general phenomenon.

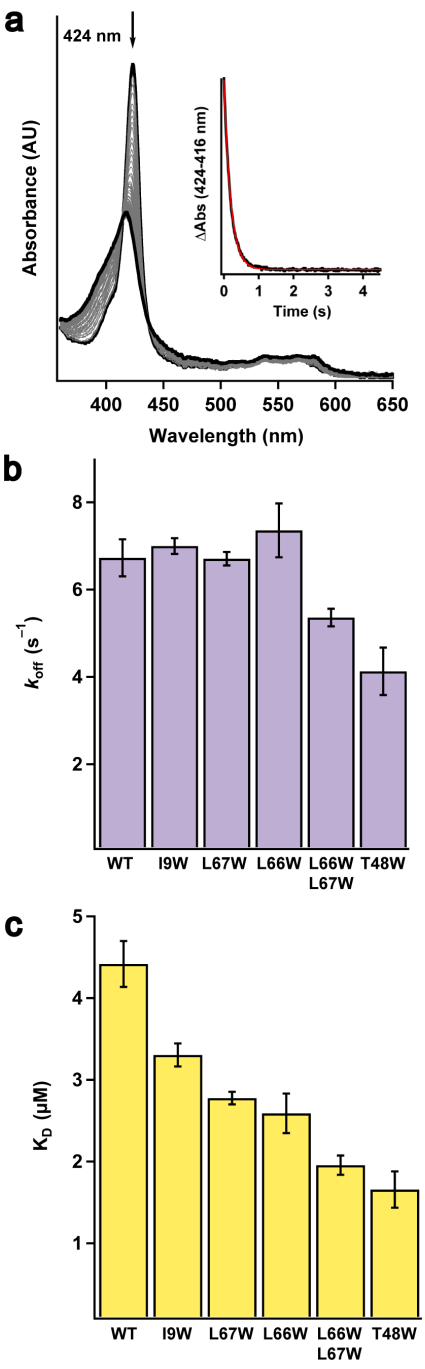

Figure 2.5 Determination of CO k_{off} and K_D values for the *Ns* H-NOX variants. **(a)** Time-resolved UV–visible spectra of CO dissociation from Fe^{II}– CO WT *Ns* H-NOX in the presence of an NO trap in a stopped flow spectrometer. **(Inset, a)** Absorbance at 424 nm vs. time for CO dissociation from WT *Ns* H-NOX. **(b)** Summary of CO k_{off} values. N ≥ 3. Error represents the standard deviation. **(c)** Summary of CO K_D values for all the *Ns* H-NOX variants. K_D values were obtained from k_{off}/k_{on}.

To eliminate the requirement for CO diffusion into the heme pocket during data acquisition, association kinetics were also evaluated in the tryptophan variants under a CO-equilibrated atmosphere using laser photolysis (42). Ferrous *Ns* H-NOX was incubated anaerobically overnight under 1 atm of CO to ensure full sample equilibration. Photolysis of the Fe^{II}–CO bond was carried out using 560 nm laser irradiation to transiently form the Fe^{II}–unligated heme. CO binding was subsequently followed over a 10 ms timescale (**Figure 2.4C**) (26, 42). A CO k_{on} value of 3.7 x 10^6 $M^{-1}s^{-1}$ was obtained for WT *Ns* H-NOX. This rate is somewhat faster than the CO on-rate (1.52 x 10^6 $M^{-1}s^{-1}$) observed in the stopped flow experiment, which could reflect different protein conformational changes formed upon photodissociation of the CO ligand. Importantly, the relative trend in CO on-rates for the tunnel-blocking variants obtained with laser photolysis parallels what was observed in the stopped flow experiment. WT *Ns* H-NOX exhibited the slowest on-rate, and the tunnel-blocking mutants exhibited faster rates with L66W showing the greatest increase (**Figure 2.4D** and **Table 2.1**). The lack of significant structural changes in the tryptophan variants suggests that the faster ligand on-rates are due to more efficient ligand trapping in the protein interior. Blocking the tunnels both individually and together appears to eliminate routes of ligand diffusion from the protein to the solvent, increasing the effective CO concentration near the heme and the subsequent rate of CO binding to the iron.

Blocking the tunnels decreases the CO k_{off} and enhances CO binding affinity. To examine if increased ligand trapping in the heme pocket also affects CO dissociation kinetics, dissociation rate constants (k_{off} values or "off-rates") were measured for the *Ns* H-NOX variants using stopped flow spectroscopy in the presence of an NO trap (40, 42). An NO trap was utilized in order to limit CO rebinding following CO release from the heme. NO reacts quickly

(~10^8 $M^{-1}s^{-1}$) with ferrous heme and binds with high affinity (K_D ~pM) such that CO is not able to displace NO once it is coordinated to the iron (40, 42). WT *Ns* H-NOX was found to have a CO k_{off} value of 6.73 s^{-1} (**Figure 2.5A**), which is comparable to that reported previously (40). Several of the single tryptophan tunnel-blocking mutants (I9W, L66W, and L67W) had no significant change in CO off-rate. However, the L66W/L67W double mutant and the T48W mutant exhibited slower rates than WT (**Figure 2.5B** and **Table 2.1**). It appears that blocking both tunnels is necessary to elicit an effect on CO k_{off} values. These tryptophan residues likely decrease the CO off-rate by increasing rapid CO recombination to the heme following transient dissociation.

Calculation of CO K_D values (k_{off}/k_{on}) shows that blocking the tunnels increases CO binding affinity up to ~2.5 fold or ~2.2 fold in the T48W mutant based on stopped-flow and photolysis data, respectively (**Figure 2.5C** and **Table 2.1**). The enhancement in ligand affinity is due to an increase in CO on-rate and decrease in CO off-rate, which appears to be associated with better ligand trapping in the heme pocket (**Figure 2.6**). Additionally, the enhanced ligand affinity in the smaller cavity is likely thermodynamically favorable due to a decreased entropic penalty associated with ligand binding (16). Together these data attest to the ability of H-NOX protein scaffolds to modulate ligand flux through the protein interior and implicates a role for protein tunnels in tuning ligand-binding properties in the H-NOX family.

Discussion

Extensive studies on the globins have provided a model for how heme protein scaffolds control ligand binding (16, 17). Myoglobin, for example, has a heme group surrounded by deep gas pockets that work to efficiently capture and release O_2 (16, 17). H-NOX protein scaffolds possess a novel fold and, unlike the globins, bind a heme cofactor that is completely buried within the protein interior. This framework appears to funnel gases toward the heme pocket and tune gas-sensing properties for involvement in diverse signaling pathways.

Much work has elucidated important determinants of ligand binding in the H-NOX family (25-30). However, the direct role of the protein scaffold in modulating ligand binding from sites beyond the heme pocket has not been previously addressed. Utilizing X-ray crystallography with xenon and kinetic measurements, a tunnel network has been mapped in a non-O_2-binding H-NOX protein (*Ns* H-NOX) that appears to be conserved in H-NOX proteins with similar ligand-binding properties. The tunnel network consists of a Y-shaped, hydrophobic channel that serves as a pathway for gas diffusion to and from the heme (**Figure 2**). Blocking the tunnel network influences heme ligand-binding kinetics – increasing ligand on-rates and decreasing ligand off-rates. These changes appear to be due to better ligand trapping near the heme, which results from removing pathways for ligand escape to the solvent (**Figure 2.6**).

Although globins and H-NOX domains have unique interior routes for ligand diffusion, comparison between these protein families shows that divergent topological features may tune reversible ligand binding in parallel ways. Similar to *Ns* H-NOX, mutagenesis studies in myoglobin have found that mutations that vary the size and character of cavities affect affinity by modifying the occupation and migration of ligands (16, 17). This is reflected in O_2 photolysis experiments on short time scales (ns-μs) where blocking the gas pocket distal to the heme

increases the fraction and rate of geminate ligand rebinding (16, 17). However, unlike *Ns* H-NOX, decreasing the interior cavity volume in myoglobin with structure-guided mutagenesis is associated with slowed ligand on-rates (16, 17). This is likely due to less efficient ligand capture in myoglobin's more open heme site where decreasing the interior cavity volume appears to preferentially favor ligand escape (16, 17).

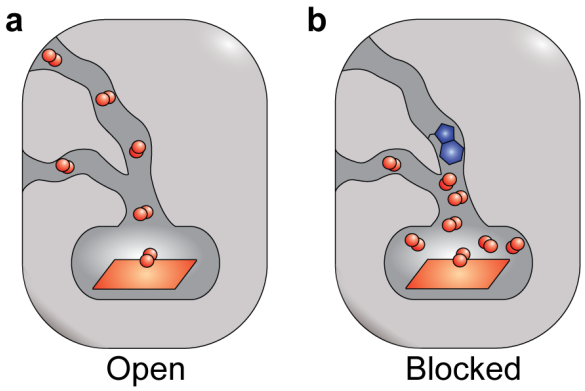

Figure 2.6 Tunnel-blocking mutants modulate heme ligand-binding properties in H-NOX proteins by altering ligand migration. **(a)** A native H-NOX protein and **(b)** an H-NOX protein with tunnel 1 blocked are shown. A tryptophan residue is shown in blue and diatomic ligands are shown in red. Blocking the tunnels individually (L66W and L67W mutants) and together (L66W/L67W mutant) in *Ns* H-NOX increases ligand trapping in the protein interior. This functions to both increase the CO k_{on} following CO diffusion through the protein scaffold and decrease the CO k_{off}. These kinetic trends appear to be due to the elimination of route(s) for ligand escape.

To provide initial insight into ligand migration in H-NOX proteins, a molecular dynamics (MD) study was conducted (33). The results of the MD simulations are in agreement with the ligand diffusion pathways observed here. Additionally, the calculations show that the presence of preformed pathways in *Ns* H-NOX increases the rate of CO escape to solvent relative to *Tt* H-NOX, which does not have an open tunnel network (**Figure A.3**) (33). This observation is consistent with the experimentally determined CO dissociation rates for both proteins reported in the present study (**Table 2.1**) and supports the hypothesis that blocking protein tunnels increases ligand capture.

Protein dynamics in H-NOX domains could work in concert with tunnels to control ligand diffusion to and from the heme pocket. A MD simulation carried out on *Tt* H-NOX, for example, led to the conclusion that the protein fluctuates near the heme edge to permit ligand flux (33). The potential role of transiently formed pathways in facilitating ligand access is particularly evident in *Ns* H-NOX when both tunnels are blocked. It is possible that the introduction of bulky residues could alter protein dynamics in a manner not evident in the structural data to form additional routes for ligand diffusion. Potential changes in dynamics in the mutants could also dampen our observed kinetic effects. Importantly, these transient pathways appear less important in the native *Ns* H-NOX scaffold where both computational and experimental data suggest that the open tunnel network represents the most favorable route for gas diffusion.

Differences in ligand flux between divergent classes of H-NOX proteins may influence ligand specificity. In H-NOX proteins that bind O_2, the absence of preformed tunnels could work in concert with H-bonding residues to trap O_2 at the heme iron and tighten O_2 affinity through

enhancing ligand rebinding (33). Most bacterial O_2-binding H-NOX domains identified to date are in obligate anaerobes where a high O_2 affinity would be important to sense and respond to low amounts of environmental O_2 (24). In non-O_2-binding H-NOX proteins, the tunnel network appears to permit more ligand flux through the heme pocket. This could favor NO binding under aerobic conditions since NO binds to ferrous heme with higher intrinsic affinity than O_2 (42). The potential ability to tune ligand-binding properties with distinct interior architectures may reflect the co-evolution of ligand diffusion pathways and diverse H-NOX protein functions.

Internal topological features in numerous proteins are essential for controlling the capture and release of biomolecules. For example, in NiFe hydrogenase, tunnels have been shown to promote H_2 back-exchange with solvent but also facilitate the escape of inhibitory amounts of CO (4); in superoxide dismutase, a positively charged cleft steers O_2^- to the active site, enabling nearly diffusion-limited turnover rates (43); and in soybean lipoxygenase, the route of O_2 migration into the active site influences product regiochemistry (2). Results reported here show that a tunnel network in H-NOX heme sensor domains guides gases to the heme iron and also tunes reversible gas binding by establishing routes for ligand diffusion. Together, our findings reflect the tightly coordinated relationship between protein frameworks and protein function. Structural features are employed in proteins not only to directly participate in active site chemistry but also control the flux of biomolecules. A deeper understanding of this complex relationship is essential to unraveling protein mechanisms and predicting biochemical properties across diverse protein families.

References

1. Baron R, Riley C, Chenprakhon P, Thotsaporn K, Winter RT, Alfieri A, Forneris F, van Berkel WJ, Chaiyen P, Fraaije MW, *et al*. (2009) Multiple pathways guide oxygen diffusion into flavoenzyme active sites. *Proc Natl Acad Sci U S A* 106: 10603-10608.
2. Knapp MJ, Seebeck FP, & Klinman JP (2001) Steric control of oxygenation regiochemistry in soybean lipoxygenase-1. *J Am Chem Soc* 123: 2931-2932.
3. Igarashi RY & Seefeldt LC (2003) Nitrogen fixation: the mechanism of the Mo-dependent nitrogenase. *Crit Rev Biochem Mol Biol* 38: 351-384.
4. Leroux F, Dementin S, Burlat B, Cournac L, Volbeda A, Champ S, Martin L, Guigliarelli B, Bertrand P, Fontecilla-Camps J, *et al*. (2008) Experimental approaches to kinetics of gas diffusion in hydrogenase. *Proc Natl Acad Sci U S A* 105: 11188-11193.
5. Doukov TI, Iverson TM, Seravalli J, Ragsdale SW, & Drennan CL (2002) A Ni-Fe-Cu center in a bifunctional carbon monoxide dehydrogenase/acetyl-CoA synthase. *Science* 298: 567-572.
6. Manjasetty BA, Powlowski J, & Vrielink A (2003) Crystal structure of a bifunctional aldolase-dehydrogenase: sequestering a reactive and volatile intermediate. *Proc Natl Acad Sci U S A* 100: 6992-6997.
7. Lund L, Fan Y, Shao Q, Gao YQ, & Raushel FM (2010) Carbamate transport in carbamoyl phosphate synthetase: a theoretical and experimental investigation. *J Am Chem Soc* 132: 3870-3878.
8. Hyde CC, Ahmed SA, Padlan EA, Miles EW, & Davies DR (1988) Three-dimensional structure of the tryptophan synthase alpha 2 beta 2 multienzyme complex from Salmonella typhimurium. *J Biol Chem* 263: 17857-17871.

9. Tilton RF, Jr., Kuntz ID, Jr., & Petsko GA (1984) Cavities in proteins: structure of a metmyoglobin-xenon complex solved to 1.9 A. *Biochemistry* 23: 2849-2857.
10. Austin RH, Beeson KW, Eisenstein L, Frauenfelder H, & Gunsalus IC (1975) Dynamics of ligand binding to myoglobin. *Biochemistry* 14: 5355-5373.
11. Schlichting I, Berendzen J, Phillips GN, Jr., & Sweet RM (1994) Crystal structure of photolysed carbonmonoxy-myoglobin. *Nature* 371: 808-812.
12. Schotte F, Lim M, Jackson TA, Smirnov AV, Soman J, Olson JS, Phillips GN, Jr., Wulff M, & Anfinrud PA (2003) Watching a protein as it functions with 150-ps time-resolved x-ray crystallography. *Science* 300: 1944-1947.
13. Cohen J, Arkhipov A, Braun R, & Schulten K (2006) Imaging the migration pathways for O_2, CO, NO, and Xe inside myoglobin. Biophys J 91: 1844-1857.
14. Elber R (2010) Ligand diffusion in globins: simulations versus experiment. *Curr Opin Struct Biol* 20: 162-167.
15. Ringe D, Petsko GA, Kerr DE, & Ortiz de Montellano PR (1984) Reaction of myoglobin with phenylhydrazine: a molecular doorstop. *Biochemistry* 23: 2-4.
16. Olson JS, Soman J, & Phillips GN, Jr. (2007) Ligand pathways in myoglobin: a review of Trp cavity mutations. *IUBMB Life* 59: 552-562.
17. Scott EE, Gibson QH, & Olson JS (2001) Mapping the pathways for O_2 entry into and exit from myoglobin. *J Biol Chem* 276: 5177-5188.
18. Salter MD, Nienhaus K, Nienhaus GU, Dewilde S, Moens L, Pesce A, Nardini M, Bolognesi M, & Olson JS (2008) The apolar channel in Cerebratulus lacteus hemoglobin is the route for O_2 entry and exit. *J Biol Chem* 283: 35689-35702.
19. Milani M, Pesce A, Ouellet Y, Dewilde S, Friedman J, Ascenzi P, Guertin M, & Bolognesi M (2004) Heme-ligand tunneling in group I truncated hemoglobins. *J Biol Chem* 279: 21520-21525.
20. de Sanctis D, Dewilde S, Pesce A, Moens L, Ascenzi P, Hankeln T, Burmester T, & Bolognesi M (2004) Crystal structure of cytoglobin: the fourth globin type discovered in man displays heme hexa-coordination. *J Mol Biol* 336: 917-927.
21. Pesce A, Dewilde S, Nardini M, Moens L, Ascenzi P, Hankeln T, Burmester T, & Bolognesi M (2003) Human brain neuroglobin structure reveals a distinct mode of controlling oxygen affinity. *Structure* 11: 1087-1095.
22. Hargrove MS, Barry JK, Brucker EA, Berry MB, Phillips GN, Jr., Olson JS, Arredondo-Peter R, Dean JM, Klucas RV, & Sarath G (1997) Characterization of recombinant soybean leghemoglobin a and apolar distal histidine mutants. *J Mol Biol* 266: 1032-1042.
23. Vallone B, Nienhaus K, Matthes A, Brunori M, & Nienhaus GU (2004) The structure of carbonmonoxy neuroglobin reveals a heme-sliding mechanism for control of ligand affinity. *Proc Natl Acad Sci U S A* 101: 17351-17356.
24. Boon EM & Marletta MA (2005) Ligand discrimination in soluble guanylate cyclase and the H-NOX family of heme sensor proteins. *Curr Opin Chem Biol* 9: 441-446.
25. Boon EM, Huang SH, & Marletta MA (2005) A molecular basis for NO selectivity in soluble guanylate cyclase. *Nat Chem Biol* 1: 53-59.
26. Weinert EE, Plate L, Whited CA, Olea C, Jr., & Marletta MA (2009) Determinants of ligand affinity and heme reactivity in H-NOX domains. *Angew Chem Int Ed Engl* 49: 720-723.

27. Rothkegel C, Schmidt PM, Stoll F, Schroder H, Schmidt HH, & Stasch JP (2006) Identification of residues crucially involved in soluble guanylate cyclase activation. *FEBS Lett* 580: 4205-4213.
28. Martin E, Berka V, Bogatenkova E, Murad F, & Tsai AL (2006) Ligand selectivity of soluble guanylyl cyclase: effect of the hydrogen-bonding tyrosine in the distal heme pocket on binding of oxygen, nitric oxide, and carbon monoxide. *J Biol Chem* 281: 27836-27845.
29. Derbyshire ER, Deng S, & Marletta MA (2010) Incorporation of tyrosine and glutamine residues into the soluble guanylate cyclase heme distal pocket alters NO and O_2 binding. *J Biol Chem* 285: 17471-17478.
30. Olea C, Boon EM, Pellicena P, Kuriyan J, & Marletta MA (2008) Probing the function of heme distortion in the H-NOX family. *ACS Chem Biol* 3: 703-710.
31. Pellicena P, Karow DS, Boon EM, Marletta MA, & Kuriyan J (2004) Crystal structure of an oxygen-binding heme domain related to soluble guanylate cyclases. *Proc Natl Acad Sci U S A* 101: 12854-12859.
32. Ma X, Sayed N, Beuve A, & van den Akker F (2007) NO and CO differentially activate soluble guanylyl cyclase via a heme pivot-bend mechanism. *EMBO J* 26: 578-588.
33. Zhang Y, Lu M, Cheng Y, & Li Z (2010) H-NOX domains display different tunnel systems for ligand migration. *J Mol Graph Model* 28: 814-819.
34. Marassio G, Prange T, David HN, Sopkova-de Oliveira Santos J, Gabison L, Delcroix N, Abraini JH, & Colloc'h N (2011) Pressure-response analysis of anesthetic gases xenon and nitrous oxide on urate oxidase: a crystallographic study. *FASEB J* 25: 2266-2275.
35. Bondi A (1964) van der Waals Volumes and Radii. J. Phys. Chem. 68: 441-451.
36. Quillin ML, Breyer WA, Griswold IJ, & Matthews BW (2000) Size versus polarizability in protein-ligand interactions: binding of noble gases within engineered cavities in phage T4 lysozyme. *J Mol Biol* 302: 955-977.
37. Beneš P, Chovancová E, Kozlíková B, Pavelka A, Strnad O, Brezovský J, Šustr V, Klvaňa M, Szabó T, Gora A, *et al*. (2010) CAVER 2.1, software.
38. Emsley P & Cowtan K (2004) Coot: model-building tools for molecular graphics. *Acta Crystallogr D Biol Crystallogr* 60: 2126-2132.
39. Abraham DJ & Leo AJ (1987) Extension of the fragment method to calculate amino acid zwitterion and side chain partition coefficients. *Proteins* 2: 130-152.
40. Tsai AL, Berka V, Martin F, Ma X, van den Akker F, Fabian M, & Olson JS (2010) Is Nostoc H-NOX a NO sensor or redox switch? *Biochemistry* 49: 6587-6599.
41. Tannenbaum SR & White FM (2006) Regulation and specificity of S-nitrosylation and denitrosylation. *ACS Chem Biol* 1: 615-618.
42. Rohlfs RJ, Mathews AJ, Carver TE, Olson JS, Springer BA, Egeberg KD, & Sligar SG (1990) The effects of amino acid substitution at position E7 (residue 64) on the kinetics of ligand binding to sperm whale myoglobin. *J Biol Chem* 265: 3168-3176.
43. Getzoff ED, Cabelli DE, Fisher CL, Parge HE, Viezzoli MS, Banci L, & Hallewell RA (1992) Faster superoxide dismutase mutants designed by enhancing electrostatic guidance. *Nature* 358: 347-351.
44. Karow DS, Pan D, Tran R, Pellicena P, Presley A, Mathies RA, & Marletta MA (2004) Spectroscopic characterization of the soluble guanylate cyclase-like heme domains from *Vibrio cholerae* and *Thermoanaerobacter tengcongensis*. *Biochemistry* 43: 10203-10211.

45. Winter MB, McLaurin EJ, Reece SY, Olea C, Jr., Nocera DG, & Marletta MA (2010) Ru-porphyrin protein scaffolds for sensing O_2. *J Am Chem Soc* 132: 5582-5583.
46. Soltis SM, Stowell MHB, Wiener MC, Phillips GN, & Rees DC (1997) Successful flash-cooling of xenon-derivatized myoglobin crystals. *J Appl Crystallogr* 30: 190-194.
47. Otwinowski A & Minor W (1997) Processing of X-ray diffraction data collected in oscillation mode. *Methods Enzymol* 276: 307-326.
48. McCoy AJ, Grosse-Kunstleve RW, Storoni LC, & Read RJ (2005) Likelihood-enhanced fast translation functions. *Acta Crystallogr D Biol Crystallogr* 61: 458-464.
49. Lamzin VS, Perrakis A, & Wilson KS (2001) in International Tables for Crystallography, eds. Rossmann MG & Arnold E (Kluwer Academic Publishers, Dordrecht, Netherlands), pp. 720-722.
50. Adams PD, Grosse-Kunstleve RW, Hung LW, Ioerger TR, McCoy AJ, Moriarty NW, Read RJ, Sacchettini JC, Sauter NK, & Terwilliger TC (2002) PHENIX: building new software for automated crystallographic structure determination. *Acta Crystallogr D Biol Crystallogr* 58: 1948-1954.
51. Davis IW, Leaver-Fay A, Chen VB, Block JN, Kapral GJ, Wang X, Murray LW, Arendall WB, 3rd, Snoeyink J, Richardson JS, *et al*. (2007) MolProbity: all-atom contacts and structure validation for proteins and nucleic acids. *Nucleic Acids Res* 35: W375-383.
52. Laskowski RA, MacArthur MW, Moss DS, & Thornton JM (1993) PROCHECK: A program to check the stereochemical quality of protein structures. *J Appl Crystallogr* 26: 283-291.
53. Dempsey JL, Winkler JR, & Gray HB (2010) Kinetics of electron transfer reactions of H2-evolving cobalt diglyoxime catalysts. *J Am Chem Soc* 132: 1060-1065.
54. Stone JR, Sands RH, Dunham WR, & Marletta MA (1996) Spectral and ligand-binding properties of an unusual hemoprotein, the ferric form of soluble guanylate cyclase. *Biochemistry* 35: 3258-3262.
55 Stone JR & Marletta MA (1994) Soluble guanylate cyclase from bovine lung: Activation with nitric oxide and carbon monoxide and spectral characterization of the ferrous and ferric states. *Biochemistry* 33: 5636-5640.

CHAPTER 3

Structural Insights into the Role of Iron-Histidine Bond Cleavage in NO-Induced Activation of H-NOX Proteins·

Summary

A key molecular event during NO-induced activation of H-NOX proteins is loss of the heme-histidine bond and formation of a five-coordinate nitrosyl complex. Although this has been known for quite some time, molecular level details into this process have remained elusive. In this chapter, high-resolution crystal structures of the H-NOX protein from *Shewanella oneidensis* in the unliganded, as well as both six-coordinate and five-coordinate nitrosyl states are reported. From these structures, it is evident that several structural features in the heme pocket of the unliganded state maintain a distorted heme that – following loss of the iron-histidine bond and structural rearrangements in the heme pocket – relaxes towards planarity to yield the active, NO-bound conformation. Additionally, the first observation of non-heme metal coordination in a H-NOX protein is presented.

Introduction

Nitric oxide (NO) is a freely diffusible radical gas that is critical to numerous eukaryotic processes, such as blood vessel homeostasis and neurotransmission (1, 2). An integral component of mammalian NO signaling is soluble guanylate cyclase (sGC), the primary receptor for NO (3-5). The binding of NO to the heme cofactor of sGC increases guanylate cyclase activity by several hundredfold, resulting in activation of cyclic guanosine monophosphate (cGMP)-dependent signaling pathways. The interaction of NO with the histidyl-ligated heme cofactor of sGC has been extensively studied through biochemical and spectroscopic means, providing an overarching model of NO-induced activation. NO binds to the ferrous (Fe^{II}) heme of sGC at the open coordination site, axial to the heme-ligating histidine, to form a transient six-coordinate nitrosyl complex. NO association severely weakens the iron-histidine bond, resulting in histidine dissociation and the formation of an activated five-coordinate, NO-bound heme (**Figure 3.1A and 3.1B**) (6-9). Rupture of the iron-histidine bond is the key molecular switch that stimulates sGC activity (reviewed in (10)). However, due to limited structural data, a detailed molecular model regarding the binding of NO to the heme and propagation of this signal have remained elusive.

Significant advances in understanding the mechanism of sGC activation have resulted from studies involving homologous prokaryotic proteins from the Heme-Nitric oxide/Oxygen binding (H-NOX) family of receptors (11-14). These bacterial homologs share similar spectroscopic properties, high sequence homology (18-40%), and key conserved residues with

---

· The work described in this chapter was done in collaboration with Rohan Jonnalagadda in Prof. John Kuriyan's laboratory (UC Berkeley) and Prof. John Kuriyan (UC Berkeley). R.J. aided in obtaining protein for crystallization as well as collecting X-ray diffraction data. R.J. and J.K. aided in data analysis.

the sGC heme pocket and therefore, have served as important models of the sGC heme domain (15, 16).

Previous structural studies to probe the NO activation mechanism in H-NOX proteins have relied on structural mimics, wherein the heme-ligating histidine residue had been substituted with a glycine and heme binding rescued using imidazole as a surrogate for the histidine side chain (13, 14). Analyses of these structural mimics demonstrated that artificially "cleaving" the heme-histidine bond elicits a conformational change involving a rotation of the distal subdomain relative to the proximal subdomain, centered about the heme cofactor. Further analysis showed that, alongside this conformational change, severing of the iron-histidine bond results in a more planar heme. The relationship between heme and protein conformation was first noted in the H-NOX crystal structure from *Thermoanaerobacter tengcongensis*, wherein the two distinct protein conformations observed crystallographically correlate well with the overall degree of heme distortion (11). The pronounced distortion of the heme from planarity is the result of van der Waals interactions with residues I5 and P115 that flank the distal and proximal faces of the heme, respectively. Removal of the steric bulk imparted by P115, a residue that is strictly conserved in H-NOX proteins, resulted in a significantly more planar heme (17) and the same conformational change that was observed upon mimicking heme-histidine cleavage (13, 14).

From these studies, a heme-strain model of NO activation was proposed. In this model, in the basal, ferrous-unliganded state the heme is distorted from planarity due to steric interactions with key conserved residues in the heme pocket. NO binding and ultimate scission of the iron-histidine bond releases the steric strain imparted on the heme, allowing it to relax to planarity and, via intimate interactions of the protein and heme, elicit a rotation of the distal subdomain with respect to the proximal subdomain. This conformational change thus is hypothesized to communicate NO binding to downstream signaling partners.

Although these prior studies provided a structural description of conformation changes associated with rupture of the iron-histidine bond, structure determination employed heme ligands and mutations within the αF, or signaling helix, that do not accurately represent the native H-NOX signaling species. As such, crucial structural changes involving the heme-ligating histidine were absent. The present study provides molecular-level insight into NO-induced activation of H-NOX proteins through high-resolution crystal structures of distinct states along the NO activation pathway. Reported structures include the inactive ferrous-unliganded, as well as both the intermediate six-coordinate and activated five-coordinate NO-bound states of the H-NOX protein from *Shewanella oneidensis* (*So* H-NOX), which has high homology and similar ligand binding properties to sGC. Structures presented here provide the first high-resolution snapshots of key steps in the NO activation trajectory and expand previous work on key structural changes that propagate the NO binding event. Together these data show that several structural features in the heme pocket of the ferrous-unliganded H-NOX maintain a distorted heme that – following NO-induced scission of the iron-histidine bond and subsequent structural rearrangements in the proximal heme pocket – relaxes towards planarity to yield the active H-NOX protein conformation. Additionally, the first observation of a non-heme metal coordination site in an H-NOX protein is also presented.

Methods

Protein expression and purification. The gene for *So* H-NOX (residues 1-181 of SO2144 from *Shewanella oneidensis* MR-1) with a C-terminal TEV protease site and hexahistidine tag was cloned into a pET20 vector. DNA primers for PCR amplification and site-directed mutagenesis were synthesized by Integrated DNA Technologies. Sequencing of all *So* H-NOX variants was carried out by Quintara Biosciences. The gene for untagged *Vc* H-NOX (residues 10-191 of VCA0720 from *Vibrio cholerae* O1 El Tor) and *Tt* H-NOX (residues 1–188 of TtTar4H from *Thermoanaerobacter tengcongensis*) were used as described previously (16).

H-NOX constructs were transformed into the RP523 strain of *Escherichia coli* that had been lysogenized with λDE3 prophage using a kit purchased from Novagen. For heme incorporation, expression cultures were grown at 37 °C in Terrific Broth (RPI Industries) in the presence of 30 μg/mL hemin (diluted from a 200X stock in DMSO) and 200 μg/mL ampicillin. Cells were grown to a density of OD_{600} ~0.6 and then the temperature was dropped to 18 °C. Cells were induced with 1 mM IPTG (final) and allowed to outgrow for 16-18 hours. Incorporation of manganese protoporphyrin IX (MnPPIX) was performed using established protocols (18) with the following addition: 100 μM $MnCl_2$ (final) was added 30 minutes prior to induction to suppress Fe incorporation into demetalated porphyrin.

Vc H-NOX and *Tt* H-NOX were purified as described previously (16). For all *So* H-NOX variants, cell pellets were resuspended in approximately 100 mL of buffer A (50 mM Phosphate (pH 8.0), 300 mM NaCl, 20 mM imidazole, 5 μM β-mercaptoethanol, 5% glycerol, and 1 mM benzamidine hydrochloride), which also contained 1 mM Pefabloc® (Sigma Aldrich) and DNase I. The resuspended cells were lysed three times with an EmulsiFlex-C5 homogenizer (Avestin, Inc.) at 4 °C between 5,000 and 15,000 psi. The lysate underwent centrifugation with an Optima XL-100K ultracentrifuge (Beckman Coulter, Inc.) for 45-60 min at 42,000 rpm (135,000 × *g*). The supernatant was applied at 1.2–1.5 mL⁄min to a nickel affinity column (Qiagen) equilibrated in buffer A. The column was then washed with 10-20 CV of buffer A and eluted using buffer A supplemented with 250 mM imidazole. Eluted protein was then diluted 10-fold with buffer B (50 mM Tris (8.0), 50 mM NaCl, 5 % glycerol, 5 mM DTT, and 1 mM TCEP), mixed with TEV protease, and dialyzed overnight at 4 °C against buffer B. Cleaved protein was then concentrated and subjected to size-exclusion chromatography using a HiLoad 16⁄60 Superdex 75 column (GE Healthcare) that had been equilibrated with buffer C (50 mM Hepes (8.0), 50 mM NaCl, 5 % glycerol, 5 mM DTT, and 2 mM TCEP). The protein was separated with an isocratic flow of buffer C at 1 mL/min while 2 mL fractions were collected. Fractions containing the highest purity *So* H-NOX, as determined by Coomassie staining following SDS-PAGE and Soret: A_{280} ratio from UV-VIS, were pooled and concentrated.

Protein Crystallization. Following gel filtration, all protein manipulation and crystallization was performed in a glove box (Plas Labs) under an argon: hydrogen (95: 5%) environment, at ~25 °C with 40-60% humidity. In addition, all samples containing MnPPIX were handled in either no/low light or under illumination of a red lamp.

Prior to crystallization, heme-bound *So* H-NOX was exchanged into buffer C lacking DTT, fully oxidized (λ_{max} 403 nm) using 1-2 equivalents of potassium ferricyanide, exchanged

into fresh buffer C, and reduced (λ_{max} 430 nm) (Fe^{II}) using 1 mM sodium dithionite (final). Residual dithionite was removed by exchanging the protein into fresh buffer C. Crystallization of ferrous unliganded (Fe^{II}) H-NOX was performed immediately.

Exhaustive crystallization attempts of Wt *So* H-NOX in the Fe^{II} oxidation state were fruitless. Wt *So* H-NOX was then submitted to the Surface Entropy Reduction prediction (SERp) server (19), which identified residues 154QQK, located in the solvent exposed αG-β1 loop, as candidates for mutation. Incorporation of alanine at all three positions (154AAA) yielded multiple crystal hits following sparse-matrix screening. It should be noted that crystallization attempts of 155AA and 154ASA mutants were unsuccessful. Crystals of ferrous-unliganded and Mn^{II}PPIX 154AAA *So* H-NOX for diffraction studies were obtained using sitting drop vapor diffusion by equilibrating a 2 μL drop of 1:1 protein: reservoir against a 700 μL reservoir containing 1.6-1.9 M DL-Malic Acid (pH 7.3). For cryoprotection, 2 μL of mother liquor containing 10 % glycerol was added directly to the drop and crystals were serial transferred into mother liquor solution containing 5, 7.5 and 10 % glycerol prior to flash freezing in liquid nitrogen.

154AAA Mn^{II} *So* H-NOX purified in the Mn^{II} state (λ_{max} 437 nm) and needed no further modification prior to crystallization. Crystallization was performed as described for 154AAA Fe^{II}.

Wt Fe^{II}-NO *So* H-NOX was reduced using the same protocol for 154AAA Fe^{II}. Immediately prior to crystallization, reduced protein (25-30 mg/mL) was mixed with 500 μM (final) of quick-releasing, PROLI-NONOate ($t_{1/2}$ ~5 s at RT), and slow-releasing, DETA-NONOate ($t_{1/2}$ ~ 56 hrs at RT) NO donors (equal mixture) to ensure immediate formation of the NO complex and to maintain adequate NO levels following drop equilibration, respectively. UV-VIS confirmed formation of a 5c-NO complex (λ_{max} 399 nm). Crystals of Wt Fe^{II}-NO H-NOX for diffraction studies were crystallized using sitting drop vapor diffusion by equilibrating a 2 or 4 μL drop of 1:1 protein: reservoir against 700 μL reservoir containing 0.7 M NaH_2PO_4, 0.9 M K_2HPO_4. Cryoprotection was achieved by carefully adding equal drop volume of mother liquor containing 50 % glycerol. Crystals were then transferred into mother liquor containing 30 % glycerol and flash frozen in liquid nitrogen.

NO and CO derivatization. Crystals of Mn^{II}-NO were obtained by transferring cryoprotected Mn^{II} crystals into 10 μL of cryoprotectant in a depression well. Crystals were then covered in 700 μL of silicon oil. Using a gas-tight syringe (Hamilton), 200 μL of anaerobic cryoprotectant containing 2 mM PROLI-NONOate (Cayman Chemical) was added under the layer of oil. Crystals were allowed to incubate for 15-45 minutes prior to freezing in liquid nitrogen.

Fe^{II}-CO crystals were generated using the same protocol for NO derivatization except CO-saturated cryoprotectant was used in place of the NO solution. CO-saturated cryoprotectant was generated by sparging the headspace of a septum-sealed Reacti-Vial (Pierce) containing anaerobic cryoprotectant with CO (99.99 %, Praxair, Inc.) for 5-15 min.

X-Ray data collection and structure refinement. X-ray data were collected using synchrotron radiation at beamlines 8.2.1, 8.2.2 or 8.3.1 at the Advanced Light Source, Lawrence Berkeley National Laboratory. Diffraction images were collected at 100 K at a wavelength of λ = 0.97 or 1.11 Å using 0.5-1.0° oscillations per frame. Data were indexed and integrated using XDS (20) and scaled using Aimless (21) from the CCP4 program suite (22). Phasing of the Fe^{II} data was carried out by molecular replacement with the program Phaser (23) using a Chainsaw (24) prepared model of *Ns* H-NOX (PDB ID: 3TF8) (12) that was further split into 2 subdomains (residues 1-83 and 84-180). The placed model was then subjected to density modification using Parrot (25) followed by extensive manual model building using the program COOT (26). The entire model was rebuilt using a combination of outputs from Buccaneer (27) and ARP/wARP Phasing of the Mn^{II} structure was performed using molecular replacement with the Fe^{II} structure as the search model. The Fe^{II}-CO and Mn^{II}-NO structures were solved by rigid body refinement of the parent structures, Fe^{II} and Mn^{II}, respectively, against the Co- and NO-derivatized X-ray datasets. Phasing of the Fe^{II}-NO structure was achieved using molecular replacement with 2 subdomains (residues 1-83 and 84-180) from the Fe^{II} structure as the search models. Gas ligands were initially placed into overlapping F_o-F_c, $2mF_o$-DF_c, and F_o-F_o densities with an occupancy of 0.5 and temperature factors approximately equal to the average of the four pyrrole nitrogen atoms. Ligand occupancy, position and B factors were refined simultaneously. (28). All structures were refined using Phenix (29) with TLS refinement parameters incorporated. Stereochemical properties were assessed by MOLPROBITY (30). Data collection and refinement statistics are listed in **Table 3.1**.

ICP-AES analysis. All glassware and tubes were rinsed with Chelex®-treated (Sigma Aldrich) MILLI-Q water (Millipore) containing 1% HNO_3 (Sigma Aldrich). Prior to analysis, all proteins were dialyzed against Chelex®-treated buffer (50 mM TEA (7.5), 150 mM NaCl, 1 mM DTT, and 5 % glycerol) for 6- 8 hrs at 4 °C. Protein was diluted with Chelex®-treated buffer to an approximate iron concentration of 300-600 ppb, assuming a 1:1 iron: protein ratio, as determined by UV-VIS and Bradford assay. All protein samples contained 1% HNO_3.

Metal standards were prepared by diluting TraceCert Metal Standard Solution (Fluka) to appropriate concentrations (50-1000 ppb) with Chelex®-treated MILLI-Q water. All standards contained a final concentration of 1% HNO_3. Metal content was analyzed using a Perkin Elmer Optima 7000 DV instrument using the following wavelengths (nm): Co= 228.616, Cu= 324.752, Fe= 238.204, Mg= 280.271, Mn= 257.610, Ni= 221.648, and Zn= 206.200.

Results and Discussion

Structural Features of the Fe^{II}-Unliganded Structure. The H-NOX protein from the facultative anaerobe *Shewanella oneidensis* (SO2144) (*So* H-NOX) was chosen for characterization of the structural changes associated with NO activation in H-NOX proteins because of its high sequence identity (30%) and similar ligand binding properties to sGC – namely, no measurable affinity for O_2 and formation of a stable, five-coordinate complex with NO (λ_{max} 399 nm) that occurs through a transient, six-coordinate intermediate (λ_{max} 420 nm) (**Figure 3.1B,** *top* panel) (6, 7). Importantly, this latter feature differs from the previously reported crystal structure of the non-O_2-binding H-NOX domain from the facultative anaerobe

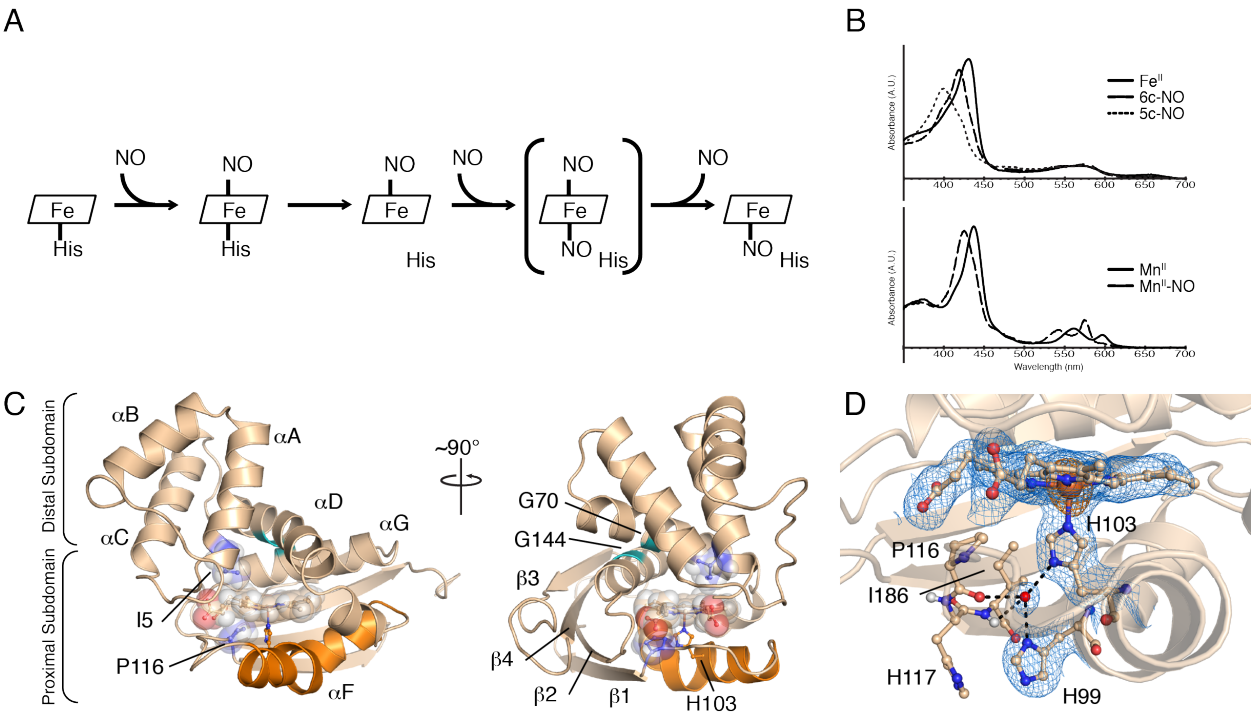

Figure 3.1. NO binding in H-NOX proteins and structural features of Fe^{II}-unliganded *So* H-NOX. (**A**) Reaction scheme of NO binding to H-NOX proteins. The putative dinitrosyl intermediate is shown in brackets. (**B**) UV-VIS absorption spectra for Fe^{II} (top) and Mn^{II} (bottom) nitrosyl complexes. (C) Cartoon representation of the Fe^{II}-unliganded *So* H-NOX structure (molecule A). Secondary structure elements and important structural features are highlighted. The signaling helix, αF, is displayed in orange, residues I5, P116 and the heme are shown as transparent spheres, and conserved glycines G70 and G144 are shown in green. (**D**) Detailed view of the Fe^{II}-unliganded H-NOX heme pocket showing a tightly coordinated water molecule (shown as a red sphere) with residues in the proximal heme pocket. $2mF_o$-DF_c electron density (blue mesh, 1σ) and anomalous difference density (orange mesh, 5σ) are displayed.

Nostoc sp. PCC 7120 (*Ns* H-NOX), which was crystallized as a six-coordinate complex with NO (12).

The Fe^{II}-unliganded structure of *So* H-NOX determined to 2.00 Å resolution (**Table 3.1**), possesses several key features that are conserved among H-NOX proteins. As with other H-NOX proteins crystallized to date, *So* H-NOX contains a heme cofactor that is highly distorted from planarity (RMSD from planarity 0.312 Å). Although the degree and modes of heme distortion (saddling, ruffling, and doming) vary among the reported H-NOX structures, the heme pocket residues that impart distortion – a branched hydrophobic residue in the distal pocket (position 5 in helix αA) and a proline in the proximal pocket – are conserved (11, 12, 15, 17, 31). Consistent with these observations, the Fe^{II}-unliganded structure of *So* H-NOX displays a highly distorted heme due to van der Waals interaction between the conserved proline 116 and pyrrole A (**Figures 3.1C** and **3.1D**). This interaction results in a hinge-like displacement of pyrroles A and D from planarity with the bending axis centered about the heme *β-δ meso* methine positions (**Figures 3.1D** and **3.4B**). Isoleucine 5, located in helix αA within the distal pocket, abuts the heme opposite to proline 116 and thereby serves to communicate the upward displacement of pyrrole D from the heme plane to the distal subdomain (residues 1-83) (**Figure 3.1C**). In

	Fe^{II}			Mn^{II}	
	Native	**NO**	**CO**	**Native**	**NO**
Data Collection					
Wavelength, (Å)	1.00	1.11	1.00	1.00	1.00
Space group	$P6_322$	$P2_12_12$	$P6_322$	$P6_322$	$P6_322$
Cell dimensions					
a, *b*, *c* (Å)	163.9, 163.9, 101.6	67.63, 86.71 33.82	164.2, 164.2, 102.4	163.8, 163.8, 102	164.3, 164.3, 101.7
α, β, γ (°)	90, 90, 120	90	90, 90, 120	90, 90, 120	90, 90, 120
Resolution (Å)	47.5 - 2.20 (2.27 - 2.20)	33.82 1.60 (1.69 - 1.60)	47.58 - 2.25 (2.32 - 2.25)	48.02 – 2.10 (2.16 - 2.10)	47.88 - 2.45 (2.55 - 2.45)
Redundancy	7.2 (7.3)	3.7 (2.1)	11.1 (11.1)	4.8 (2.4)	10.7 (11.0)
Completeness (%)	99.7 (100.0)	99.6 (96.4)	97.4 (98.1)	98.5 (98.6)	100.0 (100.0)
R_{pim} (%)	3.6 (56.9)	3.0 (60.2)	2.8 (44.6)	3.2 (65.5)	3.2 (66.3)
I / σ	17.3 (2.1)	15.9 (1.1)	20.2 (1.8)	12.8 (1.1)	19.3 (1.6)
$CC^{1/2}$	99.9 (56.4)	99.9 (61.3)	99.9 (64.4)	99.9 (74.2)	99.9 (52.7)
Refinement					
R_{work} / R_{free} (%)	17.4 / 19.2	15.9 / 21.6	16.9 / 18.9	19.0 / 22.7	18.7 / 21.9
Ramachandran Favored (%)	97.5	97.8	97.0	97.0	95.1
Ramachandran Outliers (%)	0.0	0.0	0.0	0.2	0.5
Rms deviation					
Bond lengths, (Å)	0.005	0.009	0.014	0.016	0.006
Bond angles, (°)	0.845	1.209	1.304	4.785	0.826
MolProbity Clashscore	3.73	8.79	1.74	3.06	2.54

Values in parentheses correspond to the highest resolution shell.

Table 3.1 X-ray data collection and refinement statistics.

agreement with studies on other H-NOX family members, the orientation of the distal subdomain with respect to the proximal subdomain appears to be linked to the conformation of the heme (13, 14, 17).

In addition, the Fe^{II}-unliganded structure of *So* H-NOX contains a hydrogen-bonding network that intimately links crucial secondary structure elements in the proximal heme pocket. Specifically, the proximal pocket contains an ordered water molecule that hydrogen bonds with the Nδ1 nitrogen of the heme-ligating histidine residue (H103), the Nδ1 of H99, the carbonyl oxygen of P116, and the amide of I118 (**Figure 3.1D**). As a result, this hydrogen-bonding network appears to link the conformation of the P116-containing αF-β1 loop to the conformation of the αF helix. Based on this, it is hypothesized that heme-histidine ligation serves to maintain P116 in van der Waals contact with the heme through hydrogen bonding interactions within the proximal pocket. Notably, due to the coupling of the heme and protein conformations, it is postulated then that this proximal pocket hydrogen-bonding network aids in maintaining the protein in the basal state conformation. Furthermore, a similar mode of water coordination in the proximal pocket also was observed in *Ns* H-NOX (12, 32) and has been hypothesized to be an important feature in H-NOX activation (33).

Analysis of a Structural Zinc Site in *So* H-NOX. Analysis of the electron density in the *So* H-NOX structure following molecular replacement showed a very strong peak in the anomalous difference map centered between residues C139, H161, C164, and C172 (**Figure 3.2A**). As histidine and cysteine residues are commonly observed in zinc or copper coordination sites, it was reasoned that *So* H-NOX possesses a previously unidentified non-heme metal binding site. In order to unambiguously identify the bound metal, purified *So* H-NOX used for

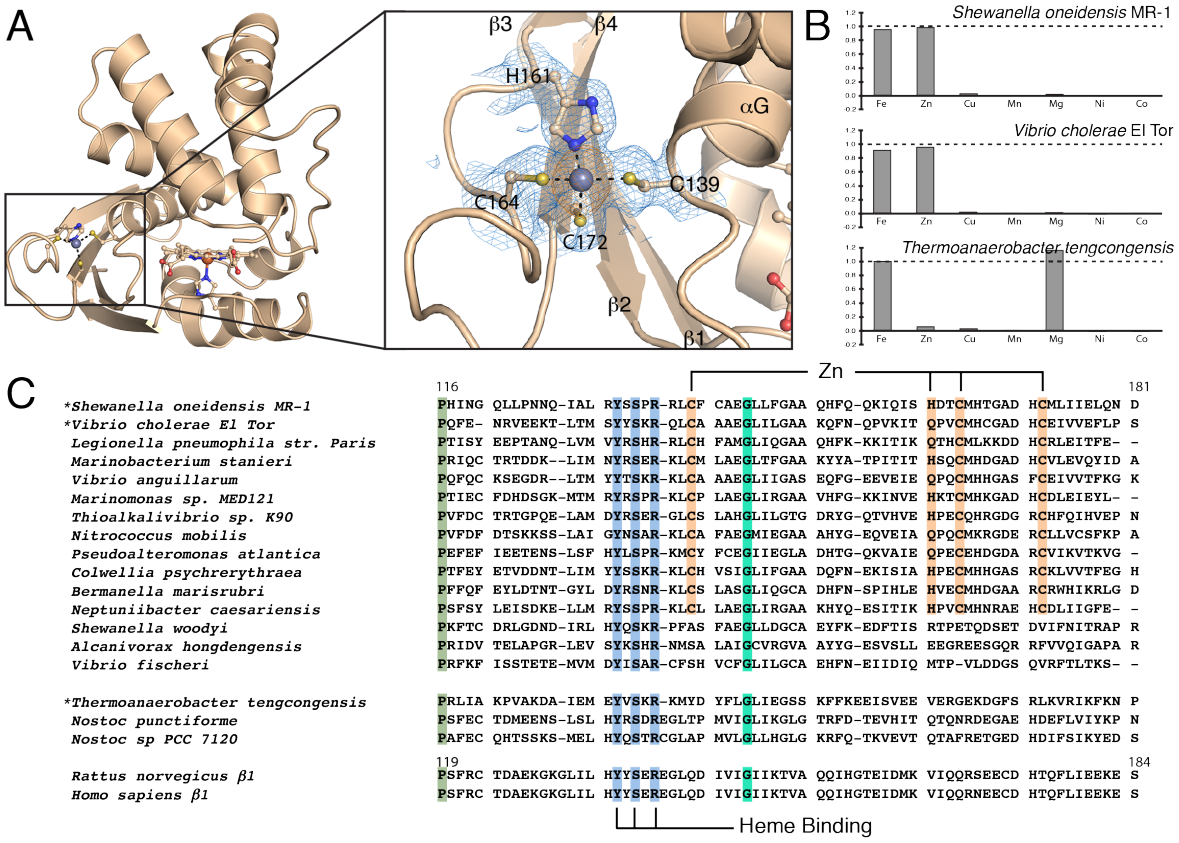

Figure 3.2 Zinc coordination in H-NOX proteins. (**A**) Overall and zoomed-in views of the zinc coordination site in *So* H-NOX. $2mF_o$-DF_c electron density (blue mesh, 1σ) for zinc-binding residues and zinc anomalous difference density (orange mesh, 5σ) are displayed. (**B**) ICP-AES analysis of metal content for various H-NOX proteins. Metal content was normalized to protein concentration and values are averaged between ≥3 measurements. (**C**) Multiple sequence alignment of selected H-NOX proteins from gammaproteobacteria (*top*), firmicutes or cyanobacteria (*middle*), or mammalian sGCs (*bottom*). Sequences were aligned using ClustalW2 (35) to absolutely conserved YxSxR heme-binding motif (highlighted in blue). Zinc coordinating residues are highlighted in orange. Genes marked with an asterisk were subjects of ICP-AES analysis displayed in panel **B**. The conserved proximal pocket proline (P116 *So* H-NOX numbering) is highlighted in green.

crystallization was subjected to inductively coupled plasma absorption emission spectroscopy (ICP-AES). ICP-AES analysis revealed near stoichiometric amounts of iron, originating from the bound heme, and zinc (**Figure 3.2B**). Negligible amounts of copper, manganese, magnesium, nickel or cobalt were detected. Following this analysis, zinc was modeled into the Fe^{II}-unliganded crystal structure and, following refinement, was found to adopt geometric values that correlate well with published statistics for tetrahedral zinc coordination sites (34).

The unprecedented observation of a non-heme metal coordination site in a H-NOX protein garnered curiosity about its prevalence within the H-NOX family. Analysis of a sequence alignment containing all available bacterial H-NOX sequences indicates that the residues involved in zinc coordination are almost exclusively found in gammaproteobacteria. Only a few examples were observed in other classes of bacteria. Furthermore, 78 of 158 known gammaproteobacteria sequences possess putative zinc-binding residues. Of those, 34% contain histidine as the fourth ligand while 66% contain glutamine, both of which are capable of binding

zinc (34). Also included in the sequence alignment analysis are sequences derived from rat and human sGCs, neither of which possess the determined zinc binding residues. As such, the observation of a zinc coordination site is limited predominantly to a select group of H-NOX proteins from gammaproteobacteria (**Figure 3.2C**).

In order to confirm those H-NOX proteins that contain glutamine as the fourth ligand also coordinate zinc, the H-NOX from *Vibrio cholera* (*Vc* H-NOX), which possesses a glutamine in place of H161 (*So* H-NOX numbering) was purified and subjected to ICP-AES analysis. *Tt* H-NOX, not predicted to bind zinc, was also analyzed by ICP-AES. These analyses indicate that *So* and *Vc* H-NOX proteins possess stoichiometric iron and zinc while *Tt* H-NOX, as expected, does not harbor any other metals besides the iron derived from the heme cofactor (**Figure 3.2B**).

Mutational analysis of the zinc site in *So* H-NOX identifies this feature as a crucial component in maintaining the structural integrity of the protein. Specifically, mutation of any one of the zinc-coordinating cysteine residues to serine or H161 to an alanine completely abolished soluble protein expression, presumably, as a result of the inability of the protein to incorporate zinc and fold properly (**Figure B.2C**). However, following the observation that *Vc* H-NOX is capable of binding zinc, H161 in So H-NOX was replaced with a glutamine and purified. ICP-AES analysis determined that H161Q *So* H-NOX bound a stoichiometric amount of zinc and displayed similar stability and ligand binding properties as the wild-type protein (**Figure B.2**). It is then postulated that zinc coordination in H-NOX proteins serves a structural role, a feature common to sites of tetrahedral zinc coordination (34), and links the β3-β4 loop to helix αG within the proximal subdomain of zinc-binding H-NOX proteins.

Mimicking the Transient Six-Coordinate Fe^{II}-NO Intermediate. H-NOX proteins from facultative anaerobes and mammalian sGC initially bind NO as a six-coordinate complex (**Figure 3.1A**). NO binding severally weakens the iron-histidine bond due to the strong *trans effect* of NO, resulting in the rapid formation of the five-coordinate NO-bound species following histidine dissociation (6-9). Though the six-coordinate NO complex is a transient intermediate, structural changes within the heme pocket concomitant with NO binding may aid in histidine dissociation. To elucidate structural changes associated with the formation of a six-coordinate NO complex, a structural analogue was sought due to the short lifetime of this species.

Previous work has shown that sGC reconstituted with manganese (II) protoporphyrin IX (Mn^{II}) remains in a stable, six-coordinate NO-bound state, due to lack of scission of the proximal histidine bond, and thus does not show NO-dependent activation (36). Similar to sGC, binding of NO to unliganded Mn^{II} *So* H-NOX (λ_{max} 437 nm) was found to yield a stable, six-coordinate NO complex (λ_{max} 425 nm) (**Figure 3.1B**, *bottom*). Therefore, it was hypothesized that the structure of Mn^{II}-NO *So* H-NOX could accurately mimic the transient six-coordinate intermediate in the native protein.

Since the crystal structure of Mn^{II}-NO *So* H-NOX would be determined through crystal derivatization of the parent Mn^{II}-substituted *So* H-NOX, the structure of Mn^{II}-unliganded *So* H-NOX first was pursued to establish feasibility. Crystals of Mn^{II}-unliganded *So* H-NOX were obtained under similar conditions as Fe^{II} *So* H-NOX (see methods). The crystals were found to diffract to a comparable resolution (2.10 Å vs. 2.00 Å) in the identical space group with similar

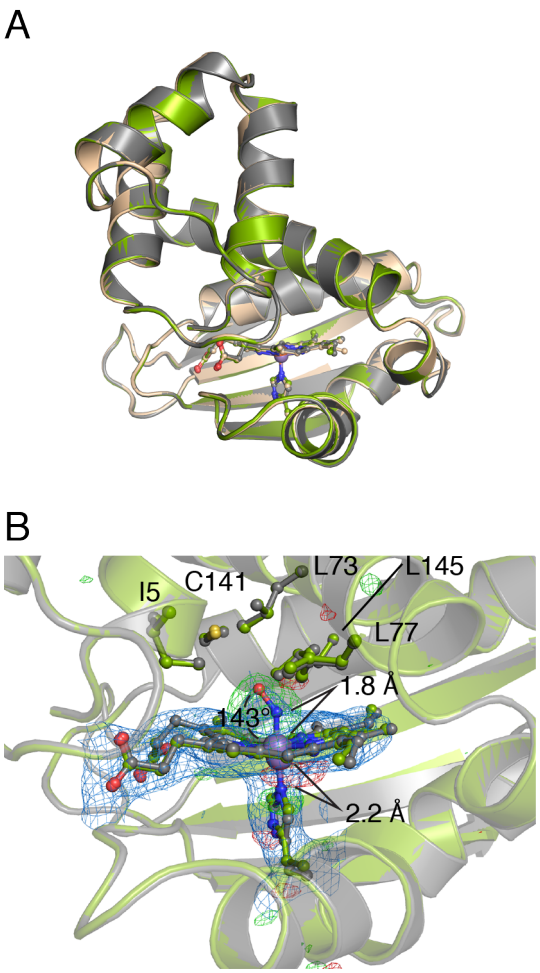

Figure 3.3 Structural comparison of Fe^{II}, Mn^{II} and Mn^{II}-NO *So* H-NOX. (**A**) Overall structural alignment of Fe^{II} (wheat), Mn^{II} (grey) and Mn^{II}-NO (green) *So* H-NOX structures (molecules A). (**B**) Detailed comparison of Mn^{II} and Mn^{II}-NO heme pockets showing the six-coordinate NO complex minimally perturbs residues in the distal pocket. $2mF_o$-DF_c electron density (blue mesh, 1σ) and isomorphous F_o-F_o (NO - native) difference density (positive, green mesh; negative, red mesh, 5σ) are displayed

unit cell parameters (**Table 3.1**). The Fe^{II} and Mn^{II} structures were found to superimpose to a high degree overall with a RMSD of 0.119 Å (C_α–C_α alignment) (**Figure 3.3A**), indicating that replacement of the heme Fe with Mn does not lead to any significant alterations in the protein conformation.

To determine the structure of the six-coordinate Mn^{II}-NO complex, crystals of the Mn^{II}-unliganded protein were soaked with NO (see methods). Analysis of the Mn^{II}-NO - Mn^{II} F_o-F_o isomorphous difference map demonstrated strong positive density distal to H103 in molecule A of the asymmetric unit, indicative of NO binding (**Figure 3.3B**). NO was not present in molecule B (**Figure B.3**). NO was observed to bind in a bent geometry (Mn-N-O angle of 143°), staggered between pyrroles A and D, and was refined to a final occupancy of 91%. The orientation of the NO ligand toward the propionate groups appears to be due to steric restraints imposed by distal pocket residues L73, L77, and L145 (**Figures 3.3B** and **B.4**). Based on comparison to the Mn^{II} structure, NO binding is associated with a slight movement of the Mn^{II} atom within the porphyrin pyrrole nitrogen plane toward the nitrogen atom of the NO ligand (~ 0.5 Å), along with a slight movement of H103 toward the porphyrin (~ 0.4 Å) (**Figure 3.3B).** Movement of H103 maintains a constant Mn-histidine bond length of ~2.2 Å. However, in the six-coordinate ferrous nitrosyl complex, movement of H103 is not expected to occur with movement of the metal within the plane of the porphyrin, thereby leading to an elongated and, presumably, weaker iron-histidine bond (45).

Superimposition of the Mn^{II} and Mn^{II}-NO structures yields a RMSD of 0.120 Å (C_α–C_α alignment), indicating that formation of the six-coordinate NO complex does not induce an appreciable conformational change (**Figure 3.3A**). Furthermore, formation of the six-coordinate NO complex occurs with minimal displacement of distal heme pocket residues (**Figure 3.3B**) as a result of local interactions with surrounding residues. These observations indicate that the primary determinant of iron-histidine bond cleavage appears to be the *trans effect* exhibited by NO. These findings are in agreement with the body of biochemical evidence suggesting that scission of the Fe-histidine bond is a primary contributor to conformational activation of H-NOX proteins, and not simply NO bound to the heme (10, 36).

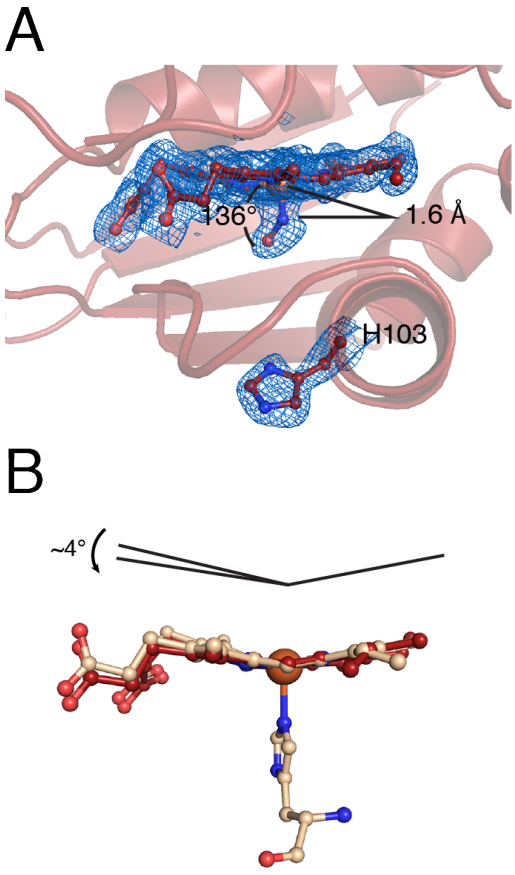

Figure 3.4 Proximal NO and NO-induced heme flattening. (**A**) Zoomed-in view of the Fe^{II}-NO heme pocket show NO binding in a bent geometry to the proximal heme face with the heme-ligating histidine 103 considerably displaced from the heme iron. $2mF_o$-DF_c electron density (1σ) is displayed in blue mesh. (B) Alignment of the Fe^{II} and Fe^{II}-NO hemes (using pyrroles A and B) (molecules A) show an increase in heme planarity upon histidine dissociation.

Nitric Oxide in Excess Binds to the Proximal Face of the Heme. Initial attempts to obtain a five-coordinate NO structure were performed by soaking Fe^{II}-unliganded crystals of *So* H-NOX with various concentrations of NO following the same protocol used to obtain the Mn^{II}-NO structure. However, pronounced crystal cracking, splitting of diffraction spots, and/or significant loss of diffraction was observed even during brief exposure to low concentrations of NO. Thus, it was reasoned that the conformational change associated with formation of the five-coordinate NO complex was not suitable with the lattice constraints induced by crystallographic contacts and efforts should be focused on crystallization of a pre-formed Fe^{II}-NO complex. Briefly, immediately prior to crystallization, the Fe^{II}-unliganded protein was mixed with an excess of quick-releasing, PROLI-NONOate ($t_{1/2}$ ~5 s) and slow-releasing, DETA-NONOate ($t_{1/2}$ ~ 56 hrs) NO donors (equal mixture) to ensure immediate formation of the NO complex and to maintain adequate NO levels following drop equilibration, respectively. Since NO is labile under aerobic conditions, all protein manipulation and crystallization was performed under an argon atmosphere (see methods).

Crystals of pre-formed Fe^{II}-NO *So* H-NOX diffracted to 1.60 Å and were assigned to a different space group than the Fe^{II}-unliganded crystals ($P2_12_12$ vs. $P6_322$), consistent with the hypothesis that the Fe^{II}-crystal lattice constraints were not conducive to the Fe^{II}-NO structure. In agreement with prior spectroscopic studies, the NO ligand in the Fe^{II}-NO structure was found to bind as a five-coordinate adduct (6-8, 37) wherein the heme-ligating histidine is displaced ~8.5 Å from the heme iron following rupture of the iron-histidine bond. Furthermore, NO was found to adopt a bent geometry (Fe-N-O angle of 136°) with the NO oxygen oriented between pyrroles A and B (**Figures 3.4A** and **B.5**).

Notably, NO was observed to bind to the proximal face of the heme (**Figures 3.4A** and **B.5A**). This observation was previously reported for cytochrome c´ from *Alcaligenes xylosoxidans* (Axcyt c´) (38), which, similar to *So* H-NOX and sGC, also reacts with NO to form a five-coordinate complex via a six-coordinate intermediate (39). Previous studies on NO binding in H-NOX proteins have revealed that both the rates of initial NO binding and

subsequent dissociation of the histidine to form the five-coordinate NO complex exhibit NO concentration dependence. Therefore, it was suggested that under conditions where there are at least 2 equivalents of NO per H-NOX protein, a second NO could bind to the proximal face of the heme in place of the dissociated histidine, to form a putative dinitrosyl intermediate, from which the original, distal NO then dissociates to leave a five-coordinate NO complex with the NO residing in the proximal pocket (**Figure 3.1A**) (6-9, 40). Additional support for this hypothesis was obtained from studies using double isotope sequential stopped-flow and freeze quench electron paramagnetic resonance (EPR) experiments where a second NO binding event to the proximal heme face could be discerned (9). The Fe^{II}-NO structure presented here provides crystallographic evidence for the formation of proximal NO in H-NOX proteins. It must be noted, however, that the conditions used to obtain this structure utilized a large excess of NO to maintain a sufficiently adequate concentration of NO during crystallization. Although it is doubtful that a H-NOX signaling system would encounter these concentrations of NO, it would seem that an excess of NO favors binding to the proximal heme face.

It was proposed in Axcyt c´ that steric repulsion imposed by a leucine (L16), located in the distal pocket and directly above the heme iron, decreased the stability of ligands bound in the distal pocket to favor NO binding in the proximal pocket. Support for this hypothesis was grounded in the observation that CO in the CO-bound Axcyt c´ structure was located in the same position previously occupied by L16 and possessed higher thermal parameters than the heme, indicative of a partially occupied or weakly bound CO. Thus, it was reasoned that this steric hindrance destabilized distal-bound ligands, contributing to the transient nature of the six-coordinate nitrosyl complex and favoring binding of NO to the proximal heme face (38, 41).

To obtain further information into whether steric crowding in the distal pocket potentially favors proximal binding of NO in *So* H-NOX, a crystal structure of the Fe^{II}-CO complex was determined to 2.25 Å (**Table 3.1**). Briefly, crystals of Fe^{II} were subjected to the same derivatization protocol used for Mn^{II}-NO except with replacement of the NO solution with CO-saturated cryoprotectant (see methods). Analysis of the Fe^{II}-CO structure reveals that CO binds in a linear geometry (Fe-C-O angle of 178°) at full occupancy to molecule A of the asymmetric unit. No ligand was observed for molecule B. Superimposition of the Fe^{II} and Fe^{II}-CO structures resulted in a RMSD of 0.112 Å (C_α–C_α alignment) (**Figure B.4A**), indicating very modest structural differences. Analysis of the distal pocket reveals that the side chain of L77, located above pyrrole C, moves ~0.6 Å upon CO binding as a result of van der Waals interaction with CO. This results in minor displacement of the CO ligand from linearity with a slight movement of the CO toward pyrrole D and away from L77 (**Figure B.4B**). However, the structural changes are modest and do not result in significant elevation of the B-factors for the CO ligand or an unusual binding geometry. Similarly, the Mn^{II}-NO structure possessed a distal-bound NO without noticeable alterations in the heme pocket. As such, it is reasoned that since *So* H-NOX is able to accommodate ligands in the distal pocket with little structural changes to distal pocket residues or unusual ligand geometries, other factors may contribute to preferential binding of NO to the proximal pocket in H-NOX proteins.

Histidine Dissociation and Structural Changes in the Signaling Helix. Comparison of the Fe^{II}-unliganded and five-coordinate Fe^{II}-nitrosyl structures reveal that the several interconnected structural changes occur within the proximal subdomain following scission of the

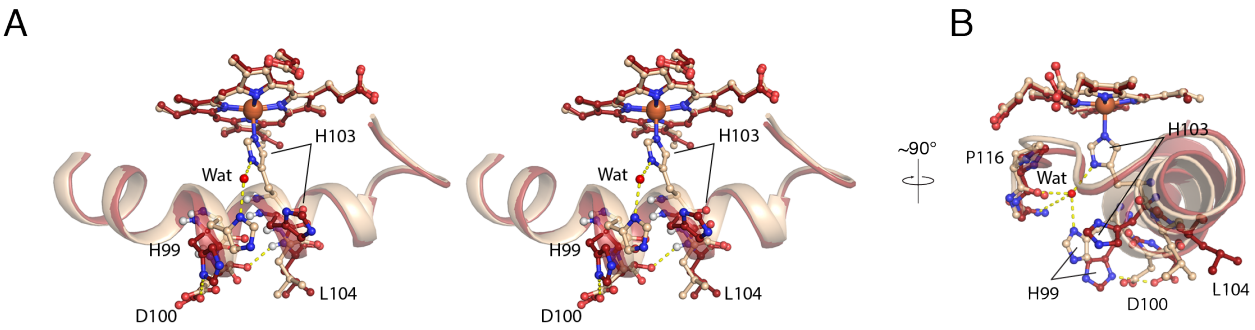

Figure 3.5 Conformational changes within the signaling helix upon NO binding. (**A**) Stereo view of the proximal pocket of Fe^{II} (wheat) and Fe^{II}-NO (red) (molecules A) focusing on important structural changes of the signaling helix (αF) and the αF -β1 loop (residues 91-118). NO has been omitted for clarity. (**B**) 90° rotation of panel A. The proximal pocket coordinated water molecule is shown as a red sphere.

iron-histidine bond. Most notably are pronounced structural changes in the signaling helix αF. These changes, predominantly localized to residues 99-106 and centered about heme-ligating histidine H103, involve a ~45° rigid rotation of these residues about an axis centered along the length of the helix. In the Fe^{II}-unliganded structure, the backbone carbonyl oxygen atoms of residues H99 and D100 lack hydrogen bonding partners, resulting in a pronounced bulge within helix αF. Upon iron-histidine bond cleavage and rotation of the αF helix, the carbonyl oxygen of D100 rotates into hydrogen bonding distance of the amide hydrogen of L104 (4.6 vs. 2.4 Å CO-NH distance) to contribute a new backbone hydrogen bond within helix αF that serves to stabilize the new conformation. Concomitant with rotation of this helix is the displacement of the side chain of H103 by ~8.5 Å (H103 Nε2-Nε2 distance between structures). This is a result of a ~1 Å movement of H103 backbone atoms away from the heme, following rotation of the αF helix, alongside a change in the rotamer of H103 ($\Delta\chi_1$ ~90°) (**Figure 3.4A** and **3.5**). Therefore, it appears that rotation of the αF helix and formation of a new backbone hydrogen bond between residues D100 (CO) and L104 (NH) aids in stabilization of the αF helix with H103 in the "out" conformation.

Histidine dissociation and outward displacement results in loss of the ordered water that was observed between residues H103, H99, P116, and L118 in the Fe^{II}-unliganded structure. Specifically, the side chain of H99 rotates ~180° about χ_1 to reorient Nδ1 from a location capable of interacting with the proximal pocket water to a conformation that now hydrogen bonds with one of the side chain oxygen atoms of D100 (**Figure 3.5**). This new bonding interaction, alongside the additional backbone hydrogen bond, places D100 within a contact network involving a backbone hydrogen bond with L104 and a side chain hydrogen bond with H99. It is hypothesized that this D100-centric contact network contributes significantly to stabilization of the H103 "out" conformation. Additionally, it must also noted that movements of histidines 99 and 103 create a large, solvent accessible void that exposes the proximal face of the heme that may, potentially, serve a role in formation of proximal NO. However, the very rapid binding kinetics associated with the second NO binding may occur faster than movement of proximal pocket residues.

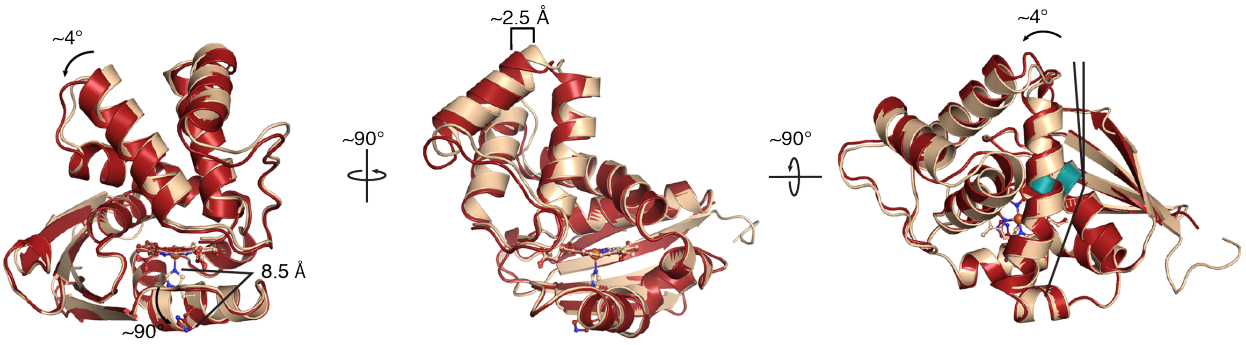

Figure 3.6 Structural comparison of Fe^{II} and Fe^{II}-NO structures. (A) Overlay of Fe^{II} (wheat) and Fe^{II}-NO (red) (molecules A) crystal structures following alignment of the proximal subdomains (residues 95-180) showing displacement of the distal subdomain upon NO-binding and breakage of the iron-histidine bond. Conserved glycines (G70 and G144) (highlighted in green) in helices αD and αG serve as a hinge point for subdomain rotation within *So* H-NOX.

Importantly, the loss of the proximal water molecule eliminates the interactions between helix αF and the αF-β1 loop to favor interactions solely within the αF helix. As such, contacts previously anchoring the αF-β1 loop are released, thereby allowing P116 to translate away from the heme and relieving the heme strain imparted by P116. This allows for subsequent relaxation of the heme toward planarity (0.312 (Fe^{II}) vs. 0.269 (Fe^{II}-NO) Å RMSD from planarity) that is a result of a piano hinge-type bending centered about the heme *β-δ meso* methine positions (aligned using pyrroles B and C) (**Figure 3.4B**). This flattening involves movement of pyrroles A and D by ~4° toward the pyrrole B and C plane. This observation is consistent with the hypothesis that NO-induced scission of the iron-histidine bond results in activation of H-NOX proteins through relaxation of the heme toward planarity.

An important feature in the basal to active conformational switch in *So* H-NOX is loss of the proximal pocket water molecule. This water molecule has also previously been observed in *Ns* H-NOX (12, 32) and is postulated to be a general feature of H-NOX proteins from facultative anaerobes and sGC. Evidence has been provided for this water molecule serving a similar role in sGC wherein mutation of the proposed water-coordinating residue in sGC, D102, to an alanine drastically affected heme stability and activation of the enzyme. As such, it was reasoned that loss of one of the amino acids that stabilize the proximal pocket water molecule destabilized interactions in the heme region to such an extent that the integrity of the enzyme was severely compromised. In sharp contrast to the D102A mutation, replacement of D102 with asparagine resulted in heme binding and formation of a stable five-coordinate NO complex. However, activation by NO was drastically reduced indicating that breakage of the iron-histidine bond and NO activation had been uncoupled (33).

Conformational Changes Associated with Nitric Oxide Binding. Superimposition of molecules A from the Fe^{II} and Fe^{II}-NO structures via their proximal subdomains (residues 95-180) demonstrates that the distal subdomain (residues 1-83) of the Fe^{II}-NO structure undergoes a rigid body displacement of ~2.5 Å that is the result of a ~4° rotation about the heme with a pivot point located within helix αD (**Figure 3.6**). The pronounced kink within helix αD, located at G70, appears to accommodate this rotation by displacing the N-terminus of helix αD by ~4°. This pivot point is of particular interest because the strictly conserved G70 residue makes van

der Waals contact with another conserved glycine, G144, located in helix αG (**Figure 3.1C** and **3.6**). Glycine residues at the interfaces of crossing helices have been observed within polytopic membrane proteins as a means to allow for close helix proximity as well as to provide crossing helices the ability to sample a wider range of crossing angles without disrupting their interface, neither of which would be possible with larger amino acid side chains at helical interfaces (42, 43). Taken together, it is postulated that H-NOX proteins possess glycine residues at these positions, termed the glycine hinge, in order to maintain the αD-αG helical interface while allowing for displacement of the distal subdomain about helix αD during NO-induced activation.

Importantly, the degree by which the distal subdomain rotates about the proximal subdomain (~4°) in formation of the five-coordinate NO structure can be correlated with the degree of pyrrole A and D rotation toward planarity (~4°). Therefore, upon iron-histidine bond cleavage and release of the proximal pocket restraints distorting the heme, residues in the distal pocket that make van der Waals contact with distal face of the heme, primarily I5, move with the trajectory of the heme towards planarity. This results in displacement of the distal subdomain with respect to the proximal subdomain to yield the active H-NOX conformation. This is in agreement with previous structural studies on H-NOX proteins that related the degree of heme distortion to distal subdomain displacement (13, 14, 17).

Rotational displacement of the distal subdomain serves as a probable mechanism for communicating NO binding to the H-NOX protein to associated signaling effector proteins. Conceivably, the effector protein shares an interaction surface with both the distal and proximal H-NOX subdomains in such a manner that following NO binding and distal subdomain rotation, the change in relative subdomain orientation imparts a structural change in the effector protein. In support of this hypothesis, interface mapping in sGC indicate that this interface potentially lies across the distal and subdomains involving αA and αF helices as well as the αB-αC and αF-β1 loops (44).

Conclusion

To provide molecular insight into this activation mechanism, crystal structures of the H-

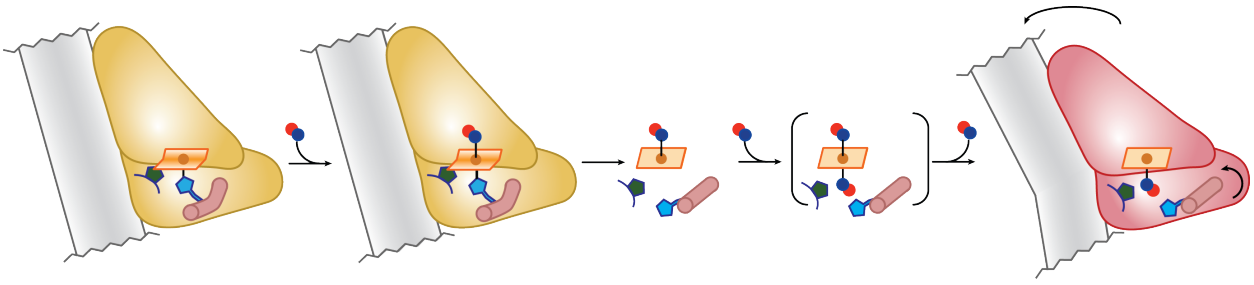

Figure 3.7 Heme-helix strain mechanism for NO-induced activation of H-NOX proteins. In the basal, ferrous unliganded (gold) state the heme (orange square) is distorted from planarity from a coordination network in the proximal involving proline 116 (green pentagon) and the heme-ligating histidine 103 (blue pentagon). Upon binding of NO (blue and red circles) the iron-histidine bond is severed allowing for histidine 103 dissociation and movement of proline 116 away from the heme. This results in a more planar heme, structural changes in the signaling helix (αF) (pink cylinder) to stabilize H103 in the outward conformation, and rotation of the distal subdomain with respect to the proximal subdomain. The resulting active conformation communicates NO binding to the signaling effector domain (shown as a gray rectangle) through contacts bridging the distal and proximal subdomains.

NOX protein from *Shewanella oneidensis* in ferrous-unliganded and both intermediate six-coordinate and active five-coordinate NO-bound states were determined. Analysis of these structures reveal that NO binding and subsequent cleavage of the iron-histidine bond yields the active H-NOX conformation via several, interconnected, structural changes. An integrated "heme-helix strain" model for NO activation has emerged that couples conformational changes within the signaling αF helix to flattening of the heme and rotational displacement of the distal subdomain.

An integral feature of the "heme-helix strain" model proposed here (**Figure 3.7**) is the stored potential energy within the porphyrin macrocycle, analogous to a loaded spring, as a result of its deformation from planarity in the unliganded structure. In the basal state (shown in gold), a proximal pocket hydrogen-bonding network linking the signaling helix to a conserved proline in the αF-β1 loop, places this proline in van der Waals contact with the heme, thereby distorting it from planarity. Following NO binding and scission of the iron-histidine bond, several rearrangements in the signaling helix act to stabilize the heme-ligating histidine in an outward conformation. As such, these rearrangements eliminate the proximal pocket hydrogen-bonding network and release the proline from its restricted position, allowing it to translate away from the heme and subsequently allowing the porphyrin to relax back toward planarity. Residues within the distal pocket contacting the heme opposite to the proline translate heme relaxation to the distal subdomain to drive rotational displacement of the distal subdomain about the proximal subdomain, yielding the active state (shown in red). This conformational change communicates NO binding to the effector protein via a binding interface that, presumably, spans the distal and proximal subdomains. Following NO dissociation back to the unliganded state, the system is reset, effectively "reloading" the spring, and returning the signaling pathway back to the basal state.

References

1. Ignarro LJ, Cirino G, Casini A, & Napoli C (1999) Nitric oxide as a signaling molecule in the vascular system: an overview. *J Cardiovasc Pharmacol* 34:879–886.
2. Bredt DS, & Snyder SH (1992) Nitric oxide, a novel neuronal messenger. *Neuron* 6:3-11.
3. Denninger JW, & Marletta MA (1999) Guanylate cyclase and the ·NO/cGMP signaling pathway. *Biochimica et Biophysica Acta (BBA)* 1411:334-350
4. Russwurm M, & Koesling D (2004) NO activation of guanylyl cyclase. *The EMBO Journal* 23:4443–4450.
5. Derbyshire ER, & Marletta MA (2009) Biochemistry of Soluble Guanylate Cyclase - Springer. *cGMP: Generators*.
6. Stone JR, & Marletta MA (1996) Spectral and kinetic studies on the activation of soluble guanylate cyclase by nitric oxide. *Biochemistry* 35:1093–1099.
7. Zhao Y, Brandish PE, Ballou DP, & Marletta MA (1999) A molecular basis for nitric oxide sensing by soluble guanylate cyclase. *Proc Natl Acad Sci USA* 96:14753–14758.
8. Ballou DP, Zhao Y, Brandish PE, & Marletta MA (2002) Revisiting the kinetics of nitric oxide (NO) binding to soluble guanylate cyclase: the simple NO-binding model is incorrect. *Proc Natl Acad Sci USA* 99:12097.
9. Martin E, Berka V, Sharina I, & Tsai A-L (2012) Mechanism of Binding of NO to Soluble Guanylyl Cyclase: Implication for the Second NO Binding to the Heme Proximal Site.

Biochemistry 51:2737–2746.
10. Derbyshire ER, & Marletta MA (2012) Structure and Regulation of Soluble Guanylate Cyclase. *Annu Rev Biochem* 81:533–559.
11. Pellicena P, Karow DS, Boon EM, Marletta MA, & Kuriyan J (2004) Crystal structure of an oxygen-binding heme domain related to soluble guanylate cyclases. *Proc Natl Acad Sci USA* 101:12854–12859.
12. Ma X, Sayed N, Beuve A, & van den Akker F (2007) NO and CO differentially activate soluble guanylyl cyclase via a heme pivot-bend mechanism. *The EMBO Journal* 26:578–588.
13. Erbil WK, Price MS, Wemmer DE, & Marletta MA (2009) A structural basis for H-NOX signaling in Shewanella oneidensis by trapping a histidine kinase inhibitory conformation. *Proc Natl Acad Sci USA* 106:19753–19760.
14. Olea C Jr., Herzik MA Jr., Kuriyan J, & Marletta MA (2010) Structural insights into the molecular mechanism of H-NOX activation. *Protein Science* 19:881–887.
15. Iyer LM, Anantharaman V, & Aravind L (2003) Ancient conserved domains shared by animal soluble guanylyl cyclases and bacterial signaling proteins. *BMC Genomics* 4:5.
16. Karow DS, Pan D, Tran R, Pellicena P, Presley A, Mathies RA, & Marletta MA (2004) Spectroscopic Characterization of the Soluble Guanylate Cyclase-like Heme Domains from *Vibrio cholerae* and T*hermoanaerobacter tengcongensis*. *Biochemistry* 43:10203–10211.
17. Olea C, Boon EM, Pellicena P, Kuriyan J, & Marletta MA (2008) Probing the Function of Heme Distortion in the H-NOX Family. *ACS Chem Biol* 3:703–710.
18. Winter MB, Woodward JJ, Marletta MA (2013) in *Cytochrome P450 Protocols*, Methods in Molecular Biology, pp 95–106.
19. Goldschmidt L, Cooper DR, Derewenda ZS, & Eisenberg D (2007) Toward rational protein crystallization: A Web server for the design of crystallizable protein variants. *Protein Science* 16:1569–1576.
20. Kabsch W (2010) XDS. *Acta Crystallogr D Biol Crystallogr* 66:125–132.
21. Evans PR, & Murshudov GN (2013) How good are my data and what is the resolution? *Acta Crystallogr D Biol Crystallogr* 69:1204–1214.
22. Winn MD et al. (2011) Overview of the CCP4 suite and current developments. *Acta Crystallogr D Biol Crystallogr* 67:235–242.
23. McCoy AJ (2006) Solving structures of protein complexes by molecular replacement with Phaser. *Acta Cryst (2007) D63, 32-41*.
24. Stein N (2008) CHAINSAW: a program for mutating pdb files used as templates in molecular replacement. *J Appl Crystallogr* 41:641–643.
25. Cowtan K (2010) Recent developments in classical density modification. *Acta Crystallogr D Biol Crystallogr* 66:470–478.
26. Emsley P, & Cowtan K (2004) Coot: model-building tools for molecular graphics. *Acta Crystallogr D Biol Crystallogr* 60:2126–2132.
27. Cowtan K (2012) Completion of autobuilt protein models using a database of protein fragments. *Acta Crystallogr D Biol Crystallogr* 68:328–335.
28. Langer G, Cohen SX, Lamzin VS, & Perrakis A (2008) Automated macromolecular model building for X-ray crystallography using ARP/wARP version 7. *Nat Protoc* 3:1171–1179.
29. Afonine PV et al. (2012) Towards automated crystallographic structure refinement with

phenix.refine. *Acta Crystallogr D Biol Crystallogr* 68:352–367.
30. Chen VB et al. (2009) MolProbity: all-atom structure validation for macromolecular crystallography. *Acta Crystallogr D Biol Crystallogr* 66:12–21.
31. Tran R, Boon EM, Marletta MA, & Mathies RA (2009) Resonance Raman Spectra of an O_2-Binding H-NOX Domain Reveal Heme Relaxation upon Mutation. *Biochemistry* 48:8568–8577.
32. Winter MB, Herzik MA Jr, Kuriyan J, & Marletta MA (2011) Tunnels modulate ligand flux in a heme nitric oxide/oxygen binding (H-NOX) domain. *Proc Natl Acad Sci USA* 108:E881–E889.
33. Baskaran P, Heckler EJ, van den Akker F, & Beuve A (2011) Aspartate 102 in the Heme Domain of Soluble Guanylyl Cyclase Has a Key Role in NO Activation. *Biochemistry* 50:4291–4297.
34. Harding MM, Nowicki MW, & Walkinshaw MD (2010) Metals in protein structures: a review of their principal features. *Crystallography Reviews* 16:247–302.
35. McWilliam H et al. (2013) Analysis Tool Web Services from the EMBL-EBI. *Nucleic acids Research* 41:W598-W600
36. Dierks EA Hu S, Vogel KM, Yu AE, Spiro TG, & Burstyn JN (1997) Demonstration of the Role of Scission of the Proximal Histidine–Iron Bond in the Activation of Soluble Guanylyl Cyclase through Metalloporphyrin Substitution Studies. *J Am Chem Soc* 119:7316–7323.
37. Price MS, Chao LY, & Marletta MA (2007) *Shewanella oneidensis* MR-1 H-NOX Regulation of a Histidine Kinase by Nitric Oxide. *Biochemistry* 46:13677–13683.
38. Lawson DM, Stevenson CEM, Andrew CR, & Eady RR (2000) Unprecedented proximal binding of nitric oxide to heme: implications for guanylate cyclase. *The EMBO Journal* 19:5661–5671.
39. Andrew CR, Green EL, Lawson DM, & Eady RR (2001) Resonance Raman Studies of Cytochrome c´ Support the Binding of NO and CO to Opposite Sides of the Heme: Implications for Ligand Discrimination in Heme-Based Sensors . *Biochemistry* 40:4115–4122.
40. Wu G, Liu W, Berka V, & Tsai A-L (2013) The selectivity of *Vibrio cholerae* H-NOX for gaseous ligands follows the "sliding scale rule" hypothesis. Ligand interactions with both ferrous and ferric Vc H-NOX. *Biochemistry* 52:9432–9446.
41. Lawson DM, Stevenson CEM, Andrew CR, George SJ, & Eady RR (2003) A two-faced molecule offers NO explanation: the proximal binding of nitric oxide to haem. *Biochem Soc Trans* 31:553–557.
42. Russ WP, & Engelman DM (2000) The GxxxG motif: A framework for transmembrane helix-helix association. *Journal of Molecular Biology* 296:911–919.
43. Eilers M, Shekar SC, Shieh T, Smith SO, & Fleming PJ (2000) Internal packing of helical membrane proteins. *Proc Natl Acad Sci USA* 97:5796–5801.
44. Underbakke ES, Iavarone AT, & Marletta MA (2013) Higher-order interactions bridge the nitric oxide receptor and catalytic domains of soluble guanylate cyclase. *Proc Natl Acad Sci USA* 110:6777-6782
45. Dai Z, Farquhar ER, Arora DP, & Boon EM (2012). Is histidine dissociation a critical component of the NO/H-NOX signaling mechanism? Insights from X-ray absorption spectroscopy. Dalton Transactions, 41(26), 7984–7993.

CHAPTER 4

NO Dissociation from Distal and Proximal-Bound, Five-Coordinate Nitrosyl Complexes from the H-NOX Protein from *Shewanella oneidensis*·

Summary

Nitric oxide binds to the heme cofactor of soluble guanylate cyclase (sGC) and a majority of H-NOX proteins to yield a five-coordinate nitrosyl (5cNO) complex. In **Chapter 3**, the first structure of a five-coordinate nitrosyl complex in a H-NOX protein was detailed. Notably, NO was observed to bind to the proximal face of the heme. Although both distal and proximal-bound five-coordinate nitrosyl complexes would yield histidine dissociation, and presumably H-NOX (and sGC) activation, it is hypothesized that these two species proceed through different mechanisms in return to the basal state and, therefore, possess different rates of NO dissociation. In this chapter, rates of NO dissociation are determined for distal and proximal-bound 5cNO species using two different chemically-based NO traps. Unexpectedly, under all conditions tested, similar rate constants for NO dissociation are observed between these two nitrosyl species. As such, it is postulated that the rate-limiting step for dissociation of NO from both 5cNO species is loss of the NO-iron bond.

Introduction

Heme-nitric oxide/oxygen (H-NOX) proteins are a recently discovered family of prokaryotic homologs that possess high sequence identity (18-40%) and exhibit similar ligand binding properties to the heme domain of the mammalian NO receptor, soluble guanylate cyclase (sGC) (1-3). In prokaryotes, these homologues are found in operons adjacent to histidine kinases, diguanylate cyclases or as fusions to methyl-accepting chemotaxis proteins (3). Furthermore, *in vivo* and *in vitro* functional studies have determined that these proteins are involved in NO-mediated signaling pathways (4-7).

The mechanisms by which H-NOX proteins selectively sense and respond to NO has been the focus of much investigation (8-13). Initially thought to be a simple biphasic process, detailed kinetic and structural analyses have revealed this binding reaction to be much more complicated than initially thought (14). NO first binds to H-NOX proteins axial to the heme-ligating histidine to form a six-coordinate nitrosyl complex. The binding of NO severely weakens the iron-histidine bond resulting in loss of the histidine ligand and a distal-bound, five-coordinate NO complex (5cNO) (8, 9, 11, 12). Breakage of the iron-histidine bond has been implicated as the primary determinant for activation of this family of proteins (15-17) (**Chapter 3**). Intriguingly, however, it has been shown that the rate of iron-histidine bond cleavage exhibits NO concentration dependence (8, 9, 11, 12). As such, it has been proposed that when NO is in excess, NO is capable of serving both as a catalyst for iron-histidine bond scission as well as a ligand for the proximal-heme face to yield, ultimately, a proximal-bound, 5cNO species (**Figure**

· The work described in this chapter was done in collaboration with Brian Michel, Ph.D. in Prof. Christopher Chang's laboratory (UC Berkeley). B.M. aided in the synthesis and characterization of *N*-(dithiocarboxy)-sarcosine and corresponding iron chelates.

4.1). Recently, a crystal structure of *So* H-NOX (30% sequence identity to the heme domain of sGC), as a five-coordinate nitrosyl species with NO located to the proximal heme face was obtained. This structure not only detailed the first five-coordinate nitrosyl complex of any H-NOX protein but also provided additional support that excess NO potentially favors NO bound to the proximal heme face (**Chapter 3**).

A major question that arises following the observation that excess NO binds in the proximal pocket is the reversibility of the complex. Since the formation of the proximal-bound 5cNO requires 2 molecules of NO, molecular reversibility does not serve as a feasible option to return the system back to the basal state, following loss of the NO signal, as this would require additional NO. Specifically, an additional NO molecule would be required to bind to the open distal heme face, thereby displacing the proximal-bound NO and freeing the proximal heme face for histidine rebinding and subsequent dissociation of the distal-bound NO (**Figure 4.1**). Thus, first assumptions would dictate that the proximal-bound 5cNO complex would yield a system effectively "stuck" in the NO-bound signaling state. However, if the H-NOX remained as a distal-bound 5cNO complex, it is presumed that histidine rebinding to the proximal heme face would return the system back to the basal state on a much shorter timescale.

The difference in NO dissociation rates between these two nitrosyl complexes is of particular interest considering that *in vivo*, the duration of H-NOX-mediated signaling in response to NO depends, primarily, on the lifetime of the NO-bound H-NOX species. As such, if the proximal-bound 5cNO complex exhibits a markedly slower dissociation rate then the potentiation of the NO signal would be much longer as compared to the distal-bound 5cNO species. To test this hypothesis, the NO dissociation rates from distal and proximal-bound 5cNO species were measured using two alternate, chemical-based NO traps. Most unexpectedly, similar biphasic dissociation rate constants were measured for both NO species. As such, it is concluded that both distal and proximal NO complexes possess the same rate limiting step during NO dissociation and, furthermore, it is hypothesized that this step is loss of the NO-iron bond.

Materials and Methods

Materials. Unless otherwise specified, chemicals were purchased from Sigma Aldrich and used without further modification.

Protein expression and purification. Expression and purification of *So* H-NOX was performed similarly as previously described (**Chapter 3**). A pET20 vector containing full-length *So* H-NOX with a C-terminal TEV protease site and hexahistidine tag was transformed into RP523(DE3) competent cells. A 20 mL overnight culture of TB medium supplemented with 200 μg/mL ampicillin, 100 μM $ZnCl_2$, and 30 μg/mL HEMIN was pelleted and washed prior to inoculation of 2-6 L of similarly prepared TB media (RPI Industries). Cells were grown at 37 °C to a density of OD_{600} ~0.6 before dropping the temperature to 18 °C. Protein expression was induced with 1 mM IPTG (final) and cells were pelleted following a 16-18 hours outgrowth. Cell pellets were resuspended in approximately 100 mL of buffer A (50 mM Phosphate (pH 8.0), 300 mM NaCl, 20 mM imidazole, 5 mM β-mercaptoethanol, 5% glycerol, 1 mM benzamidine hydrochloride), which also contained 1 mM Pefabloc and DNase I. The resuspended cells were lysed using a cell disruptor. The lysate underwent centrifugation with an Optima XL-100K

ultracentrifuge (Beckman Coulter, Inc.) for 45-60 min at 42,000 rpm (135,000 × *g*). The supernatant was applied to a nickel affinity column (Qiagen) equilibrated in buffer A. The column was then washed with 10-20 CV of buffer A and eluted using buffer A supplemented with 250 mM imidazole. Eluted protein was then immediately desalted into buffer B (50 mM Tris (8.0), 50 mM NaCl, 5 % glycerol, 5 mM DTT, and 1 mM TCEP) using a HiPrep 26/10 desalting column. TEV protease was added and incubation was performed at 4 °C for 16-18 hrs under a nitrogen atmosphere. Cleaved protein was then concentrated and subjected to size-exclusion chromatography using a HiLoad 16⁄60 Superdex 75 column (GE Healthcare) that had been equilibrated with buffer C (50 mM TEA (8.0), 50 mM NaCl, 5 % glycerol, 2 mM TCEP). Fractions containing the highest purity *So* H-NOX, as determined by Coomassie staining following SDS-PAGE and Soret: A_{280} ratio from UV-VIS, were concentrated and frozen at -80 °C until use.

Protein preparation. Following gel filtration, all protein manipulation was performed in a glove box (Plas Labs) under an argon: hydrogen (95: 5%) atmosphere, at ~25 °C. *So* H-NOX was exchanged into buffer C and fully oxidized (λ_{max} 403 nm) using 1-2 equivalents of potassium ferricyanide. Protein was then exchanged into fresh buffer C and fully reduced (λ_{max} 430 nm) (Fe^{II}) using 1 mM sodium dithionite (final). Residual dithionite was removed by exchanging the protein into fresh buffer C. Fe^{II} H-NOX was used immediately.

NO dissociation - CO_{sat}/dithionite trap. Protein NO complexes were generated by mixing 5 μM Fe^{II} *So* H-NOX (heme concentration) with diethylamine-NONOate (Cayman Chemical) (in 10 mM NaOH) at a concentration to obtain the desired NO: protein ratio (0.6-0.8 *eq* for substoichiometric and 5 *eq* for excess) (assuming 1.5 mol NO per mol diethylamine-NONOate) in a septum-sealed anaerobic cuvette (Starna Cells). Protein was allowed to react with the NO donor for ~30 minutes to ensure near complete decomposition of NO donor. Conversion to the nitrosyl species was monitored by following the shift in Soret maximum from 430 to 399 nm. The dissociation of NO from the heme of *So* H-NOX was performed using the CO_{sat}/dithionite method described previously (10, 18, 19). The trapping solution was prepared as follows: a solution of 60 mM sodium dithionite ($Na_2S_2O_4$) in buffer D was prepared in a Teflon-sealed Reacti-Vial (Pierce) anaerobically. The solution was removed from the anaerobic chamber and then saturated with CO (99.99 %, Praxair, Inc.) by bubbling the gas through the solution for 10 min prior to immediate use. Cuvette and trap solutions were equilibrated at assay temperature for 5 min prior to initiation. The reaction was initiated by equal addition of the CO_{sat}/dithionite solution to the anaerobic cuvette using an anaerobic buffer-purged Hamilton gas-tight syringe with mixing. The final $Na_2S_2O_4$ concentration in the reaction mixture was 30 mM. Final protein concentrations were 2.5 μM and 1.5-2 μM for excess and substoichometric NO-treated *So* H-NOX, respectively. Final reaction volumes were 500 μL. The reaction was monitored by electronic absorption spectroscopy using a Cary 100 spectrophotometer equipped with a temperature controller (Agilent Technologies) set to varying temperatures (10-20 °C). Data were acquired by scanning periodically over a range of 350-700 nm at 600 nm min^{-1} with a 1 nm interval. A buffer baseline was subtracted from each spectrum and spectra were corrected for baseline drift by normalization in the 690-700 nm range. The dissociation of NO from the heme was monitored as formation of the Fe^{II}-CO complex at 423 nm. Difference spectra were calculated by subtracting the first spectrum (normalized) from each subsequent spectrum (normalized). The values for ΔAbs_{423} extracted from the difference spectra were plotted *versus*

time and fit to a double exponential to obtain rates of NO dissociation. Each experiment was repeated a minimum of 4 times using protein obtained from at least two different purifications. The dissociation rates were confirmed to be independent of dithionite (data not shown).

Synthesis of *N*-(dithiocarboxy)-sarcosine. Synthesis of *N*-(dithiocarboxy)-sarcosine was performed similarly as described previously (20). Sarcosine (Sigma Aldrich, 2.5 g, 28.05 mmol) was added to a solution of NaOH (1.25 g, 31.25 mmol in 20 mL of water) cooled to 10 °C with constant stirring. To this mixture, a solution of carbon disulfide (2.8 mL, 46.5 mmol) dissolved in 7.5 mL absolute ethanol was slowly added while maintaining the temperature as close to 10 °C as possible. Once completed, the reaction was allowed to stir for an additional 30 min followed by chloroform extraction (3 x25 mL). The remaining aqueous solution was rotary evaporated to dryness yielding caramel-like oil. Absolute ethanol was added, mixed to homogeneity, and again rotary evaporated to dryness. This step was repeated until a solid material was obtained. The material was further dried overnight using a high vacuum pump. This entire procedure was repeated with the isolated material in place of sarcosine. NMR analysis was used to monitor reaction completeness and verify final compound was *N*-(dithiocarboxy)-sarcosine (**Figure C.2**). Material was stored at -20 °C in a desiccator to prevent water adsorption.

NO dissociation - dithiocarbamate trap. Protein NO complexes were generated as described for the CO_{sat}/dithionite trap experiments. Due to the hygroscopic nature of *N*-(dithiocarboxy)-sarcosine (DTCS) care should be taken to prevent dissolution with ambient water. The trapping solution was prepared fresh as follows: a solution of 10 mM DTCS, 2 mM Fe^{II} (ferrous sulfate) in buffer D supplemented with 60 mM $Na_2S_2O_4$ was prepared in a Teflon-sealed Reacti-Vial anaerobically. Cuvette and trap solutions were equilibrated at assay temperature for 5 min prior to initiation. The reaction was initiated by equal addition of the ferro-di(*N*-(dithiocarboxy)sarcosine ($Fe(DTCS)_2$) solution to the anaerobic cuvette using an anaerobic buffer-purged Hamilton gas-tight syringe with mixing. Data acquisition was performed as described for the CO_{sat}/dithionite trap. Note, as shown in **Figure C.3**, The chelated iron in $Fe(DTCS)_2$ is prone to oxidation and care must be taken to eliminate oxygen contamination to prevent iron oxidation.

Results and Discussion

Distal and Proximal-Bound NO Complexes. Because both distal and proximal-bound 5cNO complexes are indistinguishable by electronic absorption spectroscopy, the ability to distinguish between these two species in solution has proven remarkably difficult (9, 11, 12, 21-23). The preparation of distal and proximal-bound five-coordinate nitrosyl (5cNO) complexes in H-NOX proteins can be accomplished by using near stoichiometric or excess NO, respectively. It is assumed that under NO limiting conditions, the near diffusion-limited NO association rate would result in each H-NOX molecule only encountering a single NO molecule before NO was exhausted from solution. Presumably, this would yield only 5cNO species with NO bound in the distal heme pocket (**Figure 4.1, *C***) (8, 9, 11, 12). Additionally, it is reasoned that excess NO will favor binding to the proximal pocket. Support for this latter assumption lies in a body of kinetic studies of H-NOX proteins as well as the crystal structure of *So* H-NOX in the five-coordinate, proximal-bound NO state (8, 9, 11, 12) (**Chapter 3**). Indeed, sample preparation for the

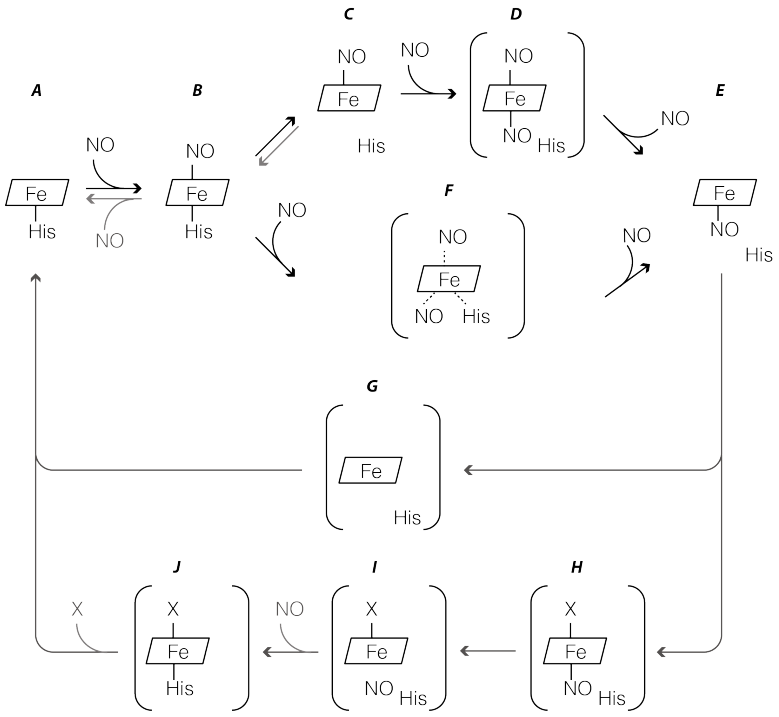

Figure 4.1 Proposed reaction scheme for formation of and dissociation from proximal-bound NO. NO binds initially as a six-coordinate complex (***B***) axial to the heme-ligating histidine. Another NO molecule can then either bind to the open proximal heme face (***C*** to ***D***) following histidine dissociation or as a quaternary complex (***F***). Distal-bound NO then dissociates to yield a five-coordinate, proximal-bound NO species (***E***). Dissociation form the distal-bound, five-coordinate NO complex (***C***) occurs through histidine rebinding (***C*** to ***B***) with subsequent NO dissociation (***B*** to ***A***). Dissociation from the proximal-bound, NO species occurs through either a four-coordinate heme intermediate (***G***) or through a mechanism involving an unknown ligand X that binds to the distal pocket (***H***) that would then allow for histidine rebinding following NO dissociation (***H*** to ***J***).

proximal-bound NO *So* H-NOX structure utilized a large excess of NO in order to maintain adequate NO concentrations during crystallization.

Dissociation of NO from *So* H-NOX – CO_{sat}/Dithionite Trap. In order to obtain insight into the differences in the rate of NO dissociation between distal- and proximal-bound 5cNO complexes, *So* H-NOX was treated with substoichiometric or excess quantities of NO, respectively, and the dissociation of NO was monitored by electronic absorption spectroscopy. In the presence of an NO trap (CO_{sat}/dithionite), dissociation of NO from the heme of *So* H-NOX resulted in an increase in absorbance at 423 nm due to formation of the heme-CO complex. Representative time courses for excess and substoichiometric NO treated *So* H-NOX are shown in **Figure 4.2** (*top* and *middle*, respectively). Comparison of the first spectrum for excess (*top*) and substoichiometric (*middle*) NO-treated samples displays a pronounced increase in heme-CO absorbance in the substoichiometric example. This is a result of CO binding to the unliganded species (~30-40%, **Figure C.1**) in the substoichiometric sample immediately following addition of the CO_{sat}/dithionite trap. Difference spectra (inset) were obtained by subtracting the first spectrum from subsequent spectra. The corresponding plots of ΔAbs_{423} against time, shown in the right panels of **Figure 4.2**, yield a dissociation time course for each sample. For each dissociation time course, the fits to both single and double exponentials are shown (gray and red lines, *right panel*s, respectively). The residuals for each of the fits are shown above each time course. In each case, examination of the fits and residuals of the fits suggested that a two-exponential fit provided a better model for the data despite the fact that there is only a single coordination state as determined by UV-vis. The two rate constants for obtained for each sample (a faster constant k_1 and a slower constant k_2, averaged from at least 4 experiments) and the amplitudes of each corresponding phase (shown as a percent of the calculated total) are reported in **Table 4.1**. The biphasic dissociation of five-coordinate NO from *So* H-NOX is probably a result of two different protein conformations as previously speculated (10, 12, 19, 24, 25).

Protein	NO Treatment	k_1 (s^{-1})	k_2 (s^{-1})	$\Delta A_1 : \Delta A_2$ (%)	Temp (°C)	Trap
S. oneidensis H-NOX	Excess	0.0003 ± 0.00003	0.00007 ± 0.00001	29 : 71 ± 5	10	CO/DT
		0.0008 ± 0.00008	0.00014 ± 0.00001	21 : 79 ± 1	15	CO/DT
		0.0005 ± 0.00007	0.00016 ± 0.00001	35 : 65 ± 4	15	DTC
	Substoichiometric	0.0013 ± 0.00010	0.00028 ± 0.00004	29 : 71 ± 6	20	CO/DT
		0.0011 ± 0.00005	0.00010 ± 0.00001	19 : 81 ± 5	10	CO/DT
		0.0008 ± 0.00009	0.00014 ± 0.00002	25 : 75 ± 2	15	CO/DT
		0.0007 ± 0.00005	0.00018 ± 0.00001	33 : 67 ± 3	15	DTC
		0.0013 ± 0.00006	0.00025 ± 0.00001	32 : 68 ± 2	20	CO/DT
V. cholera H-NOX	Excess	0.01 N.R.	0.001 N.R.	29 : 71 N.R.	24	CO/DT *
	Substoichiometric	0.01 N.R.	0.001 N.R.	16 : 84 N.R.	24	CO/DT *
β1 (1-194)	Excess	0.0030 ± 0.0002	0.00013 ± 0.00001	6 : 94 ± 1	10	CO/DT **
β1 (1-385)	Excess	0.0083 ± 0.0022	0.00018 ± 0.00004	7 : 93 ± 1	10	CO/DT **
sGC	Excess	0.0118 ± 0.0071	0.00012 ± 0.00002	5 : 95 ± 1	10	CO/DT **

Table 4.1 Comparison of NO dissociation rate constants obtained from *So* H-NOX, sGC and other H-NOX proteins. NO dissociation rate constants from *So* H-NOX were measured following treatment with different molar ratios of NO – excess *versus* substoichiometric – using 2 different NO traps. CO/DT corresponds to the CO_{sat}/dithionite NO trap and DTC corresponds to the ferro-di(*N*-(dithiocarboxy)sarcosine NO trap. Values reported for *So* H-NOX were averaged from at least 4 replicates. All values are from this work unless otherwise annotated. β1 (1-194) and β1 (1-385) correspond to truncations of the β1 subunit of soluble guanylate cyclase (sGC).

* Values obtained from ref (12).

** Values obtained from ref (19).

N.R. Values were not reported.

Previous studies to probe the rates of NO dissociation from H-NOX proteins and sGC utilized an excess of NO as a means to ensure a homogenous NO-bound population anticipating that excess, solution NO would subsequently be eliminated immediately upon mixing with trapping solution (10, 19). *So* H-NOX treated in a similar manner (5-10 *eq*. of NO) yielded average rate constants (and amplitudes) of NO dissociation (at 10 °C) of 0.0003 (k_1, 29%) and 0.00007 (k_2, 71%). The k_1 rate constant for *So* H-NOX is ~10-fold slower than that obtained from the H-NOX domain of sGC (β1(1-194) and ~40-fold slower than full-length sGC (**Table 4.1**) (19). However, k_2 is less than 2-fold slower than β1(1-194) and sGC. Moreover, ΔA_2, the fraction of the total amplitude described by k_2, is the dominant species for *So* H-NOX (71%), β1(1-194) (94%) and sGC (95%) and thus it is reasonable to conclude that all three constructs possess similar rates of NO dissociation.

In order to elucidate differences in the lifetimes of distal *versus* proximal-bound NO, NO dissociation rate constants were measured for *So* H-NOX following incubation with a substoichiometric amount of NO. The final percentage of NO-bound H-NOX was estimated to be 60-70% of the total population (~1.5-1.75 μM final concentration following addition of trapping solution) as determined by singular value decomposition analysis (**Figure C.1**). Unexpectedly, the NO dissociation rate constants measured (0.0011 s^{-1} and 0.00010 s^{-1} for k_1 and k_2, respectively) are remarkably similar to those values obtained for proximal-bound NO (both at 10 °C). Specifically, the largest difference observed is a ~4-fold increase in the rate constant k_1 measured from the substoichiometric NO treatment (0.0011 s^{-1} versus 0.0003 s^{-1}) with minor

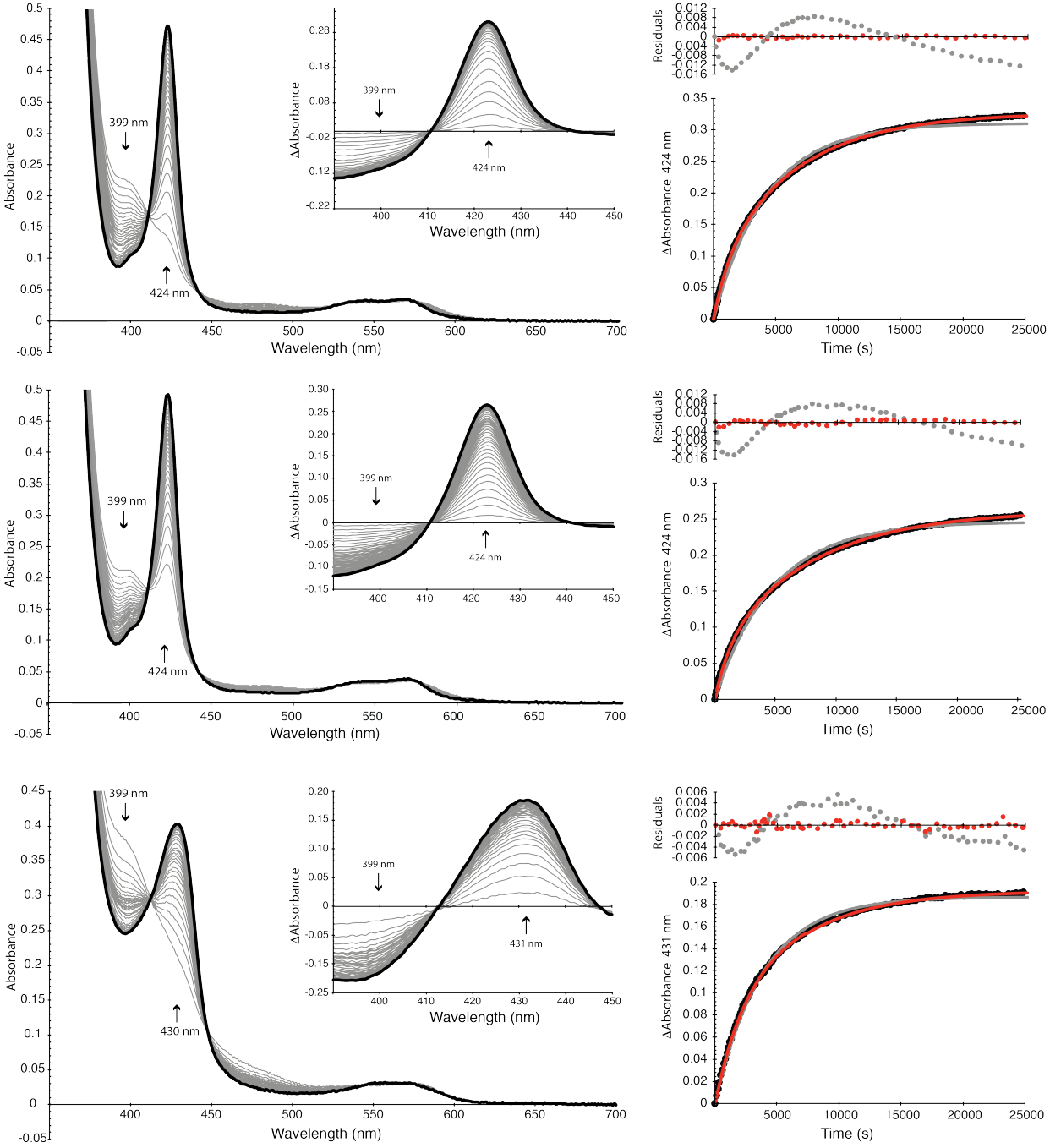

Figure 4.2 Time courses for dissociation of NO from *So* H-NOX at 15 °C determined using CO_{sat}/dithionite (*top* and *middle*) or ferro-di(*N*-(dithiocarboxy)sarcosine (*bottom*) as a trap for NO. NO dissociation was monitored by electronic absorption spectroscopy (left). Data were extracted from the difference spectra (inset) and plotted against the acquisition time course (right). Rates were determined by single (gray line) or double (red line) exponential fits (right) with the corresponding residuals shown above each plot. The time courses shown are representative of dissociation experiments repeated at least 4 times.

differences in k_2, ΔA_1 or ΔA_2 (**Table 4.1**). However, when these same measurements were performed at higher temperatures (15 or 20 °C), the observed rate constants and amplitudes of the two NO species are nearly indistinguishable. For example, at 15 °C, values of 0.0008 s^{-1} (21-

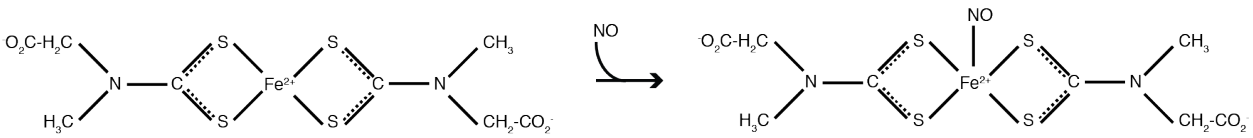

Figure 4.3 Structure and reaction of ferro-di(*N*-(dithiocarboxy)sarcosine with nitric oxide. Two molecules of *N*-(dithiocarboxy)-sarcosine chelate a single iron atom whereby NO binding yields a mononitrosyl ferro-di(*N*-(dithiocarboxy)sarcosine complex.

25%) and 0.00014 s^{-1} (75-79%) were obtained for k_1 (ΔA_1) and k_2 (ΔA_2), respectively, for dissociation of NO from both NO species (**Table 4.1**). The contributing factors that result in the minor differences observed at 10 °C are unknown.

Dissociation of NO from *So* H-NOX – Dithiocarbamate Trap. In the previous experiments, molecular reversibility – binding of an additional NO to the distal heme face to promote dissociation of proximal-bound NO – does not serve as a probable mechanism for dissociation of proximal-bound NO due to the dithionite-dependent destruction of solution NO. However, another ligand could potentially serve a similar role (X in **Figure 4.1**). The observation that distal and proximal-bound 5cNO yielded similar dissociation rates using the CO_{sat}/dithionite trap presented concern that excess CO was potentially serving as ligand X and biasing the observed rates. As such, an alternative trap was pursued that did not utilize a heme ligand.

Dithiocarbamates are a family of bidentate ligands with high affinity for transition metals that have been commonly used as spin traps to detect NO in solution (26), cell culture, or living tissue by electron paramagnetic resonance (EPR) spectroscopy (27-32). These compounds bind iron as diamagnetic Fe^{2+}–dithiocarbamate (1:2) complexes whereby NO binding to the chelated iron yields a paramagnetic mononitrosyl complex that is detectable by EPR (**Figure 4.3**) (29). Amongst the characterized and available dithiocarbamates, ferro-di(*N*-(dithiocarboxy)sarcosine ($Fe^{2+}(DTCS_2)$ was chosen as a potential NO trap due to its relatively high solubility in aqueous solution (> 100 mM) (33) and very high second-order reaction rate constant of NO (~10^8 M^{-1} s^{-1}) (26, 33).

The binding of NO to $Fe^{2+}(DTCS)_2$ does not result in destruction of NO but rather sequestration of solution NO from the protein. As such, dithionite was added to the trapping solution to serve as a means to eliminate any free NO that might arise following dissociation from the $Fe^{2+}(DTCS_2)$ trap. Additionally, dithionite was included to maintain the chelated iron in the ferrous state. Notably, the chelated iron rapidly oxidized to the ferric form in the presence of oxygen, resulting in precipitation of $Fe^{3+}(DTCS)_2$ and subsequently a pronounced increase in bulk scattering across all wavelengths utilized for determining dissociation rates (**Figure C.3**).

In the presence of the Fe^{2+}-$(DTCS)_2$/dithionite trapping solution, dissociation of NO from the heme of *So* H-NOX resulted in an increase in absorbance at 430 nm due to loss of NO and formation of the ferrous-unliganded complex. A representative time course for excess NO treated *So* H-NOX is shown in **Figure 4.2** (*bottom*). Data processing was handled similarly to that described for the CO_{sat}/dithionite experiments except the dissociation time course was extracted from a corresponding plot of ΔAbs_{430} against time as shown in the bottom right panels of **Figure**

4.2. Notably, the dissociation rate constants measured using the Fe^{2+}-$(DTCS)_2$/dithionite trap match those values obtained using the CO_{sat}/dithionite trapping solution, when performed under similar experimental conditions (**Table 4.1**), indicating that the presence of CO in the trapping solution does not bias the observed proximal-NO dissociation rate constants. Additionally, differences in the observed NO dissociation rate constants from distal or proximal-bound NO are negligible, further indicating that these species are indistinguishable, at least when only monitoring dissociation rates.

Dissociation of Proximal-Bound NO. NO dissociation from *So* H-NOX as monitored using either CO_{sat}/dithionite or ferro-di(*N*-(dithiocarboxy)sarcosine/dithionite NO traps displays a single isosbestic point thereby preventing the detection of an intermediate in the NO dissociation pathway. However, following the observation that both NO species are indistinguishable with respect to NO dissociation rate, it hypothesized that the breakage of the NO-iron bond serves as the rate-limiting step for each NO complex. As such, dissociation of NO, be it distal or proximal, would yield a transient four-coordinate protoheme that is rapidly bound by the heme-ligating histidine. In support of this hypothesis, a recent study using cytochrome c´ from *Alcaligenes xylosoxidans* – which has also been shown to form a proximal-bound 5cNO complex – monitored histidine rebinding to heme following photolysis of the NO adduct (21-23, 34, 35). From these data, it was concluded that following photoinduced dissociation of NO from the five-coordinate heme, a percentage, albeit small, of the four-coordinate heme population was rapidly bound by the proximal histidine ligand (τ_{His} = 100 ± 10 ps (k_{His} = 10^{10} s^{-1}). Importantly, if dissociation of the proximal-bound 5cNO species in *So* H-NOX proceeds via rapid-rebinding of the histidine ligand to a four-coordinate heme after loss of NO, then no alternate species besides ferrous-nitrosyl and ferrous-unliganded would be observed when monitoring NO dissociation using ferro-di(*N*-(dithiocarboxy)sarcosine/dithionite NO trapping solution. Indeed, a single isosbestic point during the transition of the proximal-bound 5cNO to the ferrous-unliganded state of the heme was observed (**Figure 4.2**, *bottom*). As such, it is hypothesized that dissociation of five-coordinate, proximal-bound NO from *So* H-NOX proceeds through a very transient four-coordinate heme with rapid rebinding of the proximal histidine ligand (**Figure 4.1**).

Conclusion

In this chapter, two different nitric oxide trapping solutions – CO_{sat}/dithionite and ferro-di(*N*-(dithiocarboxy)sarcosine/dithionite – were used to measure NO dissociation rates from distal and proximal-bound 5cNO complexes in *So* H-NOX. Intriguingly, and contrary to prediction, both traps yielded similar biphasic NO dissociation rate constants from distal and proximal-bound NO species. From these data, it is proposed that both NO species possess the same rate-limiting step during NO dissociation from the heme. It is further hypothesized that this step is loss of the NO-iron bond to form a very transiently lived four-coordinate heme that is rapidly bound by the proximal histidine ligand to yield the basal, ferrous-unliganded heme complex.

References

1. Iyer LM, Anantharaman V, & Aravind L (2003) Ancient conserved domains shared by animal soluble guanylyl cyclases and bacterial signaling proteins. *BMC Genomics* 4:5.

18. 2. Karow DS, Pan D, Tran R, Pellicena P, Presley A, Mathies RA, & Marletta MA (2004) Spectroscopic Characterization of the Soluble Guanylate Cyclase-like Heme Domains from *Vibrio cholerae* and T*hermoanaerobacter tengcongensis*. *Biochemistry* 43:10203–10211.
3. Plate L, & Marletta MA (2013) Nitric oxide-sensing H-NOX proteins govern bacterial communal behavior. *Trends in Biochemical Sciences* 38:566–575.
4. Carlson HK, Vance RE, & Marletta MA (2010) H-NOX regulation of c-di-GMP metabolism and biofilm formation in *Legionella pneumophila*. *Mol Microbiol* 77(4):930-942
5. Wang Y, Dufour YS, Carlson HK, Donohue TJ, Marletta MA, & Ruby EG (2010) H-NOX–mediated nitric oxide sensing modulates symbiotic colonization by *Vibrio fischeri*. *Proc Natl Acad Sci USA* 107:8375.
6. Plate L, & Marletta MA (2013) Phosphorylation-dependent derepression by the response regulator HnoC in the *Shewanella oneidensis* nitric oxide signaling network. *Proc Natl Acad Sci USA*
7. Plate L, & Marletta MA (2012) Nitric Oxide Modulates Bacterial Biofilm Formation through a Multicomponent Cyclic-di-GMP Signaling Network. *Molecular Cell* 46:449–460.
8. Stone JR, & Marletta MA (1996) Spectral and kinetic studies on the activation of soluble guanylate cyclase by nitric oxide. *Biochemistry* 35:1093–1099.
9. Zhao Y, Brandish PE, Ballou DP, & Marletta MA (1999) A molecular basis for nitric oxide sensing by soluble guanylate cyclase. *Proc Natl Acad Sci USA* 96:14753–14758.
10. Boon EM, Davis JH, Tran R, Karow DS, Huang SH, Pan D, Miazgowicz MM, Mathies RA, & Marletta MA (2006) Nitric oxide binding to prokaryotic homologs of the soluble guanylate cyclase β1 H-NOX domain. *J Biol Chem* 281:21892–21902.
11. Martin E, Berka V, Sharina I, & Tsai A-L (2012) Mechanism of Binding of NO to Soluble Guanylyl Cyclase: Implication for the Second NO Binding to the Heme Proximal Site. *Biochemistry* 51:2737–2746.
12. Wu G, Liu W, Berka V, & Tsai A-L (2013) The selectivity of *Vibrio cholerae* H-NOX for gaseous ligands follows the "sliding scale rule" hypothesis. Ligand interactions with both ferrous and ferric *Vc* H-NOX. *Biochemistry* 52:9432–9446.
13. Boon EM, Huang SH, & Marletta MA (2005) A molecular basis for NO selectivity in soluble guanylate cyclase. *Nat Chem Biol* 1:53–59.
14. Cary SPL, Winger JA, Derbyshire ER, & Marletta MA (2006) Nitric oxide signaling: no longer simply on or off. *Trends in Biochemical Sciences* 31:231–239.
15. Dierks EA, Hu S, Vogel KM, Yu AE, Spiro TG, & Burstyn JN (1997) Demonstration of the Role of Scission of the Proximal Histidine–Iron Bond in the Activation of Soluble Guanylyl Cyclase through Metalloporphyrin Substitution Studies. *J Am Chem Soc* 119:7316–7323.
16. Erbil WK, Price MS, Wemmer DE, & Marletta MA (2009) A structural basis for H-NOX signaling in *Shewanella oneidensis* by trapping a histidine kinase inhibitory conformation. *Proc Natl Acad Sci USA* 106:19753–19760.
17. Olea C Jr., Herzik MA Jr., Kuriyan J, & Marletta MA (2010) Structural insights into the molecular mechanism of H-NOX activation. *Protein Science* 19:881–887.
18. Cary SPL, Winger JA, & Marletta MA (2005) Tonic and acute nitric oxide signaling through soluble guanylate cyclase is mediated by nonheme nitric oxide, ATP, and GTP.

Proc Natl Acad Sci USA 102:13064–13069.
19. Winger JA, Derbyshire ER, & Marletta MA (2007) Dissociation of nitric oxide from soluble guanylate cyclase and heme-nitric oxide/oxygen binding domain constructs. *J Biol Chem* 282:897–907.
20. Pou S, Tsai P, Porasuphatana S, Halpern HJ, Chandramouli GV, Barth ED, & Rosen GM (1999) Spin trapping of nitric oxide by ferro-chelates: kinetic and in vivo pharmacokinetic studies. *Biochim Biophys Acta* 1427:216–226.
21. Lawson DM, Stevenson CEM, Andrew CR, & Eady RR (2000) Unprecedented proximal binding of nitric oxide to heme: implications for guanylate cyclase. *The EMBO Journal* 19:5661–5671.
22. Ascenzi P, Santucci R, Coletta M, & Polticelli F (2010) Cytochromes: Reactivity of the "dark side" of the heme. *Biophysical chemistry*.
23. Hough MA, Antonyuk SV, Barbieri S, Rustage N, McKay AL, Servid AE, Eady RR, Andrew CR, & Hasnain SS (2011) Distal-to-Proximal NO Conversion in Hemoproteins: The Role of the Proximal Pocket. *Journal of Molecular Biology* 405:395–409.
24. Derbyshire ER, Gunn A, Ibrahim M, Spiro TG, Britt RD, & Marletta MA (2008) Characterization of two different five-coordinate soluble guanylate cyclase ferrous-nitrosyl complexes. *Biochemistry* 47:3892–3899.
25. Gunn A, Derbyshire ER, Marletta MA, & Britt RD (2012) Conformationally distinct five-coordinate heme-NO complexes of soluble guanylate cyclase elucidated by multifrequency electron paramagnetic resonance (EPR). *Biochemistry* 51:8384–8390.
26. Azizi F, Kielbasa JE, Adeyiga AM, Maree RD, Frazier M, Yakubu M, Shields H, King SB, & Kim-Shapiro DB (2005) Rates of nitric oxide dissociation from hemoglobin. *Free Radical Biology and Medicine* 39:145–151.
27. Vanin AF, Poltorakov AP, & Mikoyan VD (2005) Mechanism of Formation of EPR-Active Mononitrosyl-Iron Complexes with Dithiocarbamates in Biosystems. *Current Topics in Biophysics* 29:139-156
28. Vanin AF, Bevers LM, Mikoyan VD, Poltorakov AP, Kubrina LN, & Faassen EV (2007) Reduction enhances yields of nitric oxide trapping by iron-diethyldithiocarbamate complex in biological systems. *Nitric Oxide* 16:71–81.
29. Vanin AF, Poltorakov AP, Mikoyan VD, Kubrina LN, & van Faassen E (2006) Why iron-dithiocarbamates ensure detection of nitric oxide in cells and tissues. *Nitric Oxide* 15:295–311.
30. Fujii S, Yoshimura T (2000) A new trend in iron–dithiocarbamate complexes: as an endogenous NO trapping agent. *Coordination Chemistry Reviews* 198:89–99.
31. Komarov A, Mattson D, Jones MM, Singh PK, Lai CS (1993) In vivo spin trapping of nitric oxide in mice. *Biochemical and Biophysical Research Communications* 195:1191–1198.
32. Lai CS, & Komarov AM (1994) Spin trapping of nitric oxide produced in vivo in septic-shock mice. *FEBS Letters* 345:120–124.
33. Yoshimura T, & Kotake Y (2004) Spin trapping of nitric oxide with the iron-dithiocarbamate complex: chemistry and biology. *Antioxid Redox Signal* 6:639–647.
34. Lawson DM, Stevenson CEM, Andrew CR, George SJ, & Eady RR (2003) A two-faced molecule offers NO explanation: the proximal binding of nitric oxide to haem. *Biochem Soc Trans* 31:553–557.
35. Yoo B-K, Lamarre I, Martin J-L, Andrew CR, & Negrerie M (2013) Picosecond Binding

of the His Ligand to Four-Coordinate Heme in Cytochrome c′: A One-Way Gate for Releasing Proximal NO. *J Am Chem Soc* 135:3248–3254.

CHAPTER 5

H-NOX Regulation of Signaling Proteins: Studies of the H-NOX: Histidine Kinase Pair From *Shewanella oneidensis*·

Summary

Two-component signaling systems serve as a basic stimulus-response pathway critical for regulation of diverse pathways in bacteria. Recently, it has established that a member of the heme-nitric oxide/oxygen binding (H-NOX) family of hemoproteins from *Shewanella oneidensis* when in complex with nitric oxide (NO) inhibits the activity of a two-component histidine kinase (SO2145). Additionally, *in vivo* studies have shown that this signaling pathway regulates biofilm formation in response to NO. In this chapter, progress into determining how the binding of NO to the H-NOX regulates the autophosphorylation of its cognate histidine kinase is detailed. Using various biophysical techniques, the architecture of a signaling competent H-NOX: histidine kinase complex has been elucidated and, further, it has been determined that the NO-bound H-NOX allosterically inhibits histidine kinase activity via interactions with the N-terminal helical domain of the kinase.

Introduction

Nitric oxide (NO) signaling in animals controls processes such as smooth muscle relaxation and neurotransmission through the NO-cGMP signaling pathway (1-5). Integral to this pathway is soluble guanylate cyclase (sGC), the primary mammalian receptor for NO. sGC is an $\alpha1/\beta1$ heterodimeric protein that catalyzes the cyclization of GTP to cGMP upon the selective binding of NO to the heme cofactor located within the $\beta1$ subunit (4). Recently, a new family of prokaryotic proteins with high sequence identity (15-40%) to the heme domain of sGC has been discovered (6). Biochemical and spectral characterization of several members of this family demonstrated that they exhibit divergent ligand binding properties (7). Specifically, it has been determined that some members of this family, similar to sGC, selectively bind NO even in the presence of O_2, whereas other members are unable to discriminate against NO, CO or O_2 (7-12). As such, members of this family have been termed heme-nitric oxide/oxygen binding (H-NOX) proteins.

Prokaryotic H-NOX proteins are often found in predicted operons with other putative signaling proteins, including histidine kinases (HKs) and diguanylate cyclases (DGCs), or fused to methyl-accepting chemotaxis proteins (MCPs) (6, 13). Importantly, histidine kinases are commonly part of two-component signaling (TCS) pathways – the predominant means by which prokaryotes sense and respond to various extracellular stimuli (14, 15). TCS systems have been observed to regulate bacterial chemotaxis (16, 17), osmoregulation (18), sporulation (19) and

---

· The work described in this chapter was done in collaboration with Rohan Jonnalagadda in Prof. John Kuriyan's laboratory (UC Berkeley), Eric Underbakke, Ph.D. in Prof. Michael A. Marletta's lab (UC Berkeley/The Scripps Research Institute), and Prof. John Kuriyan (UC Berkeley). R.J. aided in obtaining protein for crystallization and collecting X-ray diffraction data. E.U. aided in hydrogen-deuterium exchange by mass spectrometry experimental design as well as data collection and analysis. J.K. aided in data analysis.

cell-differentiation (20, 21). Most TCS systems include a sensor-HK and an effector response regulator (RR) that act in concert to transduce input stimuli to signaling output via, typically, three main steps (22-24). Upon sensing a specific stimulus, the homodimeric HK catalyzes ATP-dependent autophosphorylation of a conserved histidine residue. This phosphoryl group is then transferred to a conserved aspartic acid located within the receiver domain of the RR that, typically, promotes the RR to interact with genes or protein targets to elicit a cellular response (22). Last, signaling is terminated via loss of the RR phosphoryl group by either RR autophosphatase activity or histidine kinase phosphatase activity towards the RR (24).

The observation that H-NOX proteins are associated with two-component histidine kinases suggests that H-NOX/HK pairs may serve as NO receptors. In support of this hypothesis, several *in vitro* and *in vivo* functional studies have confirmed that H-NOX proteins regulate their putative signaling partners in response to NO (25-28). For instance, the facultative anaerobic bacterium *Shewanella oneidensis* contains an H-NOX (SO2144, *So* H-NOX) gene that is co-cistronic with histidine kinase SO2145 (HK2145) and this H-NOX/HK pair operates as a sensor/kinase couple (10, 27, 29). Specifically, it was determined that HK2145 undergoes constitutive ATP-dependent autophosphorylation in the absence of *So* H-NOX or in the presence of the ferrous-unliganded (Fe^{II}) form of *So* H-NOX. Upon binding of NO, *So* H-NOX inhibits the autophosphorylation of HK2145 with an IC_{50} between 5-10 μM (10). Although this provided the first report of H-NOX mediated regulation of a signaling effector protein, the biological output remained unknown until recently.

The penultimate step in TCS signaling involves phosphoryl transfer to the cognate RR domain to elicit a cellular response. RRs typically consist of a highly conserved receiver domain that contains the aspartic acid involved in phosphate transfer and an effector domain that interacts with targets (22, 23)[27]. Although a majority of bacterial H-NOX genes are found adjacent to genes of histidine kinases, nearly 65% of H-NOX/HK pairs (including the H-NOX/HK operon in *S. oneidensis*) lack a cognate response regulator in the same operon and thus the cellular output has remained largely unknown. However, it has recently been determined in *S. oneidensis* that HK2145 possesses three cognate response regulators that are involved in the regulation of intracellular cyclic-di-GMP concentrations (27) and transcriptional feedback regulation of the H-NOX/HK operon (29). As such, this H-NOX-regulated two-component signaling pathway regulates the motility of the host organism to promote biofilm formation upon detection of NO.

Understanding the biochemical functions of H-NOX sensors remains an important immediate challenge. Studies using the H-NOX-mediated TCS pathway in *S. oneidensis* – the most well-characterized bacterial H-NOX signaling pathway to date – have shed some light into the role of H-NOX proteins as regulators of two-component signaling (10, 27, 29). However, the molecular mechanism by which H-NOX sensor domains regulate two-component histidine kinases in response to NO remains largely unknown. Toward this end, this chapter presents recent biophysical data into the architecture of the H-NOX: histidine kinase signaling complex from *S. oneidensis* and details a potential mechanism of H-NOX regulation of histidine kinase autophosphorylation. From these data, it is concluded that the H-NOX: histidine kinase complex forms a 2:2 heterotetramer with an H-NOX protein binding to the N-terminal coiled-coil domain of each histidine kinase protomer. Together, with data presented in **Chapter 3**, it is hypothesized

that the NO-induced conformational change within the H-NOX protein –involving a rotational displacement of the distal subdomain about the proximal subdomain – is transduced through the kinases' N-terminal domain to inhibit proper positioning of the phospho-accepting histidine required for autophosphorylation. Thus, this conformational change would inhibit histidine kinase autophosphorylation and thereby prevent subsequent phosphorylation of the response regulator and downstream signaling.

Methods

Protein expression and purification. Expression and purification of heme-bound and manganese (II) protoporphyrin IX (MnPPIX)-substituted *Shewanella oneidensis* H-NOX (SO2144, *So* H-NOX) were performed as previously described (**Chapter 3**). DNA primers for PCR amplification and site-directed mutagenesis were synthesized by Integrated DNA Technologies. Sequencing of all *So* H-NOX variants was carried out by Quintara Biosciences. The gene for HK2145 (residues 1-311 of SO2145 from *Shewanella oneidensis* MR-1) was cloned into pENTR/TEV/D-TOPO using TOPO cloning (Invitrogen). Gateway cloning (Invitrogen) was used for transfer of genes into the expression plasmid pHMGWA (30) appending a N-terminal His_6-MBP. HK2145 constructs were transformed into *E. coli* Rosetta™ 2(DE3)pLysS competent cells (EMD Millipore). Cells were grown at 37 °C until an OD_{600} ~0.3 and the temperature was dropped to 18 °C. Cells were induced with 100-150 μM IPTG (final) and allowed to outgrow for 18-20 hours. Harvested cell pellets were resuspended in approximately 100 mL of buffer A (50 mM Tris (pH 8.0), 300 mM NaCl, 20 mM imidazole, 10 mM $MgCl_2$, 5 μM β-mercaptoethanol, 5% glycerol, and 1 mM benzamidine hydrochloride), which also contained 1 mM Pefabloc® (Sigma Aldrich) and DNase I. The resuspended cells were lysed three times with an EmulsiFlex-C5 homogenizer (Avestin, Inc.) at 4 °C between 5,000 and 15,000 psi. The lysate underwent centrifugation with an Optima XL-100K ultracentrifuge (Beckman Coulter, Inc.) for 45-60 min at 42,000 rpm (135,000 × *g*). The supernatant was applied at 1.2–1.5 mL min^{-1} to a nickel affinity column (Qiagen) equilibrated in buffer A. The column was then washed with 10 CV of buffer A followed by 10 CV of buffer B (50 mM Tris (8.0), 150 mM NaCl, 25 mM glutamate, 10 mM $MgCl_2$, 10 % glycerol, 5 mM β-mercaptoethanol). Protein was eluted using buffer B supplemented with 250 mM imidazole loaded immediately on an amylose column (New England BioLabs) equilibrated in buffer B. Protein was then washed with 10 CV of buffer B and eluted using buffer B supplemented with 10 mM maltose. Eluted protein was then mixed with TEV protease, and dialyzed overnight at 4 °C against buffer B. Cleaved protein was passed over a nickel affinity column to remove cleaved H_6-MBP, concentrated and subjected to size-exclusion chromatography using a HiLoad 16⁄60 Superdex 200 column (GE Healthcare) that had been equilibrated with buffer C (50 mM Tris (8.0), 150 mM NaCl, 25 mM glutamate, 10 mM $MgCl_2$, 5 % glycerol, 5 mM DTT, and 2 mM TCEP). The protein was separated with an isocratic flow of buffer C at 1 mL min^{-1} while 2 mL fractions were collected. Fractions containing the highest purity HK2145 as determined by Coomassie staining following SDS-PAGE were pooled and concentrated. Glutatione S-transferase (GST) fusions – GST-N-terminal HK (residues 1-60) and GST-C-terminal HK (residues 61-311) – were generated by cloning the desired HK2145 domain(s) into a pGEX-2T vector (GE Healthcare). Proteins were expressed and lysed using the above protocol. Following the pelleting of lysed cell debris, the supernatant was applied at 1.2–1.5 mL min^{-1} to a glutathione agarose column (Pierce) equilibrated in buffer A. The column was then washed with

10 CV of buffer A and eluted with buffer A supplemented with 10 mM reduced glutathione. Eluted protein was concentrated and subjected to size-exclusion chromatography using a HiLoad 16⁄60 Superdex 200 column that had been equilibrated with buffer C. The protein was separated with an isocratic flow of buffer C at 1 mL min^{-1} while 2 mL fractions were collected. Fractions containing the highest purity HK2145 as determined by Coomassie staining following SDS-PAGE were pooled and concentrated.

Analysis of complex formation by analytical gel filtration (AGF). The desired ligation states – ferrous-nitrosyl (Fe^{II}-NO), ferrous-unliganded (Fe^{II}), or ferric (Fe^{III}) – of purified *So* H-NOX were generated as previously described (**Chapter 3**). Complexes of *So* H-NOX (in the desired ligation state) was mixed with a five-fold excess of Wt, full-length HK2145 and incubated for 15-30 minutes at 4 °C. Protein complexes were then analyzed on an analytical Zorbax GF-250 column equilibrated with buffer C and eluted at a flow rate of 1 mL min^{-1}. Protein elution was monitored using absorbance measured at the heme-Soret maximal wavelength for each mixture: 399 nm for Fe^{II}-NO, 427 nm for Fe^{II}, and 403 nm for Fe^{III}.

Pull-down assays. Ferrous-nitrosyl *So* H-NOX-H_6 was immobilized on magnetic Ni^{2+} NTA beads equilibrated in buffer B. Beads were washed with buffer B to remove unbound H-NOX-H_6. GST, GST-N-terminal HK, GST-C-terminal HK, or untagged, full-length HK2145 were incubated with immobilized H-NOX for 1 hour at 4 °C under gentle, frequent mixing. Beads were pelleted using a magnetic tray and beads were washed with buffer B supplemented to 500 mM NaCl. Immobilized proteins were eluted using buffer B supplemented with 250 mM imidazole and analyzed by SDS-PAGE followed by Coomassie staining. Bead-only controls were also analyzed.

Densitometry. Full-length, H72A HK2145 was incubated with 5-fold excess of *So* H-NOX (200 μL final volume) and loaded onto a Superdex 200 10/300 GL equilibrated in buffer C. The complex was separated from free H-NOX using an isocratic flow of buffer C at 1 mL min^{-1} while 0.5 mL fractions were collected. The two peak fractions corresponding to the complex were analyzed by SDS-PAGE followed by Coomassie staining. For each trial, known amounts (1, 2.5, 5 or 10 μg) of each individual component were also analyzed to generate a standard curve. Gel bands were quantified using ImageJ (31).

Hydrogen-deuterium exchange. *Exchange time courses*. Exchange experiments were performed similarly as described previously (32). Exchange time courses were performed in triplicate with the following time points: 1, 2, 5, 10, 30, 60, and 1440 min. Protein samples consisted of 1 nmol of *So* H-NOX-H_6 and 5 nmol of full-length, untagged HK2145 (H72A) (ATP-bound). To initiate exchange, protein samples were diluted with D_2O buffered to 50 mM Tris (pD 8.0), 150 mM NaCl, 10 mM $MgCl_2$, 5 % glycerol, and 1 mM TCEP. At each time point, 150 μL of the reaction was quenched by addition of 2.5% (vol/vol) trifluoroacetic acid (TFA) to a final pH of ~2.5, followed by immediate freezing in liquid nitrogen. For protease digestion, immobilized pepsin (Pierce) was prewashed in deionized H_2O/0.025% TFA/4 M Urea, pH 2.5. Time point samples were thawed quickly and added to 150 μL immobilized pepsin slurry. Digestion proceeded at 4 °C with rotation for 2.5 min. Pepsin was removed by brief centrifugation, and the digested sample was immediately frozen in liquid nitrogen. Samples were maintained at -80 °C until analysis.

MS Analysis. LC-tandem MS for the identification of pepsin digestion products and LC-MS for analysis of peptides following hydrogen/deuterium exchange were performed exactly as described in (32). The mean percent deuteration for each peptide was calculated from at least three replicates with error bars representing standard deviation.

Data analysis. Hydrogen/deuterium exchange MS (HDX-MS) data for *So* H-NOX-H_6 in the presence of excess HK2145 were analyzed using the HX Express macro for Microsoft Excel (33). Deuteron incorporation was measured according to equation S1 described in (32). Back-exchange was estimated to be ~15% from representative maximally deuterated control H-NOX peptides. Maximally deuterated samples were generated by denaturing *So* H-NOX-H_6 in 100% D_2O with 4 M deuterated urea followed by digestion with an equal volume of 50% immobilized pepsin slurry pre-washed in deionized H_2O/0.025% TFA, pH 2.5.

Alanine-scanning mutagenesis. Alanine scanning mutants were generated by site-directed mutagenesis. Constructs were expressed, purified and handled as described for the Wt protein. All mutants displayed similar stabilities and ligand-binding properties as the Wt protein (data not shown). GST or GST-N-terminal HK was immobilized on magnetic glutathione beads. Beads were washed with buffer C to remove unbound GST fusion proteins. Immobilized GST or GST-N-terminal HK were then incubated with the desired *So* H-NOX-H_6 alanine mutant for 1 hour at 4 °C under gentle, frequent mixing. Beads were pelleted using a magnetic tray and beads were washed with buffer C supplemented to 500 mM NaCl. Immobilized proteins were eluted using buffer C supplemented with 10 mM glutathione and analyzed by SDS-PAGE followed by Coomassie staining. Bead-only controls were also analyzed.

Protein crystallization and data collection. Following gel-filtration, full-length HK2145 (H72E) was mixed with a 1.3 molar excess of MnPPIX *So* H-NOX-H_6 and 1 mM AMPPNP. The complex was then concentrated to 20-30 mg/mL and used immediately for crystallization. All samples containing MnPPIX *So* H-NOX-H_6 were handled under low/no light or under illumination of a red lamp. Crystals for diffraction studies were generated using hanging drop vapor diffusion by equilibrating a 2 or 4 μL drop of 1:1 protein: reservoir against 700 μL reservoir containing 2.6-2.8 M NH_4Cl, 0.4 M NaSCN, 0.1 M Tris (7.5), 5% ethylene glycol, 10 mM $MgCl_2$, 5 mM DTT, and 2 mM TCEP. Cryoprotection was achieved by adding 10 μL of mother liquor to the crystal drop followed by re-equilibrating the drop over a fresh reservoir containing: 3.0 M NH_4Cl, 0.4 M NaSCN, 0.1 M Tris (7.5), 30% ethylene glycol, 10 mM $MgCl_2$, 5 mM DTT, and 2 mM TCEP. After 48 hours, crystals were harvested directly from the drop and flash frozen in liquid nitrogen. Data were collected at beamline 8.2.1 or 8.2.2 at the Advanced Light Source, Lawrence Berkeley National Laboratory.

Results and Discussion

H-NOX: Histidine Kinase Complex Formation is Ligation-State Independent. It was shown previously that the H-NOX (SO2144) ligation state exerts different regulatory roles on histidine kinase (SO2145) autophosphorylation activity. Specifically, it was demonstrated that the ferrous-nitrosyl (Fe^{II}-NO) H-NOX inhibits kinase activity while the ferrous-unliganded (Fe^{II}) state displays no inhibitory effects (10). Thus, to determine if NO is required for the H-NOX to form a complex with HK2145, complexes of the histidine kinase with various ligation states of the H-NOX – Fe^{II}, Fe^{III}, and Fe^{II}-NO – were analyzed by analytical gel filtration (AGF). These

data indicate that the H-NOX is capable of forming a stable complex with the histidine kinase regardless of the ligation state (**Figure 5.1**). Taken together with prior studies, this observation indicates that the H-NOX is likely to bound to the histidine kinase while in the Fe^{II} state – allowing for constitutive kinase autophosphorylation – whereby NO binding to the H-NOX results in a conformational change that allosterically inactivates the histidine kinase. This is in contrast to a scenario where the H-NOX inhibits histidine kinase autophosphorylation by simply acting as a molecular wedge that sterically occludes the phospho-accepting histidine (34).

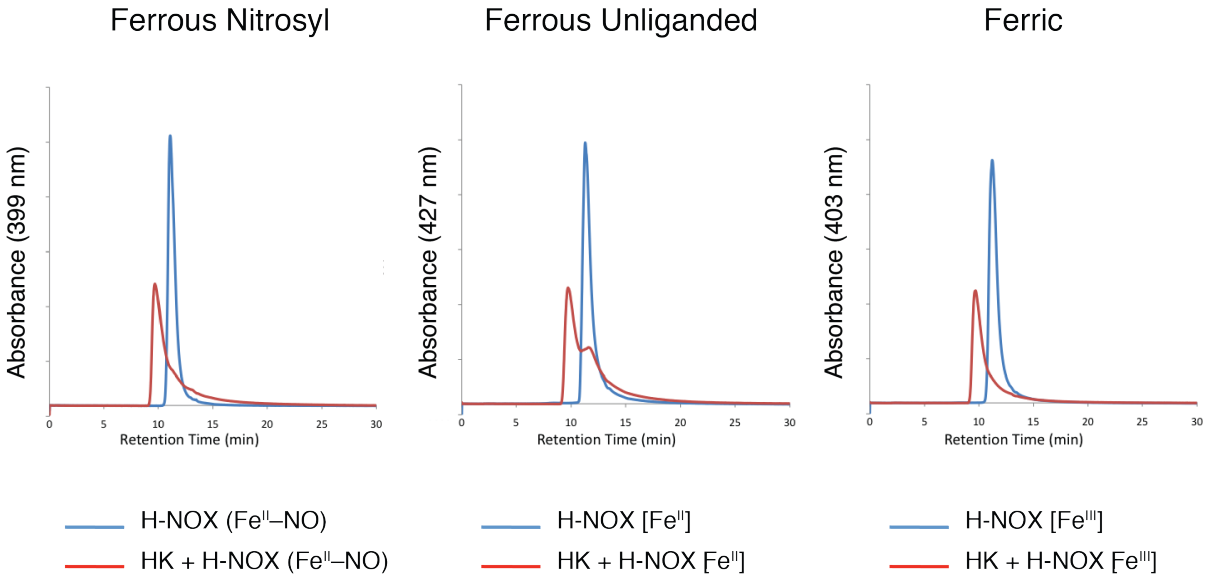

Figure 5.1 Analysis of the H-NOX ligation state dependence for complex formation with histidine kinase SO2145 using analytical gel filtration. For each experiment, elution of the H-NOX and H-NOX: histidine kinase complex were monitored using the maximum absorbance of the H-NOX heme cofactor at the corresponding ligation state (Fe^{II}-NO: 399 nm, Fe^{II}: 427 nm, and Fe^{III}: 403 nm). Complex formation utilized a 5-fold excess of full-length histidine kinase SO2145.

The H-NOX Binds to the N-Terminal Domain of Histidine Kinase SO2145. The observation that Fe^{II} H-NOX forms a stable complex with the kinase without affecting kinase autophosphorylation suggests that the H-NOX may be bound at a region distant from the phospho-accepting histidine. To test this hypothesis, localization of the H-NOX binding interface was determined using pull-down assays with hexahistidine-tagged H-NOX as bait against various histidine kinase domains fused to glutathione S-transferase (GST) (**Figure 5.2**). Briefly, SO2145 is a soluble, homodimeric histidine kinase that contains a N-terminal coiled-coil domain (as estimated by secondary structure prediction servers), a dimerization and histidine phosphorylation (DHp) domain, which houses the phospho-accepting histidine, as well as a C-terminal catalytic and ATP-binding (CA) domain (**Figure 5.2A** and **5.2B**) (35). GST fusions with the N-terminal kinase domain or the kinase core (DHp and CA domains) were generated. NO-bound H-NOX-H_6 was then mixed with GST, the GST fusions, or Wt kinase. Complexes were then immobilized using Ni^{2+} magnetic beads, washed extensively, and the eluates were analyzed by SDS-PAGE (see methods). Analysis of the eluates indicates that the H-NOX shows no appreciable affinity towards GST or the kinase catalytic core. However, GST-N-terminal domain and full-length kinase were obtained in quantities that were nearly stoichiometric with

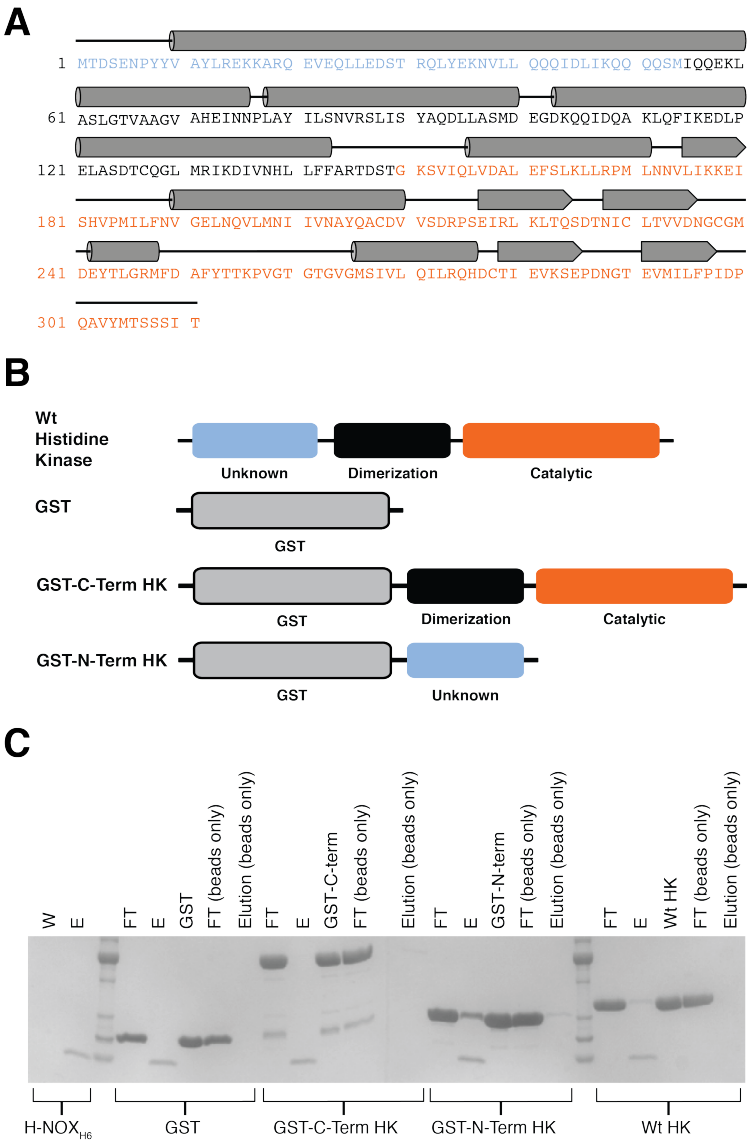

Figure 5.2 (**A**) Secondary structure prediction analysis for histidine kinase SO2145. α-helices are shown as cylinders and β-strands are shown as arrows. The N-terminal domain (light blue), dimerization and histidine phosphorylation domain (black), and the catalytic domain (orange) are colored according to their domain boundaries. (**B**) Domain architecture for histidine kinase constructs used in the H-NOX-H_6 pull-down assay shown in (**C**). (**C**) Pull-down assay using ferrous nitrosyl H-NOX-H_6 as the bait. For each construct the flow-thru (FT), wash (W), elution (E), and bead-only controls were analyzed by SDS-PAGE followed by Coomassie staining.

immobilized H-NOX. As such, from these data, it is clear that the H-NOX binds exclusively to the N-terminal helical domain (**Figure 5.2B** and **5.2C**).

Stoichiometry of the H-NOX: Histidine Kinase Complex. To obtain further insight into the architecture of the H-NOX: histidine kinase complex, the stoichiometry of each component was determined using SDS-PAGE and densitometry (**Figure D.1**). Briefly, histidine kinase was incubated with 5-fold excess H-NOX and then subjected to gel filtration. The two main peaks corresponding to the H-NOX: histidine kinase complex were then analyzed by SDS-PAGE followed by Coomassie staining and gel-based densitometry. For each analysis, known amounts (1, 2.5, 5 or 10 μg) of each individual component were also analyzed to generate a standard curve. Unknown protein amounts were determined against the generated standard curves (see methods).

From these analyses, it is concluded that two H-NOX proteins bind to a histidine kinase homodimer to yield a 2:2 heterotetramer (**Figure D.1**). This observation is somewhat expected considering 1) one would anticipate each kinase protomer to possess a suitable H-NOX binding site, and 2) the genes for the H-NOX (SO2144) and histidine kinase (SO2145) are co-cistronic. From this latter observation it is assumed that initiation of transcription would lead to mRNAs for both components and, thereby, an equal molar ratio of each protein within the cell. Currently, however, it is unclear whether each H-NOX binds to a single histidine kinase protomer or whether the H-NOX: histidine kinase interface spans across both N-terminal helices of the kinase homodimer. Furthermore, it is

unclear whether a single H-NOX protein is capable of exerting NO-dependent inhibition or whether an intact heterotetramer is required.

Mapping the Histidine Kinase Interface on the H-NOX Protein by HDX-MS. Hydrogen-deuterium exchange by mass spectrometry (HDX-MS) was performed in order to map the histidine kinase binding interface on the H-NOX protein. Briefly, NO-bound H-NOX in the presence of a five-fold molar excess of histidine kinase was diluted with >99% D_2O (90% final

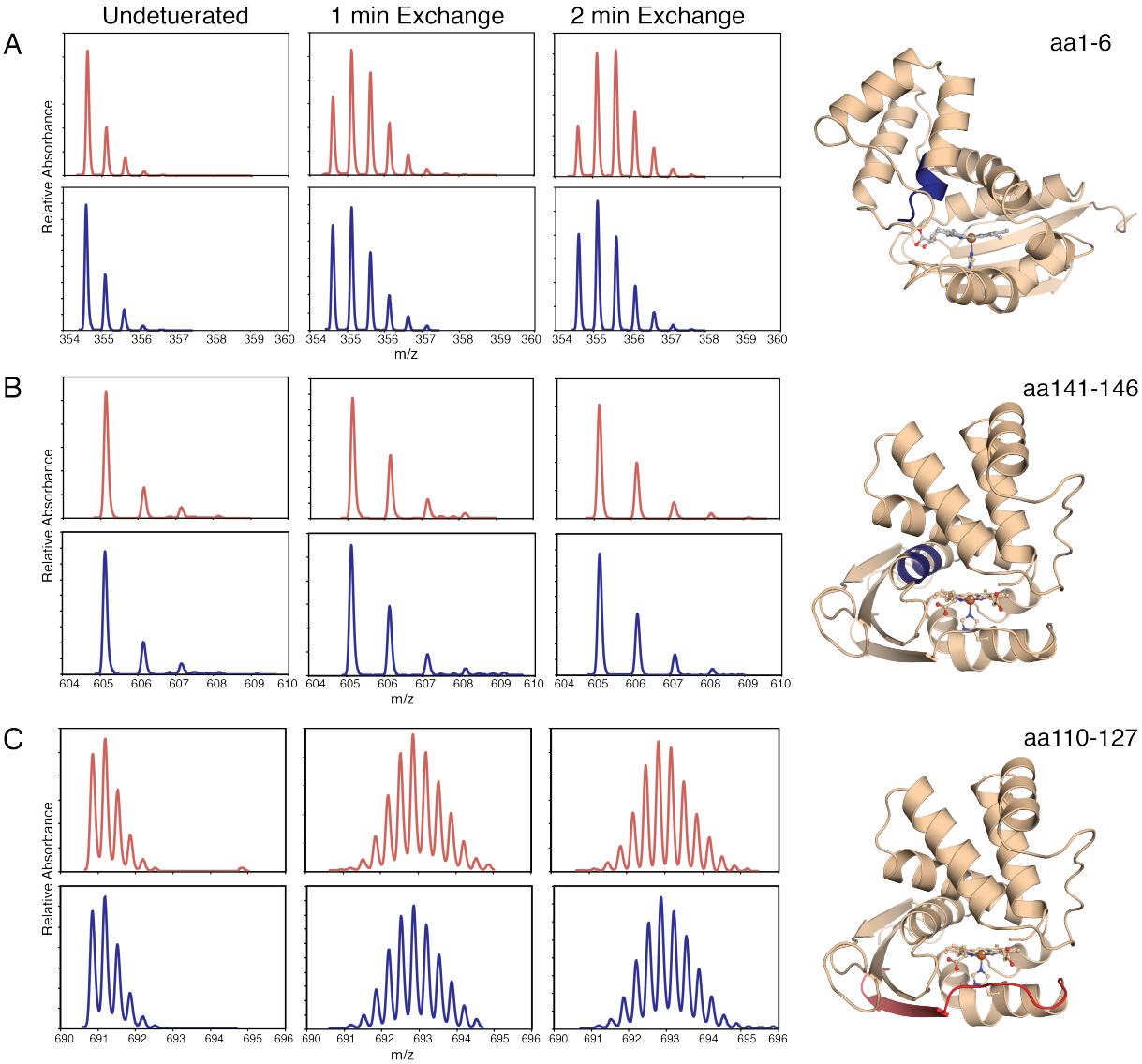

Figure 5.3 Typical exchange time courses for deuteration of *So* H-NOX in the absence (red traces) or presence (blue traces) of histidine kinase (five-fold excess). For each peptide chosen, the mass spectrum is reported following 0 min (undeuterated control), 1 min or 2 min incubation in D_2O. The corresponding amino acids from the exchange time course (colored either blue (slow exchange) or red (fast exchange)) are mapped to the structure of *So* H-NOX (shown in cartoon representation, wheat). (**A**) Amino acids 1-6, locating to the N-terminal helix (shown in blue) exhibits ~30% slower exchange in the presence of the kinase. (**B**) Amino acids 141-146 within the helix αG exhibit very little exchange indicative of a portion of the protein that is very well folded/protected from D_2O. (**C**) The peptide corresponding to amino acids 110-127, which comprise the αF-β1 loop and the β1 strand, exhibits ~50% deuteration from the first timepoint onward indicating that the loop region exchanges very rapidly while the strand portion exchanges slowly.

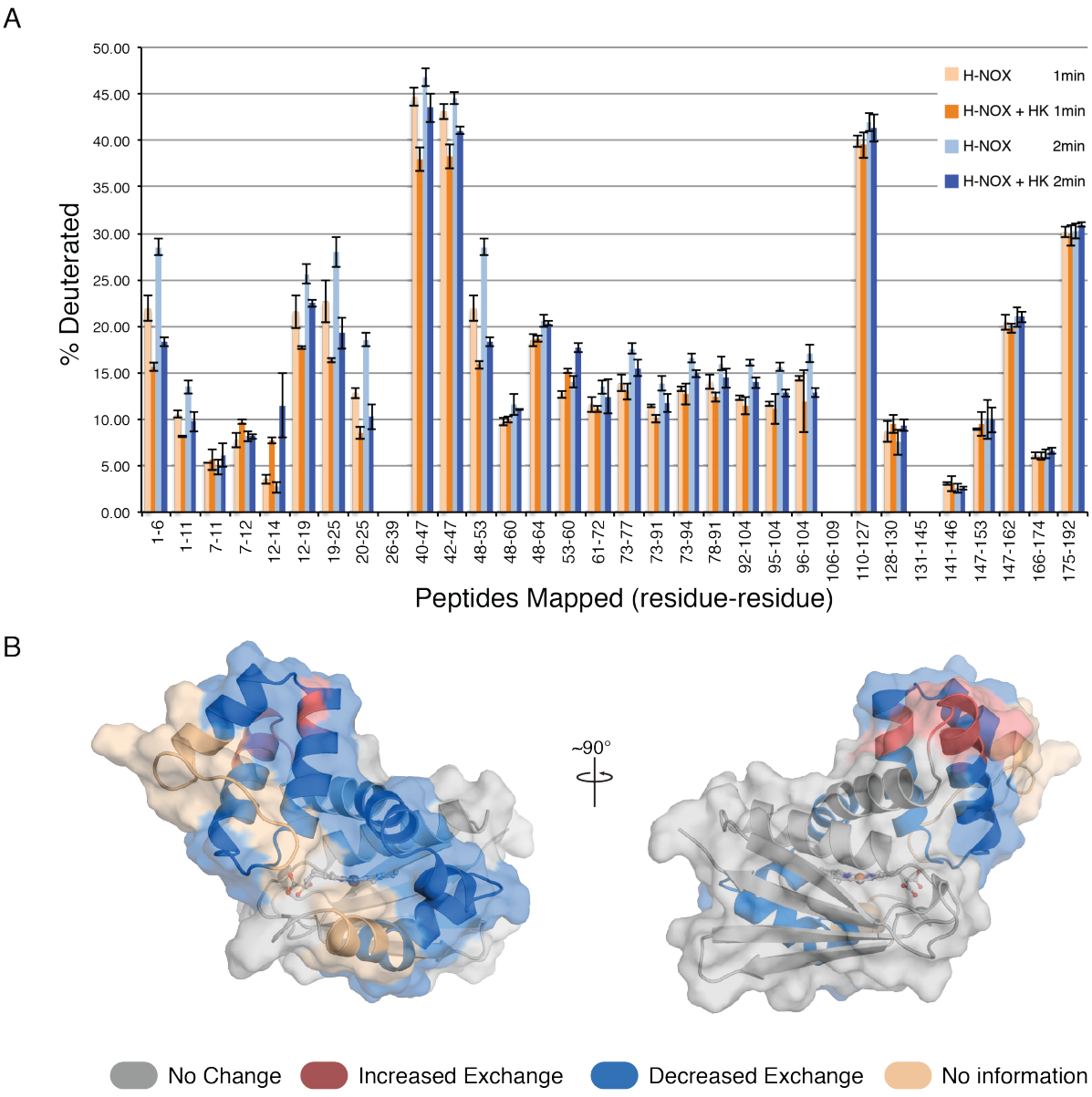

Figure 5.4 (**A**) Percent deuteration of *So* H-NOX in the absence (light orange and orange) or in complex with the cognate histidine kinase SO2145 (5X) (light blue and blue). For each peptide, values are averaged across at least 3 replicates. % Deuteration was determined as the ratio of the number of deuterons incorporated into the peptide versus the number of possible exchangeable amide protons. (**B**) Color coded HDX-MS results mapped to the crystal structure of *So* H-NOX. Peptides that exhibit statistically significant differences in HDX-MS exchange rates are colored accordingly. Regions that do not display differences in exchange rates are colored gray. Regions for which no sequence coverage was obtained are colored wheat.

concentration) to initiate the exchange reaction. After the desired incubation time, reactions were quenched with TFA (final pH of ~2.5) and immediately flash frozen on liquid nitrogen. Samples were then digested with the acid-stable protease pepsin and peptides were then analyzed by liquid chromatography mass spectrometry (LC-MS) (see methods). Optimization of the pepsin digestion step yielded multiple overlapping peptides with 89% and 99% sequence coverage for the H-NOX and histidine kinase, respectively (**Figures D.2** and **D.3**).

Initial analyses of the exchange rates for the free H-NOX are indicative of a well-folded protein (**Figure 5.3** and **5.4A**). Briefly, the peptide corresponding to amino acids 141-146, located within helix αG at the back of the heme pocket, only exhibit ~7-10% exchange over the deuteration time course (**Figure 5.3B** and **5.4A**). This is expected for residues that are not only buried within the core of the protein but also possess amide protons involved in α-helix hydrogen-bonding interactions and thus, not readily exchangeable with solvent. Additionally, the peptide corresponding to residues 110-127 – comprising the αF-β1 loop and β1 strand – rapidly exchanges ~50% of the available amide protons at the first time point (1 min) without appreciable accumulation of additional deuterons over the exchange time course (**Figure 5.3C**). This would indicate that within this peptide, those residues that are located in the αF-β1 loop rapidly exchange their amide protons while those amide protons involved in hydrogen-bonding interactions between the β1 and β2 strands, remain protected during the deuteron exchange time course. Additionally, global analysis of the percent deuteration for H-NOX peptides obtained indicates that different regions exhibit different extents of deuteron incorporation, with flexible loop regions exchanging faster that buried residues (**Figure 5.4A**). If the protein were predominantly unfolded or experienced significant exchange dynamics then the percent deuteration for each peptide would be approximately equivalent.

Regions of the H-NOX that are involved in the H-NOX: histidine kinase interface or experience decreased protein dynamics upon complex formation with the histidine kinase would exhibit decreased rates of deuteron incorporation. Several regions of the H-NOX meet these criteria when in the presence of the histidine kinase (**Figures 5.3A and 5.4**). For example, the peptide corresponding to amino acids 1-6 in helix αA exhibits >30% fewer deuterons incorporated in the presence of the kinase (**Figures 5.3A and 5.4**). Additionally, an overlapping peptide comprised of residues 1-11 also displays decreased exchange in the presence of the kinase indicating that the N-terminal portion of helix αA is potentially involved in binding the histidine kinase. Global analysis of the H-NOX HDX-MS data reveal numerous overlapping peptides that, in the presence of the kinase, display significantly decreased exchanges rates (**Figure 5.4A**). More importantly, these residues map to a single face of the H-NOX, spanning the distal and proximal subdomains. Specifically, residues within helices αA, αB, and the αG-αF loop experience the most significant decrease in exchange rates (**Figure 5.4**). Although, unfortunately, no information was obtained for the αB-αC or αF-β1 loops, it is hypothesized that these loops are also involved in the kinase-binding interface.

Alanine-Scanning Mutagenesis of Histidine Kinase Interface. Alanine-scanning mutagenesis was pursued in order to validate the putative kinase interface obtained by HDX-MS. Briefly, solvent exposed residues observed in regions that experienced kinase-dependent decreased exchange were chosen as targets. Also, solvent-exposed residues in the αB-αC and αF-β1 loops were also chosen as it is hypothesized that these residues are also involved in the interface. Additionally, arginine 131, located in the β2 strand distant from the putative kinase interface, was also chosen as a control mutation. All mutations displayed similar stabilities and ligand-binding properties as the Wt counterpart (data not shown). GST-tagged histidine kinase was then used as bait against each of these mutants to see if any of the mutations abolished binding (see methods). From these data, it appears that the single K108A mutation, located at the first position of the αF-β1 loop, resulted in a pronounced decrease in binding affinity supporting

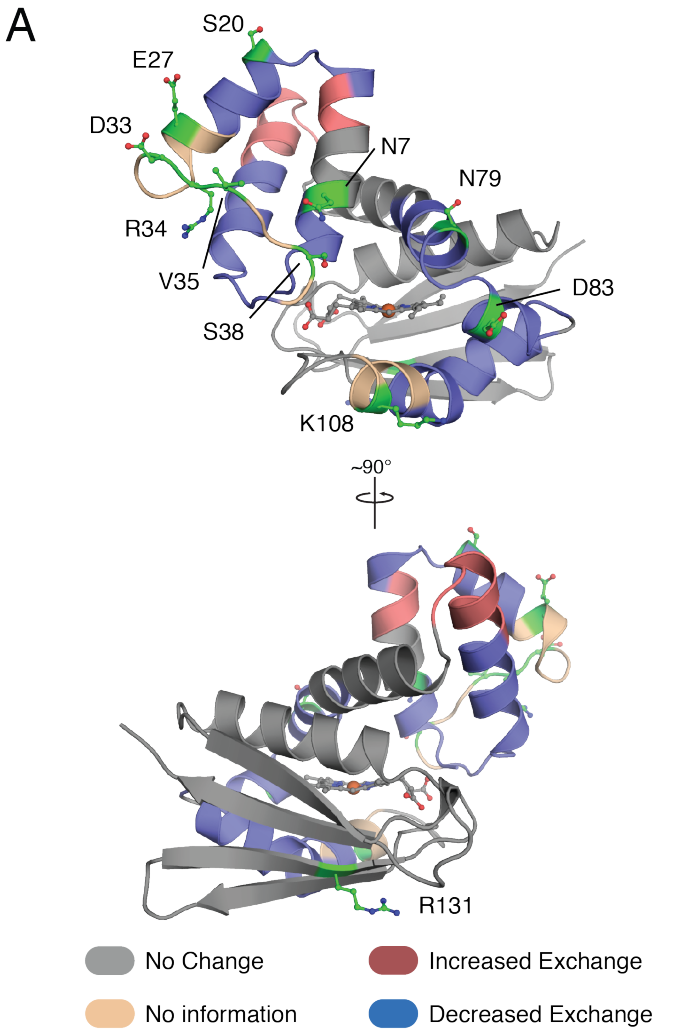

Figure 5.5 (**A**) Structure of *So* H-NOX color coded according to observed changes in deuteration rates in the presence of histidine kinase SO2145 as determined by HDX-MS. Residues chosen for alanine scanning are shown as green sticks. (**B**) The GST-N-terminal domain of the histidine kinase was used as bait against Wt *So* H-NOX-H6. GST of the GST-fusion were incubated with the corresponding H-NOX mutants and then pulled out of solution using magnetic glutathione beads. After the beads were washed extensively the bead eluate was analyzed by SDS-PAGE. Lane 1 is the GST only control. Lane 2 utilized immobilized H-NOX-H_6 to pull-down GST-N-terminal HK.

the involvement of this putative interface in kinase recognition (**Figure 5.5**). However, a majority of the mutations did not yield significantly decreased H-NOX binding. It is possible that the conditions utilized in the assay (protein concentrations, etc.) are not capable of elucidating the modest differences in binding affinity. Additionally, it is also possible that, considering how expansive the putative interface is, a single mutation will not completely abolish binding but multiple mutations in conjunction are required. As such, current efforts include varying protein concentrations, using the K108A mutation in the background of the other alanine mutants, as well as incorporating more disruptive mutations (i.e. valine to glutamate, etc.).

Allosteric Regulation of Histidine Kinase Autophosphorylation. Previous structural studies have determined that histidine kinase DHp domains homodimerize to yield a four-helix bundle with the phospho-accepting histidine located on the surface of helix 1 of each protomer (35-41). A short, flexible linker that connects the C-terminus of helix 2 of the DHp domain to the CA domain allows the CA domain to sample multiple orientations required for autophosphorylation. Additionally, recent structural studies indicate that transmembrane histidine kinases communicate binding of specific extracellular signals to the cytoplasmic kinase domain via rotation of the transmembrane α-helices that subsequently alter the DHp domain dimer interface (42, 43). This conformational change within the DHp domain can either place the phospho-accepting histidine in a conformation that is readily accessible for phosphorylation

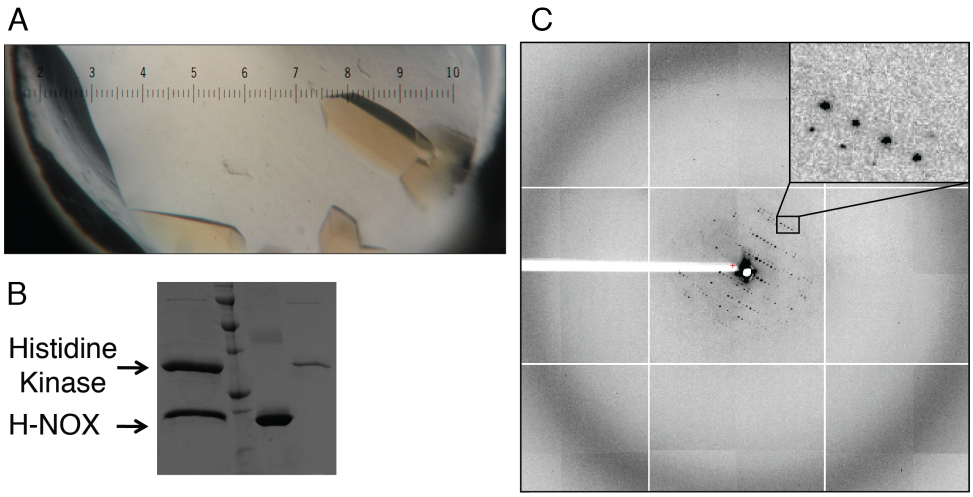

Figure 5.6 (**A**) Crystals of Mn^{II}PPIX H-NOX:full length, AMPPNP-bound H72E HK2145 obtained via hanging drop vapor diffusion at 4 °C (see methods). Tick marks correspond to approximately 50 microns. (**B**) SDS-PAGE analysis of crystals of the H-NOX:histidine kinase complex (lane 1) and purified H-NOX and histidine kinase (lanes 3 and 4, respectively) used in complex formation. Complex crystals were washed extensively with mother liquor prior to mixing with SDS loading buffer. (**C**) X-ray diffraction image of H-NOX: histidine kinase crystals. Crystals diffract to ~8 Å belonging to a hexagonal space group with approximate unit cell dimensions of 205x205x235 Å.

or occlude it from the CA domain to prevent phosphorylation (16, 40, 44).

Although histidine kinase SO2145 lacks a sensor domain, it is hypothesized that the same mechanism of helix rotation is utilized for communication between the H-NOX sensor domain and the DHp domain. Mapping of the histidine kinase binding interface using HDX-MS and alanine scanning mutagenesis revealed that this interface spans across the distal and proximal subdomains of the H-NOX, involving helices αA, αB, and the αB-αC and αF-β1 loops. The N-terminal domain of SO2145 – predicted to be a long α-helix that extends from the N-terminus of helix 1 of the DHp domain – binds at this interface, lying across the distal and proximal H-NOX subdomains. As such, any changes in the relative orientation of the H-NOX subdomains would result in changes in the kinase N-terminal domain. Along these lines, the NO-induced conformational changes in the H-NOX protein detailed in **Chapter 3** – a pronounced rotational displacement of the H-NOX distal subdomain about the proximal subdomain – would induce a kink and/or rotation of the kinase N-terminal helices that, presumably, would elicit a rotation of the helices within the DHp domain and alter the orientation of the phospho-accepting histidine. Taken together, it is hypothesized that these NO-induced series of conformational changes would inhibit histidine kinase autophosphorylation by placing the phospho-accepting histidine in a position inaccessible by the CA domain.

Crystallization of the H-NOX: Histidine Kinase Complex. In order to further obtain molecular details into the H-NOX: histidine kinase interaction as well as insight into the mechanism by which the H-NOX allosterically regulates the kinase, a crystal structure of the H-NOX: histidine kinase complex was pursued. Towards this end, exhaustive crystallization attempts utilizing a combinatorial library of H-NOX constructs and ligation states (Fe^{II}, Fe^{II}-NO,

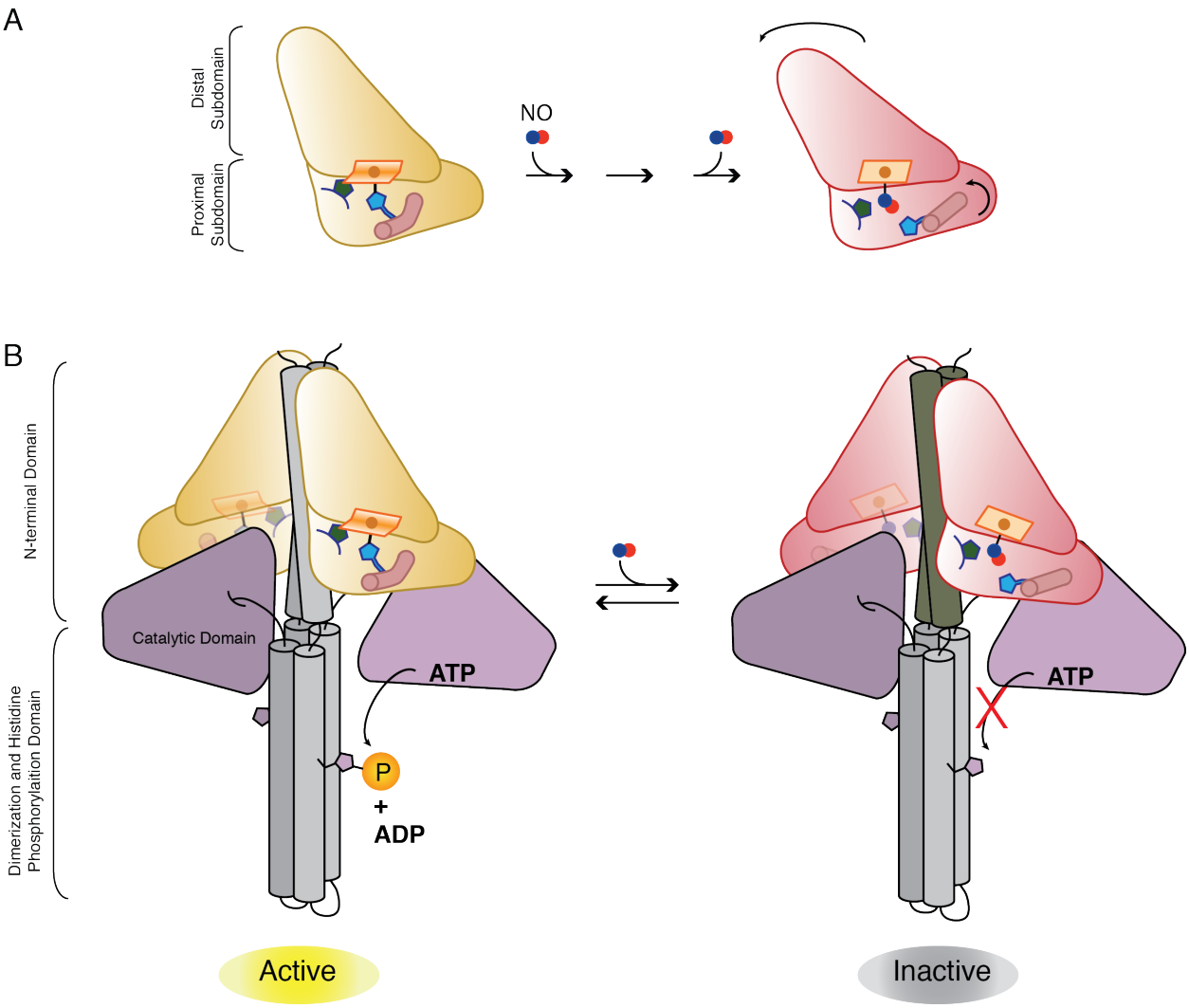

Figure 5.7 Proposed model for H-NOX-dependent inhibition of histidine kinase activity in *Shewanella oneidensis*. (**A**) Binding of NO to the H-NOX domain (gold) results in cleavage of the heme-histidine bond that then, via several interconnected structural changes, elicits a rotational displacement of the distal subdomain with respect to the proximal subdomain to yield the inhibitory H-NOX conformation (red) (*see* **Chapter 3**). (**B**) The H-NOX/histidine kinase cognate pair in *S. oneidensis* exists as a 2:2 H-NOX:HK heterotetramer with the H-NOX protein bound to the kinase via interactions with the N-terminal domain of the HK. In the basal state, the histidine kinase (gray) is constitutively active and catalyzes ATP-dependent autophosphorylation of a conserved histidine residue (purple pentagon). The NO-induced conformational change in the H-NOX is then transduced to the histidine kinase that, through an as of yet unknown mechanism, inhibits kinase autophosphorylation.

Fe^{III}, etc.) with histidine kinase constructs and nucleotide states (ADP, ATP, AMPPNP, AMPPCP, etc.) were screened. However, efforts using heme-bound H-NOX were fruitless.

Chapter 3 documented successful screening and crystallization of manganese protoporphyrin IX (MnPPIX)-substituted H-NOX. During these trials it was observed that MnPPIX-substituted H-NOX was much less susceptible to auto-oxidation as compared to the heme-bound protein, exhibiting a half-life of the Mn^{II} species of ~48 hours as compared to a half-life of ~8 hours for the Fe^{II} species (data not shown). Therefore, in an effort to reduce the

heterogeneity of the H-NOX population that would result following oxidation of the heme, complexes of MnPPIX H-NOX: histidine kinase were screened. Utilizing the same combinatorial approach as for heme-containing H-NOX, crystals of MnPPIX H-NOX with a TEV-cleaved hexahistidine tag in complex with a kinase dead (H72E) mutant of the full-length histidine kinase in the presence of AMPPNP were obtained (**Figure 5.6A**). In order to confirm that both components of the complex were intact in the crystals, numerous crystals were washed and analyzed by SDS-PAGE. Coomassie staining reveals that both components are present in the crystals at approximately equal concentrations as estimated by band intensity (**Figure 5.6B**). Furthermore, the approximate molecular weight of each component from the crystals matches the molecular weight of the corresponding purified protein used for crystallization thereby indicating that there was no proteolysis of either component. (**Figure 5.6B**).

Crystals of the MnPPIX H-NOX: histidine kinase (H72E) complex diffracted maximally to ~8 Å resolution with a severe loss of diffraction in the 10-8 Å resolution range (**Figure 5.6C**). Analysis of the diffraction images reveals that the crystals belong to a hexagonal space group ($P6_x$) with unit cell dimensions of approximately 205x205x235 Å (α=90°, β=90°, and γ=120°). Using this information, a calculation of the Matthew's coefficient – an estimation of the solvent content in the asymmetric unit (asu) given the components within the crystals and estimates of protein density – reveals that the asu probably contains 2 copies of the 110 kDa heterotetramer (volume of unit cell= 8552758.6 $Å^3$, 63% solvent content, ~220 000 daltons in asu) (45). Efforts to extend diffraction to a resolution amenable to structure determination – including micro- and macro-seeding, screening for additive compounds (i.e. salts, polyols, metals, etc.), and crystal dehydration – have been unsuccessful. Further efforts to extend diffraction using surface mutations or N-terminal/C-terminal truncations are being pursued.

Conclusion

Together, these data provide a model describing the architecture of the H-NOX: histidine kinase complex as well as a potential mechanism by which H-NOX proteins transduce NO binding to their cognate signaling partners (**Figure 5.7**). The H-NOX: histidine kinase complex exists as a 2:2 heterotetramer with a H-NOX bound to the N-terminal coiled-coil domain of each histidine kinase protomer. In the absence of NO, the histidine kinase remains constitutively active and catalyzes the ATP-dependent autophosphorylation of a conserved histidine residue located in the dimerization and histidine phosphorylation (DHp) domain. The phosphoryl group is then transferred to a downstream response regulator that participates in regulating the motility of the organism. Upon binding NO, the H-NOX undergoes a conformational change involving a rotational displacement of the distal subdomain about the proximal subdomain. This alteration of relative orientation of the distal and proximal subdomains is hypothesized to be communicated to the kinase dimerization domain via conformational changes in the kinase N-terminal coiled-coil domain. Ultimately, NO binding results in inactivation of the histidine kinase via rotation of the helices within the DHp four-helix bundle to place the phospho-accepting histidine in an orientation inaccessible by the catalytic domain and, thus, incapable of being autophosphorylated.

References

1. Ignarro LJ, Cirino G, Casini A, & Napoli C (1999) Nitric oxide as a signaling molecule in the vascular system: an overview. *J Cardiovasc Pharmacol* 34:879–886.
2. Bredt DS, & Snyder SH (1992) Nitric oxide, a novel neuronal messenger. *Neuron*. 8:3-11
3. Moncada S, Palmer RM, Higgs EA (1991) Nitric oxide: physiology, pathophysiology, and pharmacology. *Pharmacological reviews*.
4. Derbyshire ER, & Marletta MA (2009) Biochemistry of Soluble Guanylate Cyclase - Springer. *cGMP: Generators*.
5. Denninger JW, & Marletta MA (1999) Guanylate cyclase and the ·NO/cGMP signaling pathway. *Biochimica et Biophysica Acta* 1411:334-350.
6. Iyer LM, Anantharaman V, & Aravind L (2003) Ancient conserved domains shared by animal soluble guanylyl cyclases and bacterial signaling proteins. *BMC Genomics* 4:5.
7. Karow DS, Pan D, Tran R, Pellicena P, Presley A, Mathies RA, & Marletta MA (2004) Spectroscopic Characterization of the Soluble Guanylate Cyclase-like Heme Domains from *Vibrio cholerae* and *Thermoanaerobacter tengcongensis*. *Biochemistry* 43:10203–10211.
8. Boon EM, Huang SH, & Marletta MA (2005) A molecular basis for NO selectivity in soluble guanylate cyclase. *Nat Chem Biol* 1:53–59.
9. Boon EM, Davis JH, Tran R, Karow DS, Huang SH, Pan D, Miazgowicz MM, Mathies RA, & Marletta MA (2006) Nitric oxide binding to prokaryotic homologs of the soluble guanylate cyclase beta1 H-NOX domain. *J Biol Chem* 281:21892–21902.
10. Price MS, Chao LY, & Marletta MA (2007) *Shewanella oneidensis* MR-1 H-NOX Regulation of a Histidine Kinase by Nitric Oxide. *Biochemistry* 46:13677–13683.
11. Wu G, Liu W, Berka V, & Tsai A-L (2013) The selectivity of *Vibrio cholerae* H-NOX for gaseous ligands follows the "sliding scale rule" hypothesis. Ligand interactions with both ferrous and ferric *Vc* H-NOX. *Biochemistry* 52:9432–9446.
12. Ma X, Sayed N, Beuve A, & van den Akker F (2007) NO and CO differentially activate soluble guanylyl cyclase via a heme pivot-bend mechanism. *The EMBO Journal* 26:578–588.
13. Plate L, & Marletta MA (2013) Nitric oxide-sensing H-NOX proteins govern bacterial communal behavior. *Trends in Biochemical Sciences* 38:566–575.
14. Pirrung MC (1999) Histidine kinases and two-component signal transduction systems. *Chemistry & biology* 6:R167–R175.
15. Laub MT, & Goulian M (2007) Specificity in Two-Component Signal Transduction Pathways. *Annu Rev Genet* 41:121–145.
16. Szurmant H, White RA, & Hoch JA (2007) Sensor complexes regulating two-component signal transduction. *Current Opinion in Structural Biology* 17:706–715.
17. Baker MD, Wolanin PM, & Stock JB (2005) Signal transduction in bacterial chemotaxis. *Bioessays* 28:9–22.
18. Yoshida T, Phadtare S, & Inouye M (2007) *Methods in Enzymology*.
19. Piggot PJ, & Hilbert DW (2004) Sporulation of Bacillus subtilis. *Current Opinion in Microbiology* 7:579–586.
20. Skerker JM, Prasol MS, Perchuk BS, Biondi EG, & Laub MT (2005) Two-Component Signal Transduction Pathways Regulating Growth and Cell Cycle Progression in a Bacterium: A System-Level Analysis. *PLoS Biol* 3:e334.

21. Paul R, Jaeger T, Abel S, Wiederkehr I, Folcher M, Biondi EG, Laub MT, & Jenal U (2008) Allosteric Regulation of Histidine Kinases by Their Cognate Response Regulator Determines Cell Fate. *Cell* 133:452–461.
22. Bourret RB (2010) Receiver domain structure and function in response regulator proteins. *Current Opinion in Microbiology* 13:142–149.
23. Gao R, Mack TR, & Stock AM (2007) Bacterial response regulators: versatile regulatory strategies from common domains. *Trends in Biochemical Sciences* 32:225–234.
24. Stock AM, Robinson VL, & Goudreau PN (2010) Two-Component Signal Transduction. *Ann Rev Biochem* 69:183-215.
25. Carlson HK, Vance RE, & Marletta MA (2010) H-NOX regulation of c-di-GMP metabolism and biofilm formation in *Legionella pneumophila*. *Mol Microbiol* 77(**4**):930-942.
26. Wang Y, Dufour YS, Carlson HK, Donohue TJ, Marletta MA, & Ruby EG (2010) H-NOX–mediated nitric oxide sensing modulates symbiotic colonization by Vibrio fischeri. *Proc Natl Acad Sci USA* 107:8375.
27. Plate L, & Marletta MA (2012) Nitric Oxide Modulates Bacterial Biofilm Formation through a Multicomponent Cyclic-di-GMP Signaling Network. *Molecular Cell* 46:449–460.
28. Henares B, Xu Y, & Boon E (2013) A Nitric Oxide-Responsive Quorum Sensing Circuit in *Vibrio harveyi* Regulates Flagella Production and Biofilm Formation. *IJMS* 14:16473–16484.
29. Plate L, & Marletta MA (2013) Phosphorylation-dependent derepression by the response regulator HnoC in the Shewanella oneidensis nitric oxide signaling network. *Proc Natl Acad Sci* E4648-4657.
30. Busso D, Delagoutte-Busso B, & Moras D (2005) Construction of a set Gateway-based destination vectors for high-throughput cloning and expression screening in Escherichia coli. *Analytical Biochemistry* 343:313–321.
31. Schneider CA, Rasband WS, & Eliceiri KW (2012) NIH Image to ImageJ: 25 years of image analysis. *Nat Methods* 9(**7**) 671-675.
32. Underbakke ES, Iavarone AT, & Marletta MA (2013) Higher-order interactions bridge the nitric oxide receptor and catalytic domains of soluble guanylate cyclase. *Proc Natl Acad Sci 110:6777-6782*.
33. Weis DD, Engen JR, & Kass IJ (2006) Semi-automated data processing of hydrogen exchange mass spectra using HX-Express. *J Am Soc Mass Spectrom* 17:1700–1703.
34. Bick MJ, Lamour V, Rajashankar KR, Gordiyenko Y, Robinson CV, & Darst SA (2009) How to Switch Off a Histidine Kinase: Crystal Structure of *Geobacillus stearothermophilus* KinB with the inhibitor Sda. *Journal of Molecular Biology* 386:163–177.
35. Dutta R, Qin L, & Inouye M (1999) Histidine kinases: diversity of domain organization. *Mol Microbiol* 34:633–640.
36. Gao R, & Stock AM (2009) Biological Insights from Structures of Two-Component Proteins. *Annu Rev Microbiol* 63:133–154.
37. Song Y, Peisach D, Pioszak AA, Xu Z, & Ninfa AJ (2004) Crystal Structure of the C-terminal Domain of the Two-Component System Transmitter Protein Nitrogen Regulator II (NRII; NtrB), Regulator of Nitrogen Assimilation in *Escherichia coli*. *Biochemistry* 43:6670–6678.

38. Ashenberg O, Rozen-Gagnon K, Laub MT, & Keating AE (2011) Determinants of Homodimerization Specificity in Histidine Kinases. *Journal of Molecular Biology* 413:222–235.
39. Marina A, Waldburger CD, & Hendrickson WA (2005) Structure of the entire cytoplasmic portion of a sensor histidine-kinase protein. *The EMBO Journal* 24:4247–4259.
40. Casino P, Rubio V, & Marina A (2010) The mechanism of signal transduction by two-component systems. *Current Opinion in Structural Biology*:1–9.
41. Kim KK, Yokota H, & Kim SH (1999) Four-helical-bundle structure of the cytoplasmic domain of a serine chemotaxis receptor. *Nature* 400:787–792.
42. Hulko M, Berndt F, Gruber M, Linder JU, Truffault V, Schultz A, Martin J, Schultz JE, Lupas AN, & Coles M (2006) The HAMP Domain Structure Implies Helix Rotation in Transmembrane Signaling. *Cell* 126:929–940.
43. Zhu Y, & Inouye M (2004) The HAMP Linker in Histidine Kinase Dimeric Receptors Is Critical for Symmetric Transmembrane Signal Transduction. *Journal of Biological Chemistry* 279:48152–48158.
44. Ferris HU, Dunin-Horkawicz S, Hornig N, Hulko M, Martin J, Schultz JE, Zeth K, Lupas AN, & Coles M (2012) Mechanism of Regulation of Receptor Histidine Kinases. *Structure/Folding and Design* 20:56–66.
45. Kantardjieff KA, & Rupp B (2003) Matthews coefficient probabilities: Improved estimates for unit cell contents of proteins, DNA, and protein-nucleic acid complex crystals. *Protein Science* 12:1865–1871.

CHAPTER 6

Future Directions

Summary

In this final chapter, suggestions for future experiments are provided for each project.

Future Directions

Ligand Diffusion in H-NOX Proteins. Experimental evidence has been provided in **Chapter 2** to understand the functional influence of the H-NOX protein scaffold on modulating the diffusion of gas molecules as a means to tune gas-sensing properties.

Future work in this area should employ molecular dynamics (MD) simulations as a means to further investigate the hypothesis that incorporation of tunnel-blocking mutations affect ligand-binding properties by trapping ligands near the heme site. Previous studies to investigate gas diffusion in H-NOX proteins monitored the migration of CO molecules from the interior heme site to solvent following *in silico* cleavage of the iron-CO bond in Wt *Ns* H-NOX (1). These studies corroborate the experimental evidence provided in **Chapter 2** indicating that the tunnel network serves as the preferred ligand migration pathway for gas molecules to and from the interior heme site. For each of the tunnel-blocking mutants investigated in **Chapter 2**, a similar MD simulation protocol could be used as described in (1) to provide insight into differences in the preferred migration pathway as well as the lifetime of the CO molecule(s) within the protein matrix upon blocking either or both of the tunnels. Of particular interest would be investigating the migration of gas molecules in the double mutant L66W/L67W as this mutant was shown to block both tunnels, yet, the binding of gas molecules was not completely abolished. It is possible that very transient pockets and/or gas migration pathways develop as a result of protein dynamics that allow for gases to enter and exit the protein matrix of the L66W/L67W mutant.

Additional experiments are provided in the dissertation of Michael B. Winter, Ph.D. entitled "Tuning Sensing and Signaling in the H-NOX Family of Heme Proteins."

Distal and Proximal-Bound Nitrosyl Species. Interest to elucidate the molecular mechanism by which cleavage of the iron-histidine bond activates H-NOX proteins led to the observation that NO is capable of binding to the proximal heme face. Importantly, this provides evidence that H-NOX proteins are capable of binding NO as five-coordinate complexes in both the distal and proximal heme pockets. A wealth of biochemical and kinetic data point to potential differences in these two nitrosyl species. However, it is hypothesized that, regardless of the location of the NO, be it distal or proximal, the structural changes that occur following scission of the iron-histidine bond would be similar. Support of this hypothesis has remained elusive, as structure determination of a five-coordinate, distal-bound NO complex has proven remarkably difficult. Within the context of this dissertation, following crystallization of the proximal-bound 5cNO structure, crystallization trials with H-NOX prepared using a substoichiometric

concentration of NO were pursued using similar conditions, but to no avail. Perhaps the most daunting task with crystallizing this nitrosyl complex is maintaining NO concentrations within the crystal well such that an adequate concentration of NO-bound H-NOX is present for crystallization whilst not surpassing the stoichiometric ratio of NO: protein that favors NO binding to the proximal pocket. One potential method to achieve this would be to attempt crystallization using different ratios of chemical-based NO donors (i.e. NONOates), with different half-lives, in order to maintain the proper NO: protein ratio, prior and post equilibration of the crystal well, for maintaining only a population of the distal-bound NO complex.

In an effort to determine the differences in the NO lifetime between distal and proximal-bound species, NO dissociation rates were measured (**Chapter 4**). Critical to these experiments is the assumption that each NO species could be isolated by incubating the H-NOX with different ratios of NO. However, because both species are identical by UV-vis spectroscopy, there was no way to be 100% confident that a homogenous population of either species was isolated. Thus future efforts should investigate methods to discern the two nitrosyl species. One such methodology could employ the use of small, thiol-based spin labels to modify Cys141 in the distal pocket of *So* H-NOX and compare the electron paramagnetic resonance (EPR) spectra upon incubation with different molar ratios of NO (2, 3). It is possible that the two alternate nitrosyl complexes would affect the resonance of the spin-label differently. Specifically, the distal-bound NO would be in much closer proximity (<6 Å) as compared to proximal-bound NO (>8 Å) and the change in chemical environment may alter the resonance spectrum of the spin probe. Additionally, differences in spin label distances may be discernable using methodologies described in (3).

H-NOX Regulation of Histidine Kinase Autophosphorylation. In an effort to understand the molecular mechanism by which H-NOX proteins communicate ligand-binding to their signaling effector proteins, structural characterization of the H-NOX: histidine kinase complex from *Shewanella oneidensis* was performed (**Chapter 5**). Although the work presented in this dissertation provided insights into the overall architecture of the complex, several questions pertaining to the H-NOX-induced structural changes within the histidine kinase remain.

Conceivably, the most informational follow-up experiment from these results would be determination of the H-NOX: histidine kinase complex structure. As such, initial future efforts should focus on optimization of the H-NOX: histidine kinase crystals to obtain a resolution of diffraction adequate for structure determination (4). Attempts thus far have included sparse-matrix screening for additive compounds (i.e. salts, polyols, metals, etc.), micro- and macro-seeding, as well as dehydration. However, increases in crystal and diffraction qualities have been minimal. One avenue for future efforts would be to focus on adding additional steps during the purification of the protein components, in an effort to eliminate any heterogeneity within the protein sample, altering the crystallization constructs via N-terminal or C-terminal truncations, as well as screening complexes comprised of the 154AAA mutant of *So* H-NOX. Additionally, following the success of surface entropy reduction on crystallization of the free H-NOX, the amino acid sequence of HK2145 should be subjected to the SERp server for analysis with particular emphasis on regions distant from the H-NOX binding site (5). It must be noted, however, that any of these alterations may, in fact, eliminate crystallization in the current

condition and sparse-matrix screening would be required to obtain an alternate condition. Lastly, in an attempt to obtain and orthogonal crystallization condition using the current complex components, sparse-matrix micro-seeding could be an attractable option (6, 7).

In lieu of a crystal structure of the complex, additional alanine-scanning mutagenesis experiments to validate the putative histidine kinase binding interface on the H-NOX, as mapped by hydrogen/deuterium exchange by mass-spectrometry (HDX-MS), should be performed. Initial experiments using this technique identified K108 on the H-NOX as a primary contributor to stabilizing the H-NOX: histidine kinase interface. However, none of the other alanine mutations at the predicted interface resulted in an observed decrease in histidine kinase binding affinity, at least as determined by a pull-down assay. Using the same library of mutants generated in **Chapter 5**, pull-down experiments should be repeated using lower concentrations of the complex components to determine if the lack of observed differences are a result of the components being at concentrations significantly greater than the K_D of the complex. Additionally, alternate mutations that are predicted to be more disruptive, i.e. charge swap or introducing charged amino acids at non-polar sites, should be pursued using the same methodologies.

References

1. Zhang Y, Lu M, Cheng Y, & Li Z (2010) H-NOX domains display different tunnel systems for ligand migration. *Journal of Molecular Graphics and Modelling* 28:814–819.
2. Pohl T, Spatzal T, Aksoyoglu M, Schleicher E, Rostas AM, Lay H, Glessner U, Boudon C, Hellwig P, Weber S, & Friedrich T (2010) Spin labeling of the Escherichia coli NADH ubiquinone oxidoreductase (complex I). *Biochim Biophys Acta* 1797:1894–1900.
3. Steinhoff HJ, Radzwill N, Thevis W, Lenz V, Brandenburg D, Antson A, Dodson G, & Wollmer A (1997) Determination of interspin distances between spin labels attached to insulin: comparison of electron paramagnetic resonance data with the X-ray structure. *Biophysical Journal* 73:3287–3298.
4. Heras B, & Martin JL (2005) Post-crystallization treatments for improving diffraction quality of protein crystals. *Acta Cryst (2005) D61, 1173-1180*.
5. Goldschmidt L, Cooper DR, Derewenda ZS, & Eisenberg D (2007) Toward rational protein crystallization: A Web server for the design of crystallizable protein variants. *Protein Science* 16:1569–1576.
6. D'Arcy A, Villard F, & Marsh M (2007) An automated microseed matrix-screening method for protein crystallization. *Acta Crystallogr D Biol Crystallogr* 63:550–554.
7. St John FJ, Feng B, & Pozharski E (2008) The role of bias in crystallization conditions in automated microseeding. *Acta Crystallogr D Biol Crystallogr* 64:1222–1227.

Appendix A

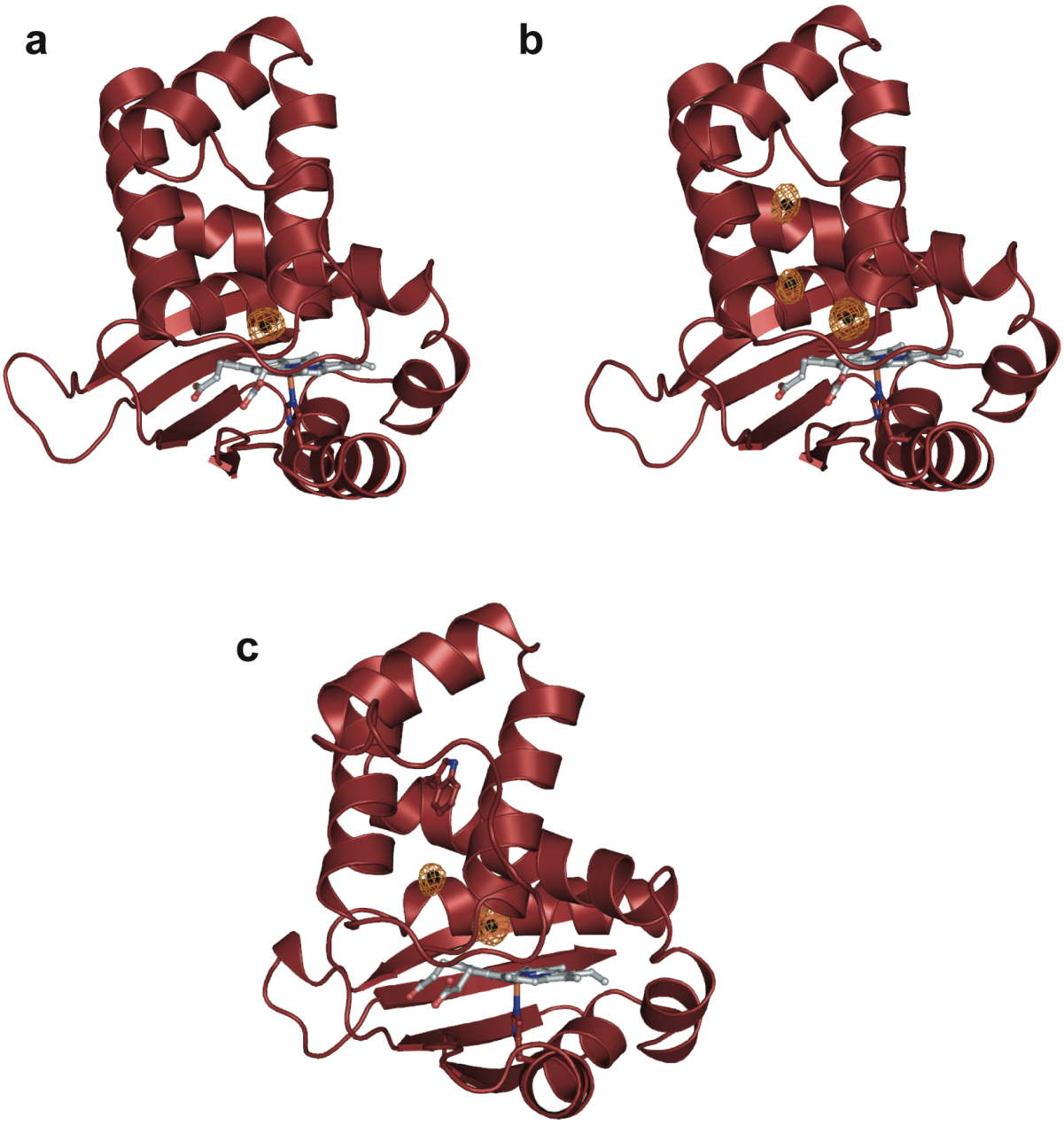

Figure A.1 Crystal structures of WT *Ns* H-NOX following pressurization with (**a**) 1 atm of xenon and (**b**) 6 atm of xenon. (**c**) Crystal structure of L66W *Ns* H-NOX following pressurization with 6 atm of xenon. Anomalous density (mesh surface) for xenon atoms is contoured at 5σ.

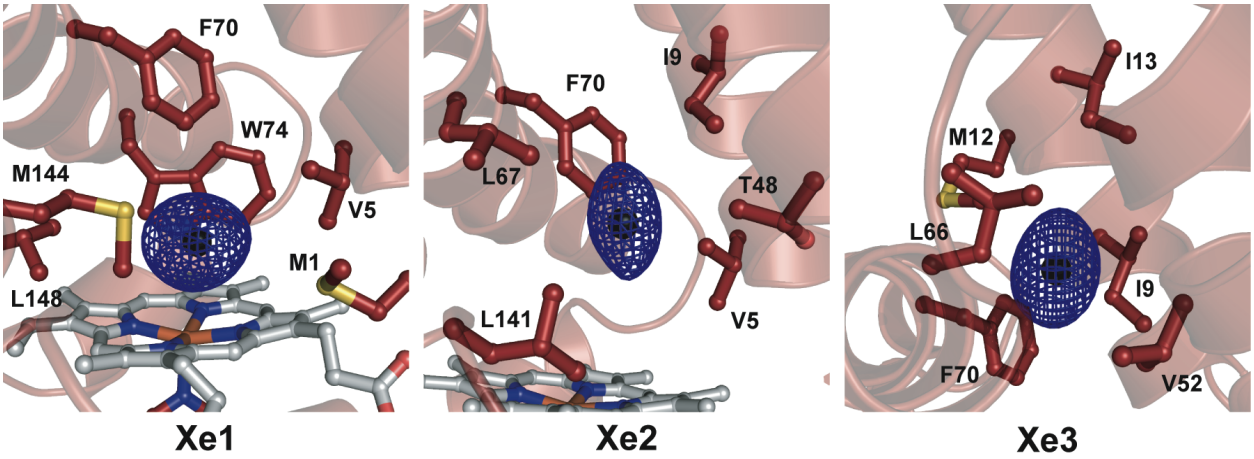

Figure A.2 Xenon binding sites in the crystal structure of WT *Ns* H-NOX pressurized with 6 atm of xenon. The Xe1, Xe2, and Xe3 sites are depicted individually with surrounding tunnel residues. $2mF_o–DF_c$ map (mesh surface) is contoured at 1σ.

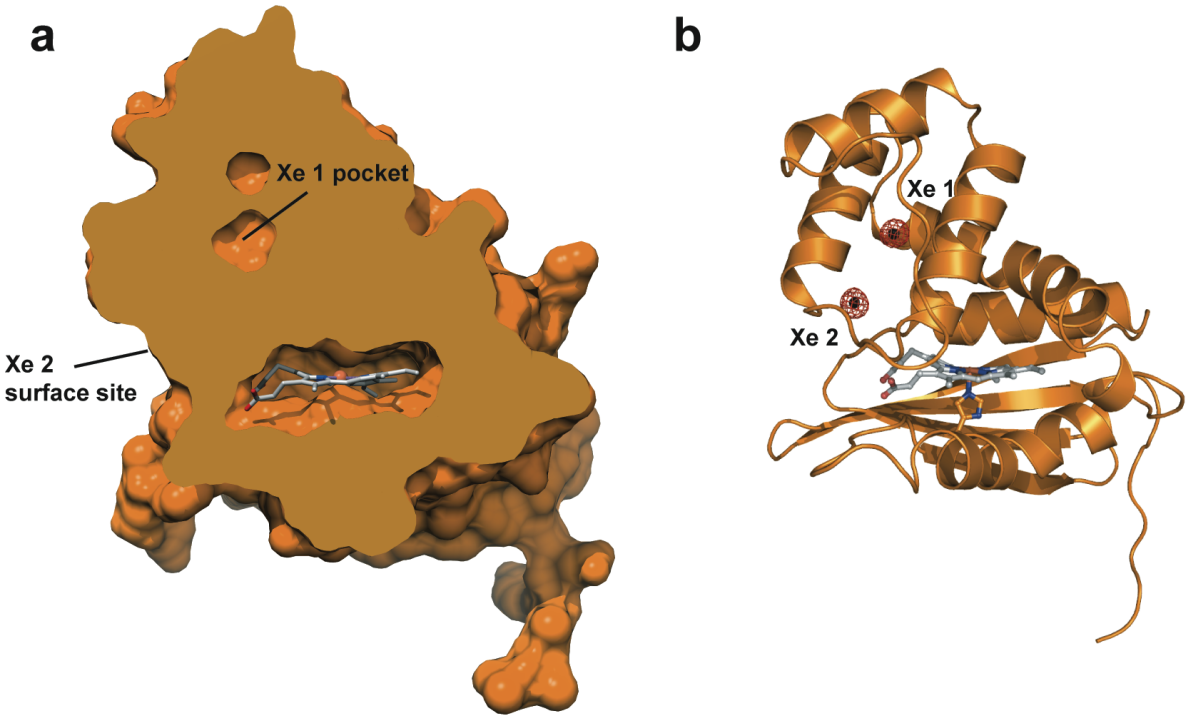

Figure A.3 Crystal structure of *Tt* H-NOX pressurized with 6 atm of xenon for 1 min. (**a**) Surface representation of *Tt* H-NOX showing a cross-sectional view with xenon binding sites labeled. (**b**) Cartoon representation of *Tt* H-NOX with anomalous density (mesh surface) for xenon atoms contoured at 5σ. See **Table A.2** for crystallography data collection and refinement statistics.

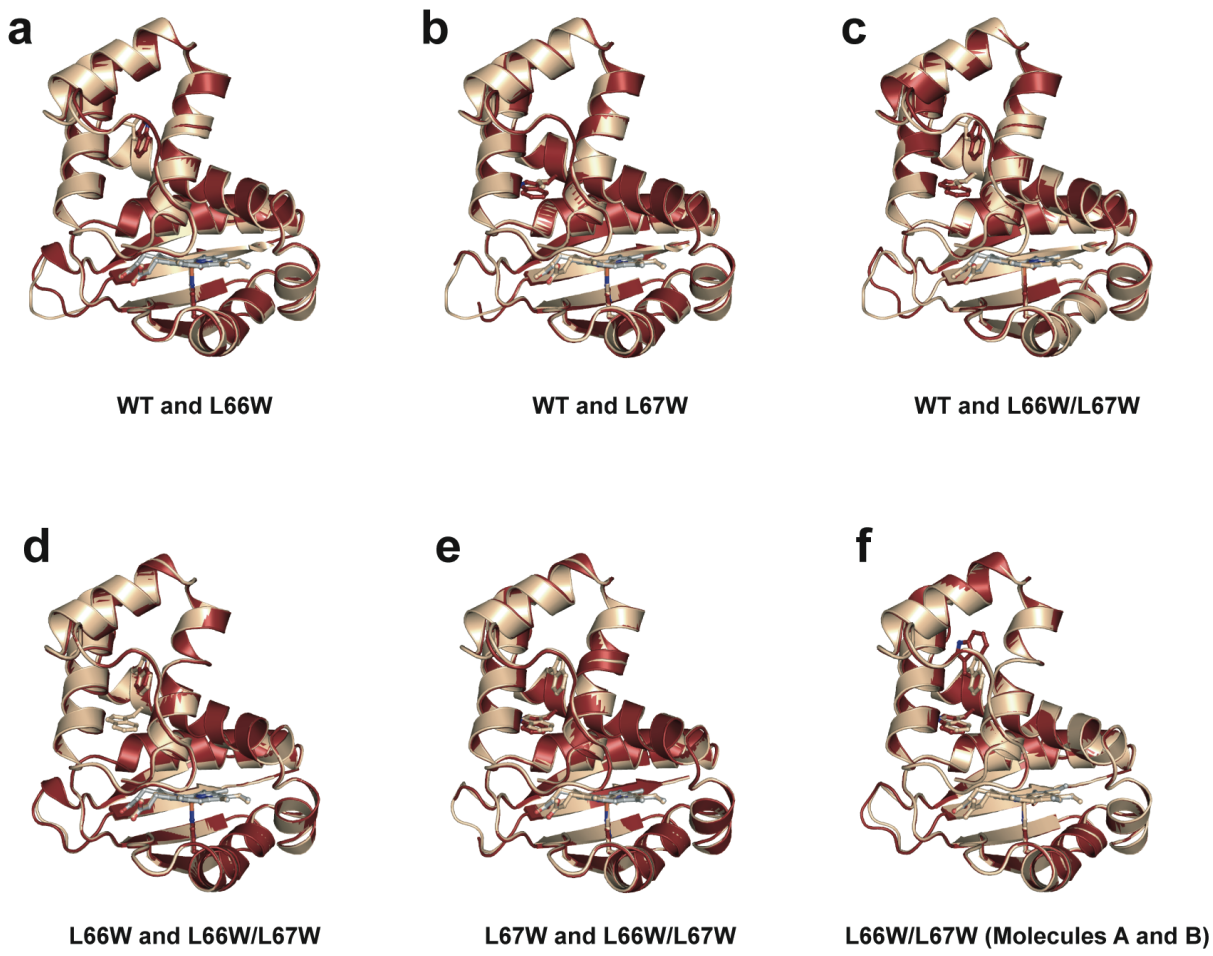

Figure A.4 Overall structural alignments for *Ns* H-NOX variants. Alignments are shown for WT *Ns* H-NOX with (**a**) L66W, (**b**) L67W, and (**c**) L66W/L67W. Alignments are also shown for L66W/L67W with (**d**) L66W, (**e**) L67W, and (**f**) L66W/L67W (molecule B). Molecule A was utilized for all alignments except where noted.

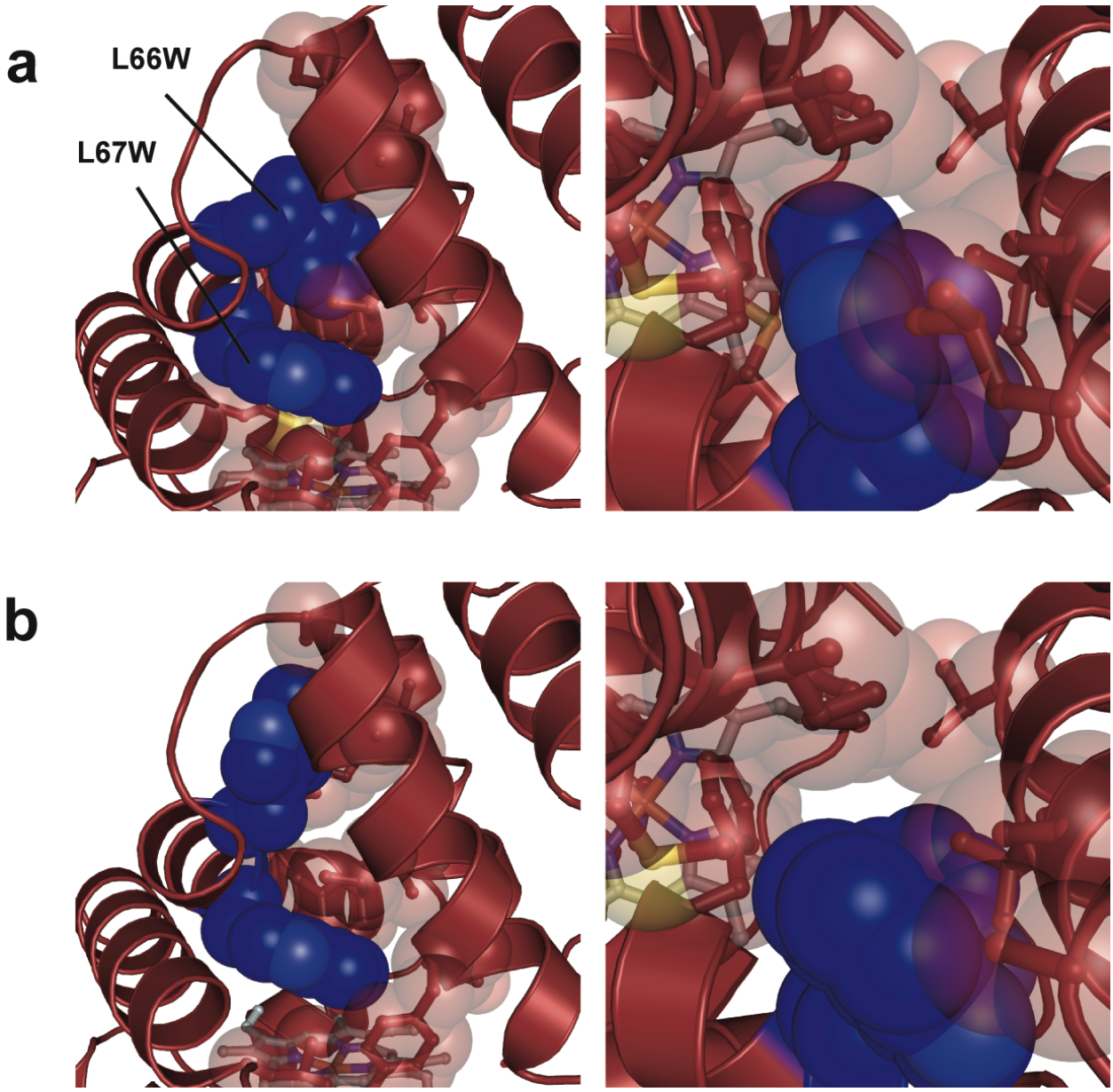

Figure A.5 L66W rotamers in the L66W/L67W double mutant crystal structure. (**a**) Molecule A from (**left**) "side" and (**right**) "top-down" views. (**b**) Molecule B from (**left**) "side" and (**right**) "top-down" views. The tryptophan side chains in molecule A of the double mutant structure are positioned similarly to the side chains in the L66W and L67W single mutant structures. The alternate L66W rotamer in molecule B appears to not be as effective in sterically blocking tunnel 1 (see "top-down" view). Molecules A and B superimpose to a high degree overall (see **Figure A.4F**).

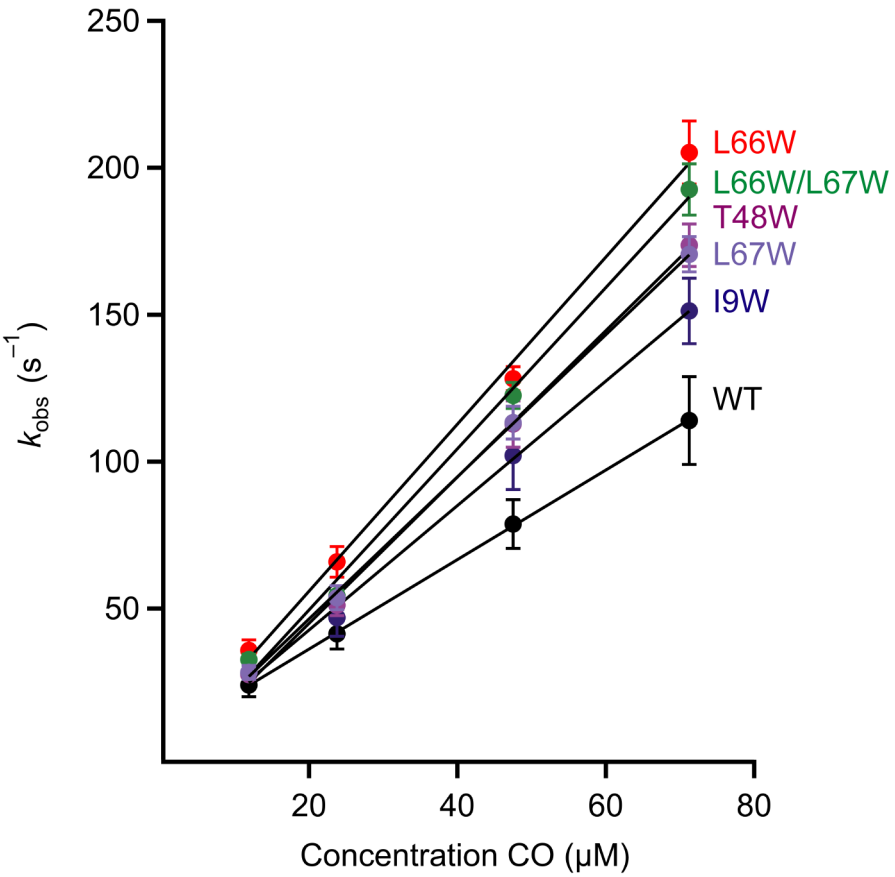

Figure A.6 Observed CO binding rates (k_{obs}) for *Ns* H-NOX variants determined with stopped flow spectroscopy. Final CO concentrations of 11.9, 23.8, 47.5, and 71.3 μM were utilized. N = 3-5. Error bars represent the standard deviation.

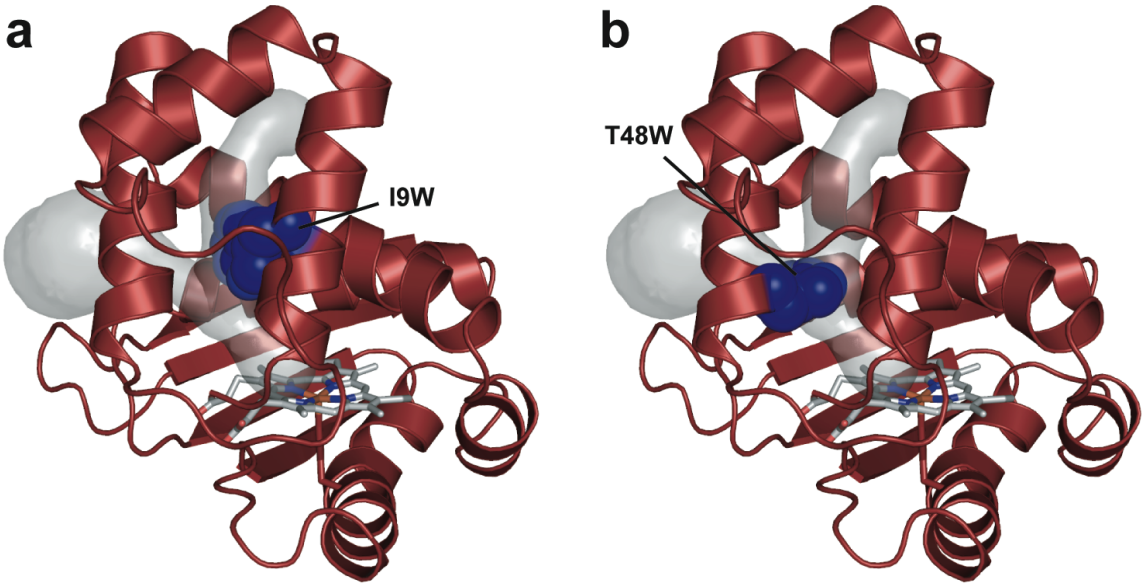

Figure A.7 I*n silico* representations of (**a**) I9W and (**b**) T48W. Mutagenesis and modeling of allowed rotamers was carried out in Coot. The most favorable rotamer for each side chain is shown. The tunnel network was modeled using CAVER on the WT *Ns* H-NOX structure with the heme iron as the point of origin.

Table A.1 WT *Ns* H-NOX crystallography data collection and refinement statistics.

	WT *Ns* H-NOX		
	Native	**1 atm Xe**	**6 atm Xe**
Wavelength (Å)	0.97	1.40	1.40
Space group	$P2_13$	$P2_13$	$P2_13$
Cell dimensions			
$a = b = c$ (Å)	123.7	124.4	123.9
$\alpha = \beta = \gamma$ (°)	90	90	90
Resolution (Å)	50.00-2.13 (2.17-2.13)	50.00-2.59 (2.63-2.59)	50.00-2.27 (2.31-2.27)
Redundancy	5.6 (5.6)	6.3 (6.1)	6.3 (5.9)
Completeness[a] (%)	99.9 (100.0)	99.5 (100.0)	99.5 (97.9)
R_{sym} (%)	6.5 (63.4)	7.3 (61.6)	5.4 (28.1)
I / σ	23.6 (3.2)	20.4 (2.78)	30.2 (5.76)
No. of reflections	38528	40549	55256
R_{work}/R_{free} (%)	16.4/20.0	17.7/21.4	16.2/19.0
Molecules in AU	2	2	2
No. atoms			
Protein[b]	2886	2819	2779
Heme	96	96	96
Xenon	0	2	6
Solvent	224	20	90
Rms deviation			
Bond lengths (Å)	0.010	0.021	0.010
Bond angles (°)	1.233	1.881	1.267
Xenon Occupancy			
Molecule A		0.3[c]	0.6,[c] 0.3,[d] 0.4[e]
Molecule B		0.3[c]	0.7,[c] 0.4,[d] 0.5[e]

[a] Overall completeness. [b] Non-hydrogen atoms. [c] Xe1. [d] Xe2. [e] Xe3.

Table A.2 Mutant *Ns* H-NOX crystallography data collection and refinement statistics.

	L66W		L67W	L66W/ L67W
	Native	**6 atm Xe**	**Native**	**Native**
Wavelength (Å)	0.97	1.40	0.97	0.97
Space group	$P2_13$	$P2_13$	$P2_13$	$P2_13$
Cell dimensions				
$a = b = c$ (Å)	123.2	123.3	123.2	123.1
$\alpha = \beta = \gamma$ (°)	90	90	90	90
Resolution (Å)	50.00-1.96 (1.99-1.96)	50.00-1.99 (2.02-1.99)	50.00-1.94 (1.97-1.94)	50.00-1.90 (1.93-1.90)
Redundancy	5.5 (5.6)	6.8 (6.5)	6.8 (6.8)	6.8 (6.8)
Completeness[a] (%)	100.0 (100.0)	100.0 (100.0)	100.0 (100.0)	100.0 (100.0)
R_{sym} (%)	4.9 (64.6)	5.6 (68.3)	5.5 (61.5)	6.2 (62.5)
I / σ	29.9 (2.28)	28.7 (2.91)	29.8 (3.70)	28.2 (3.32)
No. of reflections	43497	79661	48228	51187
R_{work}/R_{free} (%)	16.3/18.7	15.6/17.3	16.5/18.8	16.0/18.3
Molecules in AU	2	2	2	2
No. atoms				
Protein[b]	2890	2875	3038	3022
Heme	96	96	96	96
Xenon	0	4	0	0
Solvent	205	191	247	262
Rms deviation				
Bond lengths (Å)	0.009	0.009	0.009	0.018
Bond angles (°)	1.290	1.227	1.251	1.661
Xenon Occupancy				
Molecule A		0.3,[c] 0.1[d]		
Molecule B		0.4,[c] 0.1[d]		

[a] Overall completeness. [b] Non-hydrogen atoms. [c] Xe1. [d] Xe2. [e] Xe3.

Table A.3 *Tt* H-NOX crystallography data collection and refinement statistics.

	WT *Tt* H-NOX	
	Native	**6 atm Xe**
Wavelength (Å)	0.977	1.23
Space group	$P2_12_12$	$P2_12_12$
Cell dimensions		
a, *b*, *c* (Å)	80.5, 130.7, 42.7	80.1, 130.2, 42.8
$\alpha = \beta = \gamma$ (°)	90	90
Resolution (Å)	50.00-1.74 (1.77-1.74)	50.00-2.03 (2.07-2.03)
Redundancy	6.6 (6.3)	4.2 (4.0)
Completeness[a] (%)	95.4 (89.5)	99.8 (99.1)
R_{sym} (%)	6.7 (55.1)	7.9 (62.4)
I / σ	23.39 (2.43)	17.11 (2.16)
No. of reflections	44302	52372
R_{work}/R_{free} (%)	20.2/22.9	17.9/21.9
Molecules in AU	2	2
No. atoms		
Protein[b]	3059	3003
Heme	96	96
O_2	2	2
Xenon	0	4
Solvent	111	145
Rms deviation		
Bond lengths (Å)	0.008	0.017
Bond angles (°)	0.992	1.482
Xenon Occupancy		
Molecule A		0.8,[c] 0.5[d]
Molecule B		0.7,[c] 0.4[d]

[a] Overall completeness. [b] Non-hydrogen atoms. [c] Xe1. [d] Xe2.

Table A.4. UV−visible spectral features of *Ns* H-NOX variants.

	Absorbance (nm)				
Protein	**Unligated**	**Fe^{II}−CO**	**Fe^{II}−NO**	**$Fe^{II}-O_2$**	***Ref.*[b]**
***Ns* H-NOX** (Wild-type)	431 558	424 539 565	399[a] / 417 545 573	n.o	
L67W	431 558	423 541 566	399[a] / 417 544 573	n.o.	
L66W	430 558	424 541 566	399[a] / 417 544 573	n.o.	
L66W/L67W	431 560	423 541 569	399[a] / 417 544 573	n.o.	
T48W	430 558	423 539 567	399[a] / 418 544 573	n.o.	
I9W	431 557	424 538 566	399[a] / 417 544 574	n.o.	
***Tt* H-NOX**	431 565	424 544 565	420 547 575	416 556 591	(44)
sGC	431 555	423 541 567	398 537 572	n.o.	(55)

[a]Shoulder. [b] This work unless otherwise noted. n.o. = not observed.

Appendix B

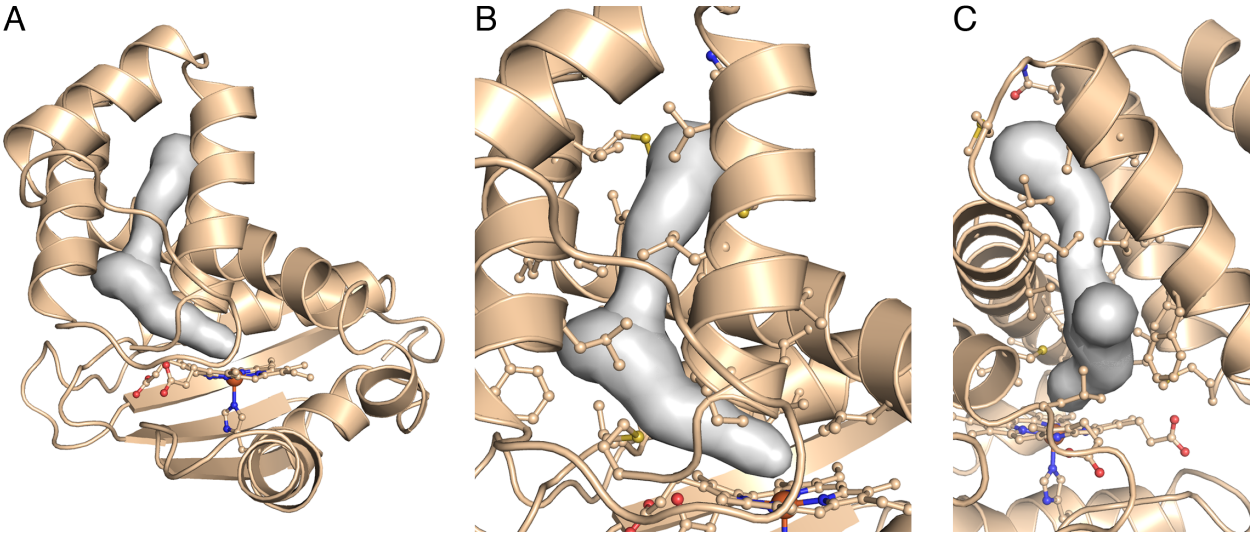

Figure B.1 Distal pocket tunnel network in *So* H-NOX. (**A**) Cartoon representation of the Fe^{II} *So* H-NOX crystal structure with the tunnel network displayed as grey surface. The tunnel network was modeled using CAVER (1) with the heme iron as the point of origin and a probe radius of 1.5 Å. Panels B and C show zoomed in views of the distal subdomain with residues that buttress the tunnels shown as sticks. The observation that the distal pocket of *So* H-NOX possesses hydrophobic residues that line a branched tunnel network originating from the distal heme pocket connecting to the solvent is analogous to those tunnels observed in *Ns* H-NOX that were recently shown to be important for tuning the ligand-binding properties (2).

References

1. 1. Chovancova E, Pavelka A, Benes P, Strnad O, Brezovsky J, Kozlikova B, Gora A, Sustr V, Klvana M, Medek P, Biedermannova L, Sochor J, & Damborsky J (2012) CAVER 3.0: A Tool for the Analysis of Transport Pathways in Dynamic Protein Structures. *PLoS Comput Biol* 8:e1002708.

2. Winter MB, Herzik MA Jr, Kuriyan J, & Marletta MA (2011) Tunnels modulate ligand flux in a heme nitric oxide/oxygen binding (H-NOX) domain. *Proc Natl Acad Sci USA* 108:E881–E889.

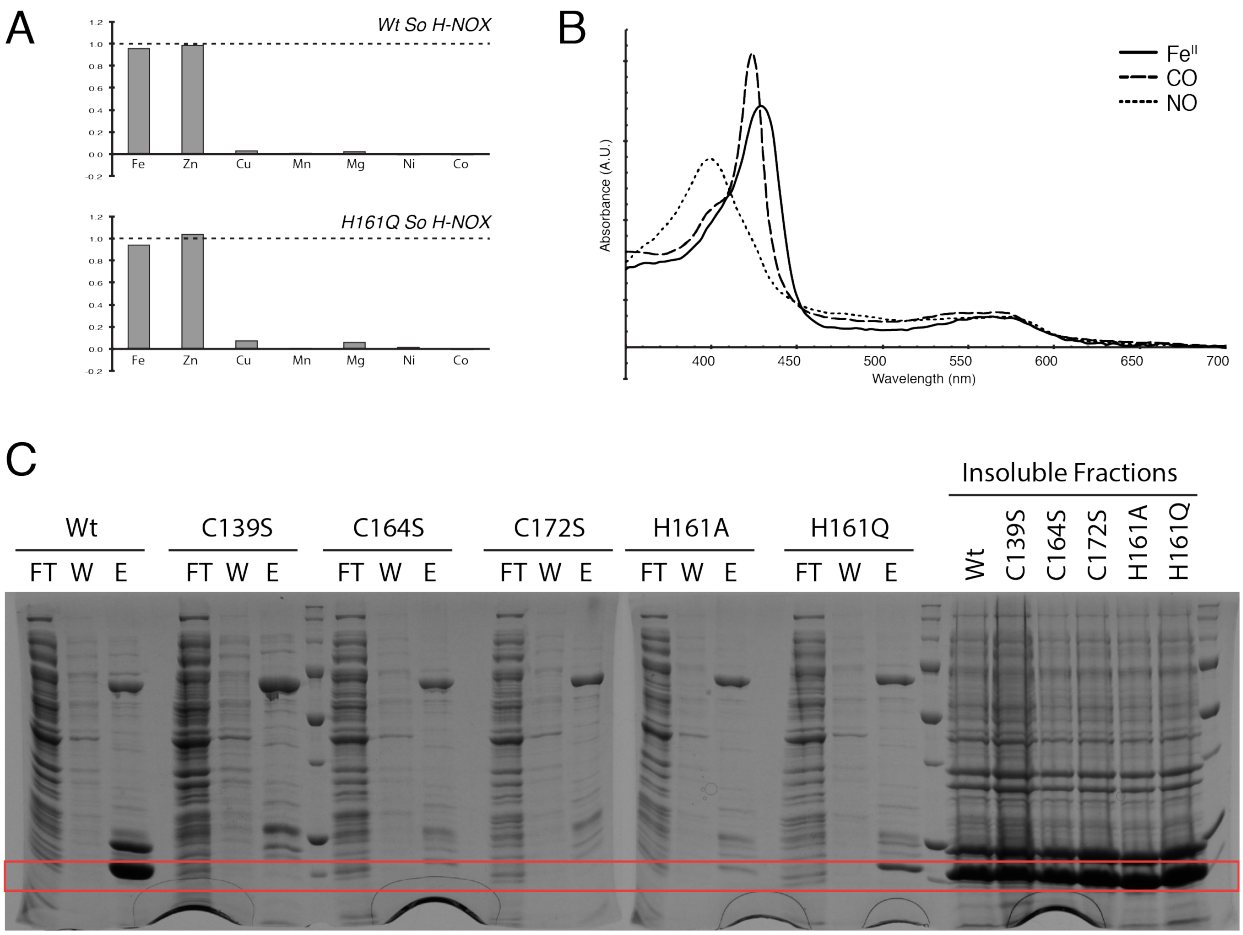

Figure B.2. Mutational analysis of the zinc-coordination site in *So* H-NOX. (**A**) ICP-AES analysis of Wt and H161Q *So* H-NOX. Metal content was normalized to protein concentration and values are averaged between ≥3 measurements. (**B**) UV-VIS absorption spectra for various ligand complexes of H161Q *So* H-NOX. (**C**) SDS-PAGE analysis of zinc-coordination mutants in *So* H-NOX following Ni^{2+} affinity purification. For each mutant, samples of the flow-thru (FT), wash (W), elution (E) and the insoluble fractions were analyzed.

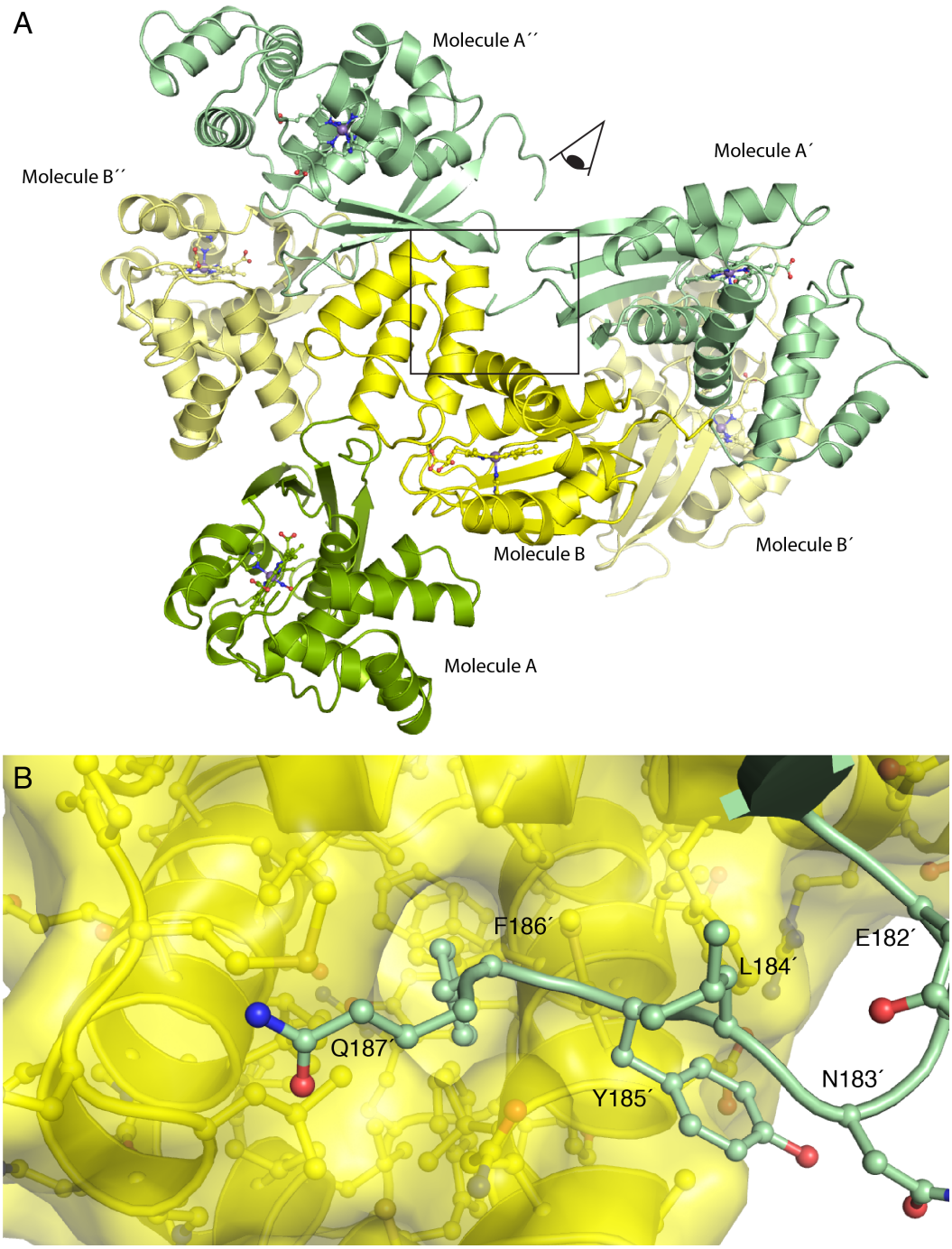

Figure B.3 The C-terminus of molecule A´ prevents ligand binding to molecule B. (**A**) Molecules A (green) and B (yellow) of MnPPIX-NO *So* H-NOX with crystallographic symmetry mates A´ and A´´ (colored palegreen) and B´ and B´´ (colored paleyellow) shown in cartoon representation. (**B**) Zoomed-in view of the interaction between molecule A´ (C-terminal residues are shown as sticks) and molecule B (shown in semi-transparent surface) demonstrating that residue F186 from the C-terminus of molecule A´ blocks tunnel 1 of molecule B. It is hypothesized that this interaction prevents binding of NO and CO ligands to molecule B *in crystallo* during the soaking experiments.

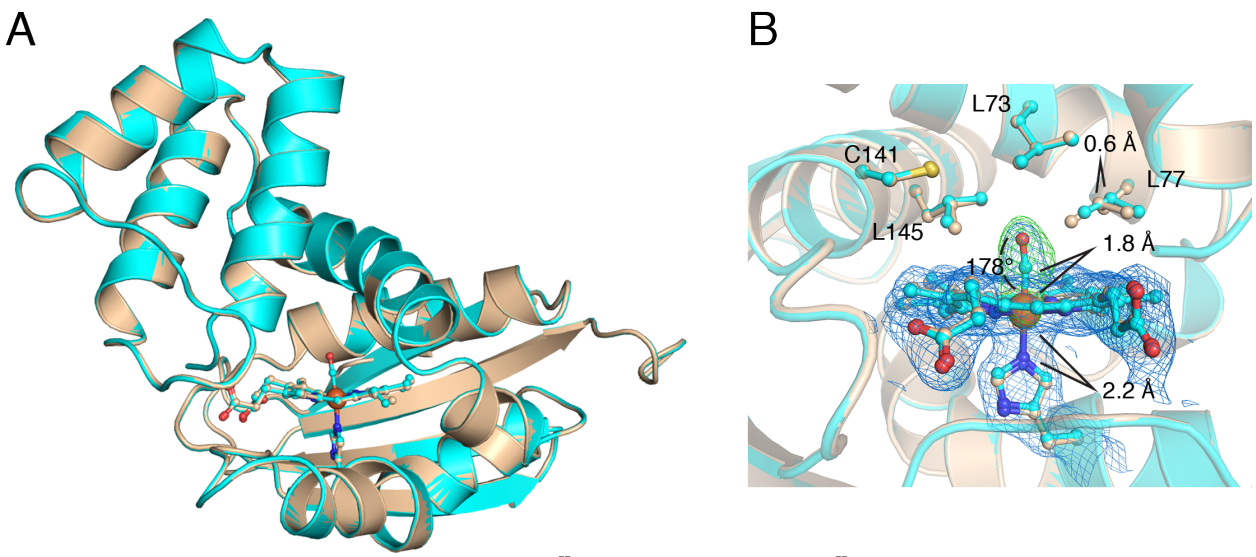

Figure B.4 Structural comparison of Fe^{II}-unliganded and Fe^{II}-CO *So* H-NOX. (**A**) Overall structural alignment of Fe^{II} (wheat) and Fe^{II}-CO (blue) *So* H-NOX crystal structures (molecules A). (**B**) Detailed view of the Fe^{II}-CO H-NOX heme pocket. $2mF_o$-DF_c electron density (blue mesh, 1σ) and isomorphous F_o-F_o (CO - native) difference density (positive, green mesh; negative, red mesh, 5σ) are displayed.

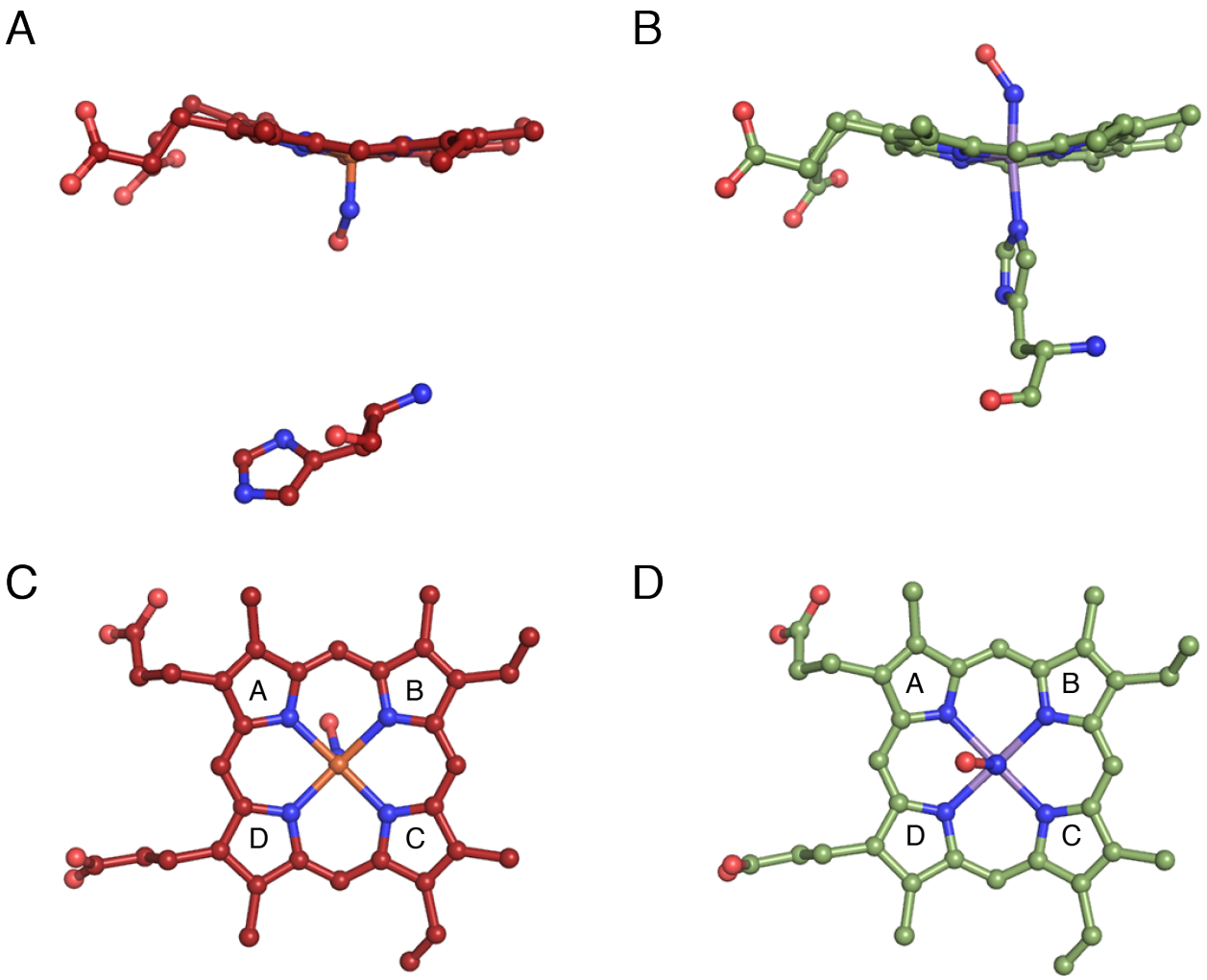

Figure B.5 Distal and proximal-bound NO exhibit different orientations in *So* H-NOX. Panels **A** and **C** correspond to the proximal-bound, five-coordinate NO complex and panels **B** and **D** correspond to the distal-bound, six-coordinate NO complex. Panels **C** and **D** are 90° rotations of panels **A** and **B**, respectively.

Appendix C

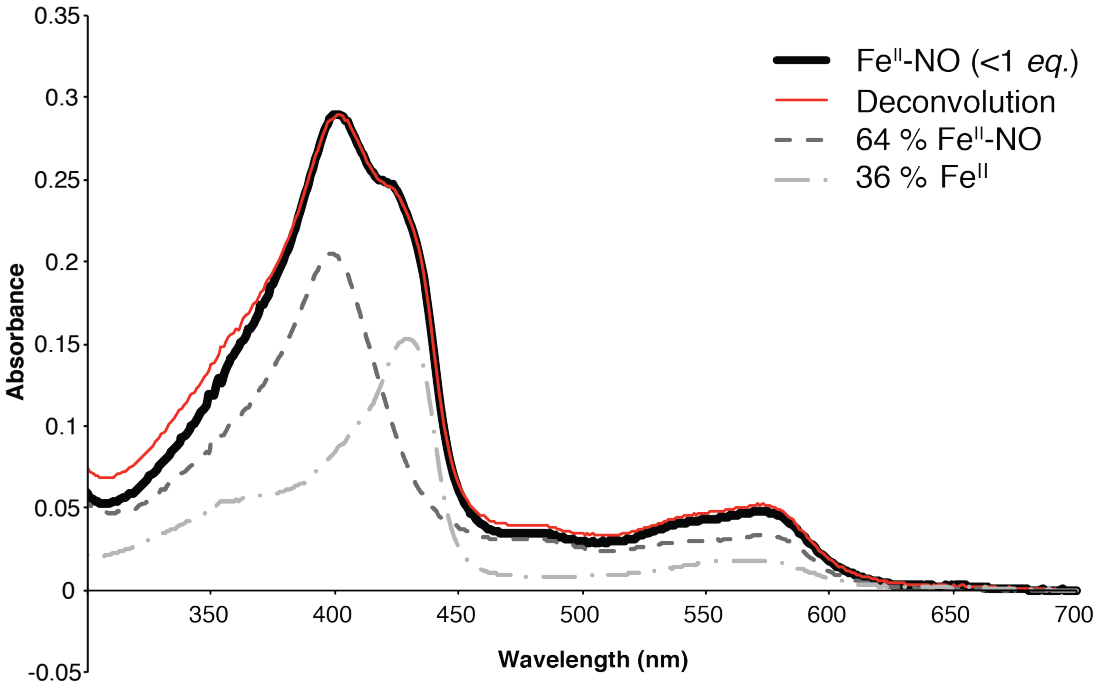

Figure C.1 Electronic absorption spectrum of *So* H-NOX (~5 uM heme concentration) following treatment with a substoichiometric amount of NO (0.6-0.8 *eq*.) (black). The reconstructed spectrum as calculated from single value decomposition (red) is shown as well as the corresponding contributions of ferrous-nitrosyl (dashed) and ferrous-unliganded (dashed-dot) spectra.

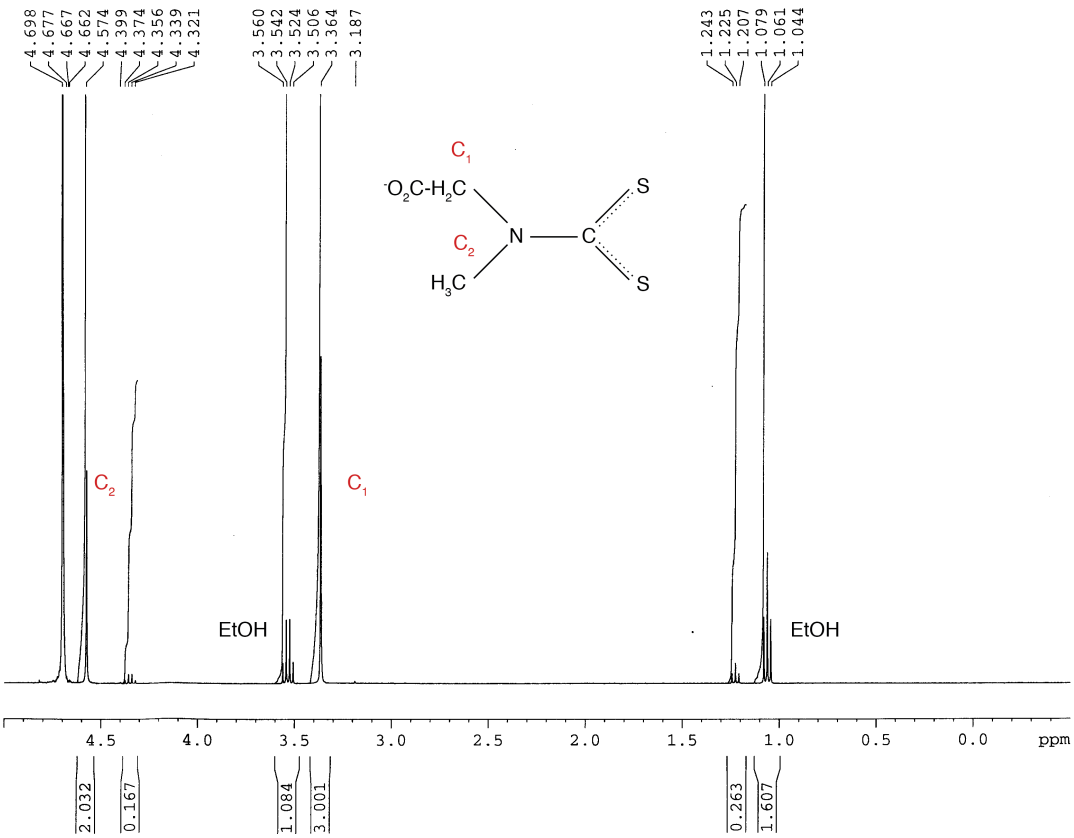

Figure C.2 ^{1}H-NMR spectra of *N*-(dithiocarboxy)-sarcosine in D_2O. Spectra were acquired on a Bruker AVB-400 (400 MHz) spectrometer at 294 K.

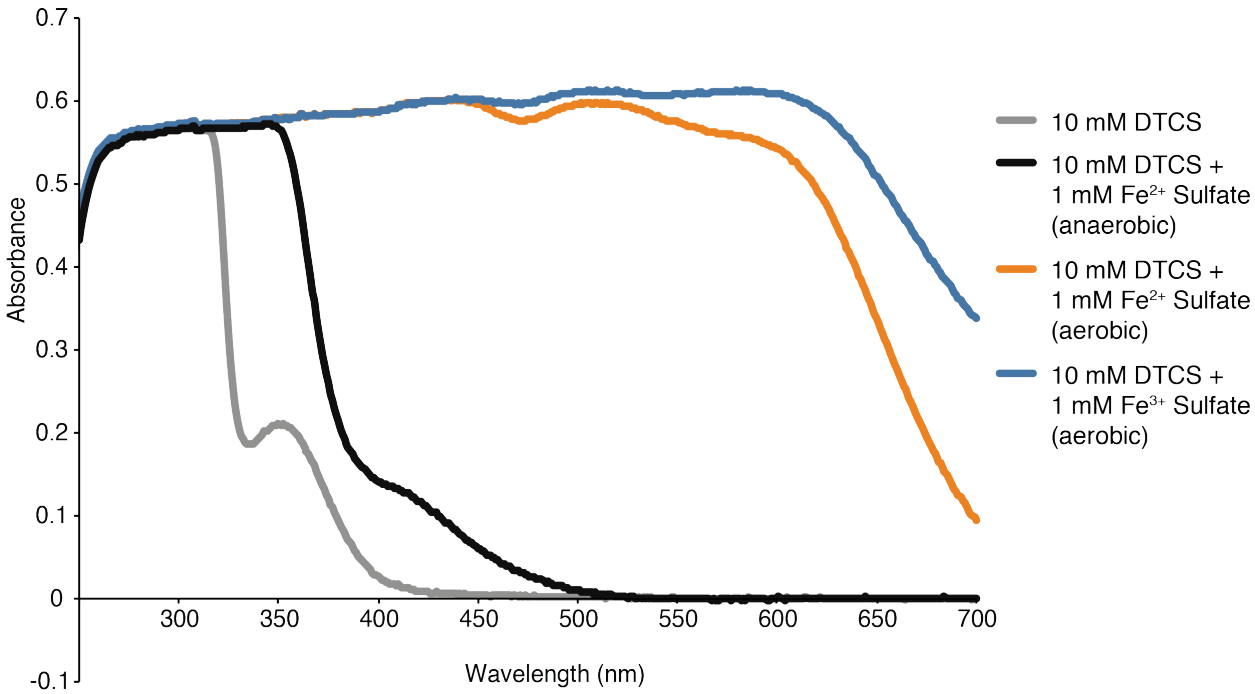

Figure C.3 Electronic absorption spectra of *N*-(dithiocarboxy)sarcosine (DTCS) and iron-chelates. Oxidation of the chelated iron in ferro-di(*N*-(dithiocarboxy)sarcosine results in increased absorbance across the 400-700 nm wavelength range due to decreased solubility of the ferri-di(*N*-(dithiocarboxy)sarcosine complex as compared to the ferrous complex.

Appendix D

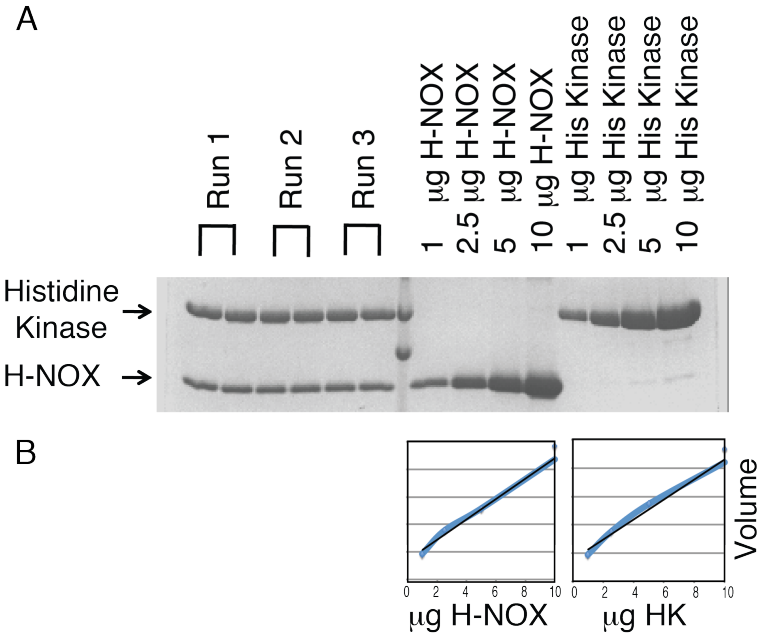

C

	Calculated Amount (μg)	Calculated Amount (μmol)	H-NOX:HK
H-NOX	1.25 (± .1)	57.5	0.8
Histidine Kinase	2.52 (± .3)	71.6	

Figure D.1 Determination of the H-NOX: histidine kinase complex stoichiometry using SDS-PAGE and densitometry. (**A**) Complexes of H-NOX: histidine kinase were purified by gel filtration and the peak fractions corresponding to the complex from each of three runs were analyzed by SDS-PAGE. The integrated volume of each protein band was quantified by densitometry using ImageJ and the total amount of protein was determined via fitting to standard curves of known quantities of H-NOX and histidine kinase (shown in (**B**)) (1). (**C**) Average amounts of each protein component calculated using densitometry and the final calculated stoichiometry.

References

1. Schneider CA, Rasband WS, & Eliceiri KW (2012) NIH Image to ImageJ: 25 years of image analysis. *Nat Methods* 9(**7**) 671-675.

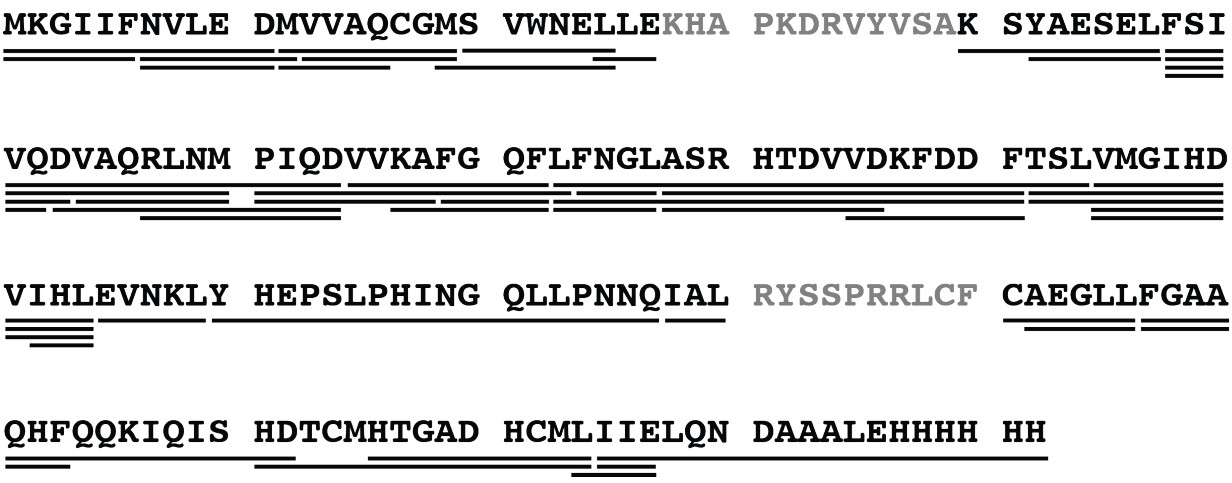

Figure D.2 Pepsin-generated peptides of *So* H-NOX mapped to the amino acid sequence. The length of each line dictates the boundaries of the corresponding peptide. Amino acids colored gray were not observed by mass spectrometry. Total sequence coverage was 89%.

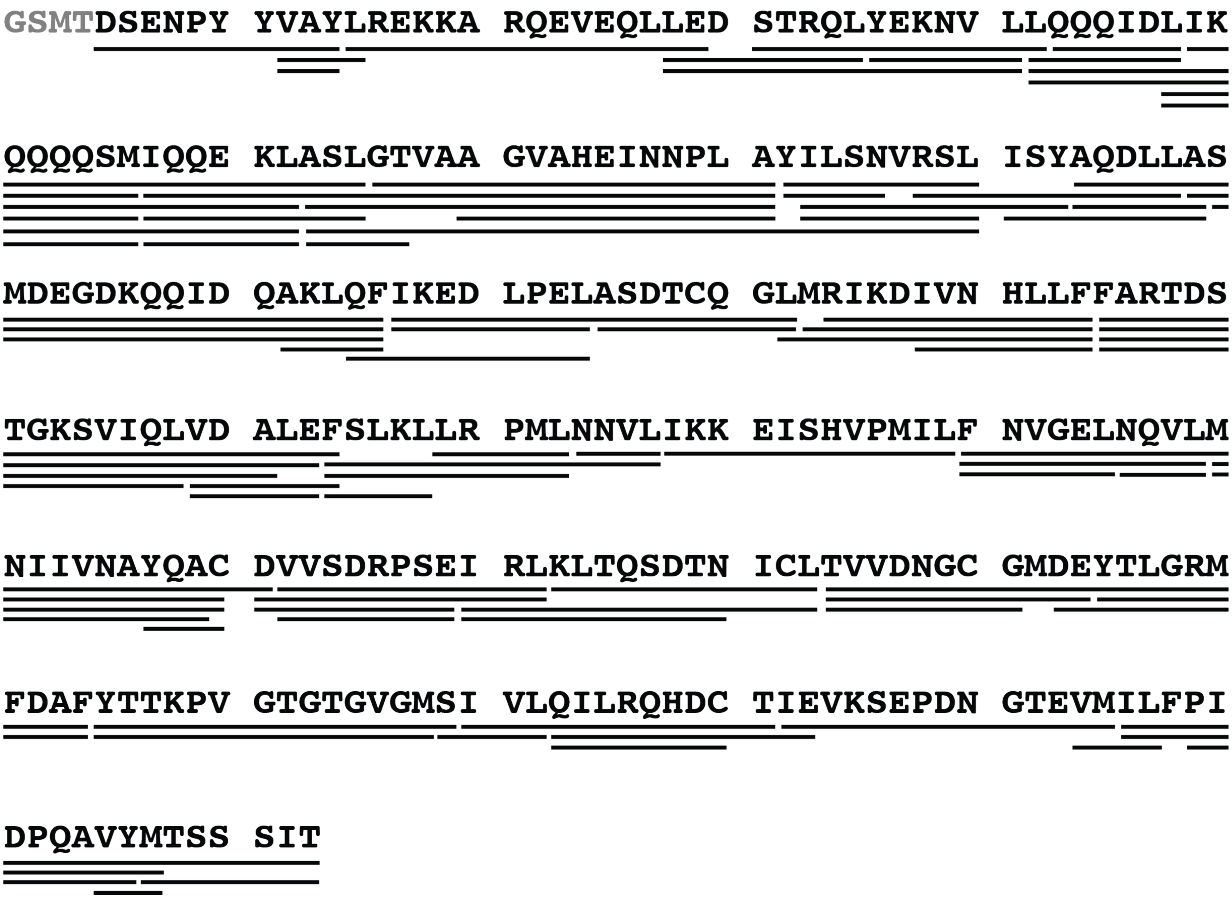

Figure D.3 Pepsin-generated peptides of histidine kinase SO2145 mapped to the amino acid sequence. The length of each line dictates the boundaries of the corresponding peptide. Amino acids colored gray were not observed by mass spectrometry. Total sequence coverage was 99%.